Cu ELECTRODEPOSITION ON Ru-Ta AND CORROSION OF PLASMA TREATED Cu

IN POST ETCH CLEANING SOLUTION

Karthikeyan Sundararaju Meenakshiah Pillai, B.Tech, M.S.

Dissertation Prepared for the Degree of

DOCTOR OF PHILOSOPHY

UNIVERSITY OF NORTH TEXAS

August 2011

APPROVED:

Oliver M.R. Chyan, Major Professor
Michael G. Richmond, Committee Member
Guido Verbeck, Committee Member
Justin Youngblood, Committee Member
William Acree, Chair of the Department of
    Chemistry
James D. Meernik, Acting Dean of the
    Toulouse Graduate School

Sundararaju Meenakshiah Pillai, Karthikeyan. <u>Cu Electrodeposition on Ru-Ta and Corrosion of Plasma Treated Cu in Post Etch Cleaning Solution</u>. Doctor of Philosophy (Chemistry-Analytical Chemistry), August 2011, 109 pages, 4 tables, 68 figures, chapter references.

In this work, the possibility of Cu electrodeposition on Ru-Ta alloy thin films is explored. Ru and Ta were sputter deposited on Si substrate with different composition verified by RBS. Four point probe, XRD, TEM and AFM were used to study the properties of Ru-Ta thin films such as sheet resistance, crystallinity, grain size, etc. Cyclic voltammetry is used to study the Cu electrodeposition characteristics on Ru-Ta after various surface pretreatments. The results provide insights on the removal of Ta oxide such that it enables better Cu nucleation and adhesion. Bimetallic corrosion of Cu on modified Ru-Ta surface was studied in CMP related chemicals.

In Cu interconnect fabrication process, the making of trenches and vias on low-k dielectric films involves the application of fluorocarbon plasma etch gases. Cu microdots deposited on Ru and Ta substrate were treated by fluorocarbon plasma etch gases such as CF_4, CF_4+O_2, CH_2F_2, C_4F_8 and SF_6 and investigated by using x-ray photoelectron spectroscopy, contact angle measurement and electrochemical techniques. Micropattern corrosion screening technique was used to measure the corrosion rate of plasma treated Cu. XPS results revealed different surface chemistry on Cu after treating with plasma etching. The fluorine/carbon ratio of the etching gases results in different extent of fluorocarbon polymer residues and affects the cleaning efficiency and Cu corrosion trends.

ACKNOWLEDGEMENTS

TABLE OF CONTENTS

LIST OF TABLES

LIST OF ILLUSTRATIONS

CHAPTER 1

INTRODUCTION

1.1 Introduction to Integrated Circuits (IC)

This introductory chapter is written with an objective of explaining the purposes, analytical techniques, and methods etc. in order to provide a brief outline of the thesis for the reader. Semiconductors are materials that are highly useful and important because of their conducting nature which lies in between metals and insulator. The most commonly used semiconductor materials are silicon (Si) and germanium (Ge). Some others such as silicon carbide (SiC), gallium arsenate (GaAs) and silicon germanium (SiGe) are also used as semiconductor materials. The conductivity of a semiconductor can be controlled by adding certain impurities to that, a process called "doping" and by applying an electric field.

An integrated circuit (IC) is essentially a combination of diodes, resistors and transistors with which more than 90% of electronic devices are fabricated. Germanium, the semiconductor material used by Bardeen and Brattain to develop the first point-contact transistor [1] in 1947, was the material of choice for many years due to its best crystalline quality achievable at that time. For more than a decade, till the late 1950s – early 1960s, Ge had been the workhorse for the development of bipolar transistors. To provide a historical perspective, Figure 1.1 shows the image of the first transistor invented at Bell laboratories. The two point contacts at the bottom of the triangular quartz crystal were made from two strips of gold foil separated by about 50 μm and pressed onto the Ge surface. With one gold contact forward biased and the other reverse biased, the transistor action was observed and this was the beginning of what is known as the electronic age.

With the development of field effect transistors in late 1960s, Ge was considered secondary to silicon and was largely abandoned by the semiconductor industry, mainly due to its unfavorable surface properties and to the fact that, in contrast with Si, it has no stable natural oxide required for metal oxide semiconductor (MOS) operation. The first integrated circuit was made by Jack Kilby using single-crystal germanium substrate, Figure 1.2. However, germanium was replaced by silicon quickly and the IC industry was entirely dominated by silicon since the 1960s. Since then, the IC industry has developed exponentially and the exponential progress of metal oxide semiconductor technology is best illustrated by the evolution of the number of MOS transistors integrated in a single memory chip or single microprocessor, as a function of a calendar year. Figure 1.3 shows that the number of transistors doubles every 2 years. This exponential growth of integration density with time is known as Moore's law [2].
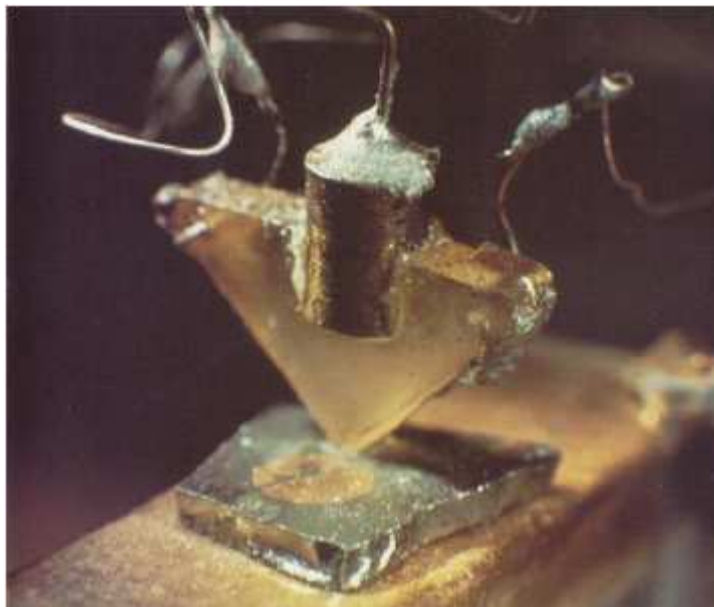
Figure 1.1 First point contact transistor invented in 1947 at Bell laboratories [3]
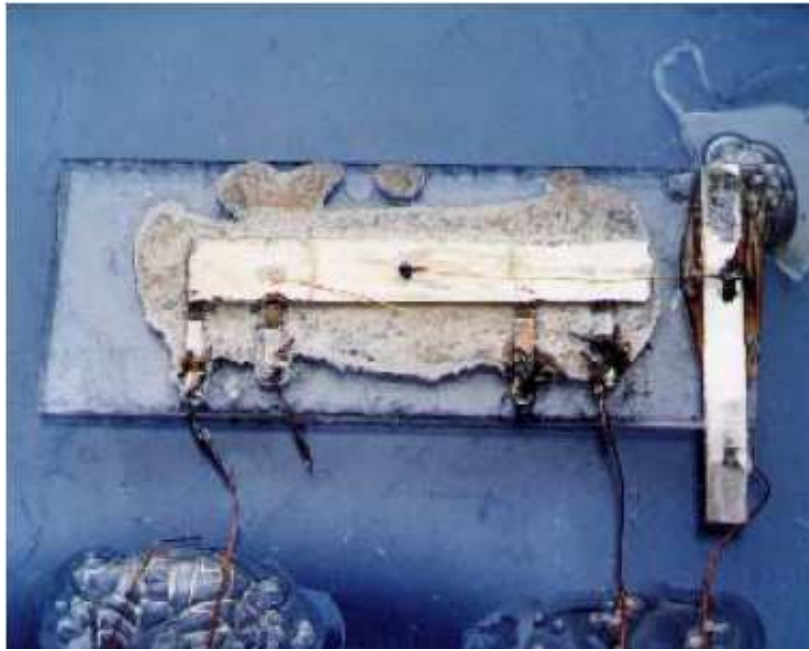
Figure 1.2 First integrated circuit invented in late 1950s [4]
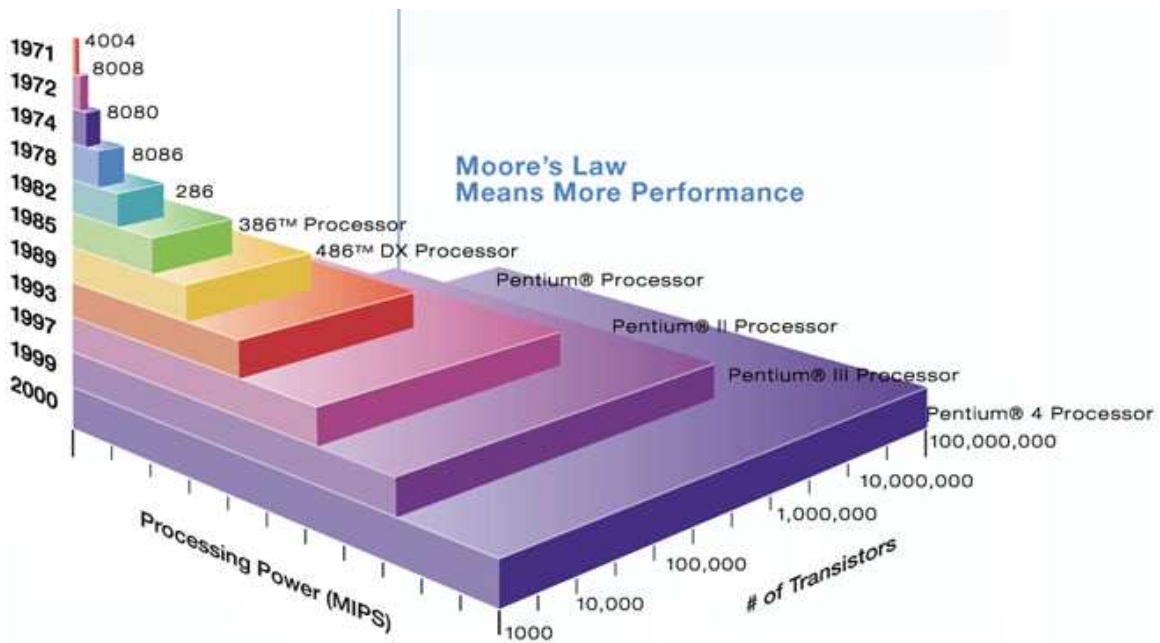
Figure 1.3 Graph of no. of transistors vs. year demonstrating Moore's law [5]

In memory circuits, the integration density is about 5 to 10 times higher than that in logic circuits because of the repeated layout of arrays in memory chips. The reason behind the increase in integration density is the decrease in transistor size [6]. The decrease in the feature size from a few microns in the 1970s to 65 nm in 2007 has been shown in Figure 1.4. As a result of continuous decrease in feature size, the complexity in fabrication technologies has been increased and requires discovery of new materials. To represent the level of complexities, a term called ultra large scale integration (ULSI) was introduced for chips of more than 1 billion transistors.
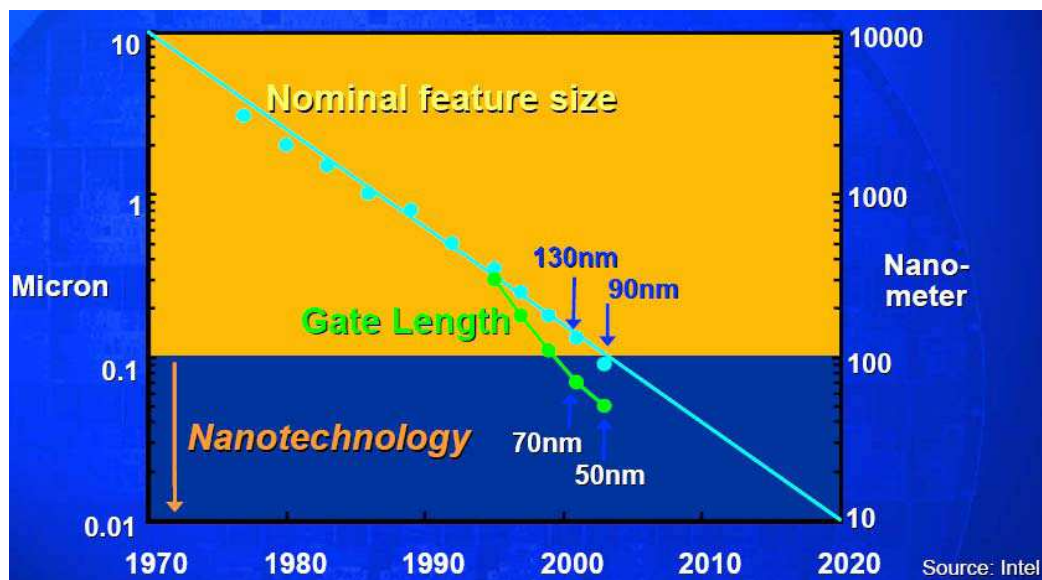
Figure 1.4 Graph showing the decrease in feature size from the year 1970 to 2020 [7]

Multilevel metallization has become the key process in fabricating ULSI devices [8]. Interconnects serve as local and global wiring, which connect circuit elements and distribute power. Earlier, aluminum (resistivity ~ 2.5 $\mu\Omega$.cm) was used as the interconnect metal in devices with large feature size. Due to the need for faster devices, metals with lower resistance than aluminum are required to reduce the interconnect time delay. Copper (resistivity ~ 1.67

4

μΩcm) has become the metal of choice for fabricating submicron devices. Not only has copper the ability to reduce the resistance-capacitance product (RC) delay due to its lower resistivity, but also increase the circuit reliability because of its higher electromigration resistance [9].

Cu interconnects are fabricated by dual damascene process as opposed to plasma etching and plasma masking through which Al was fabricated. Figure 1.5 shows the scheme of fabricating Cu interconnects – dual damascene process.
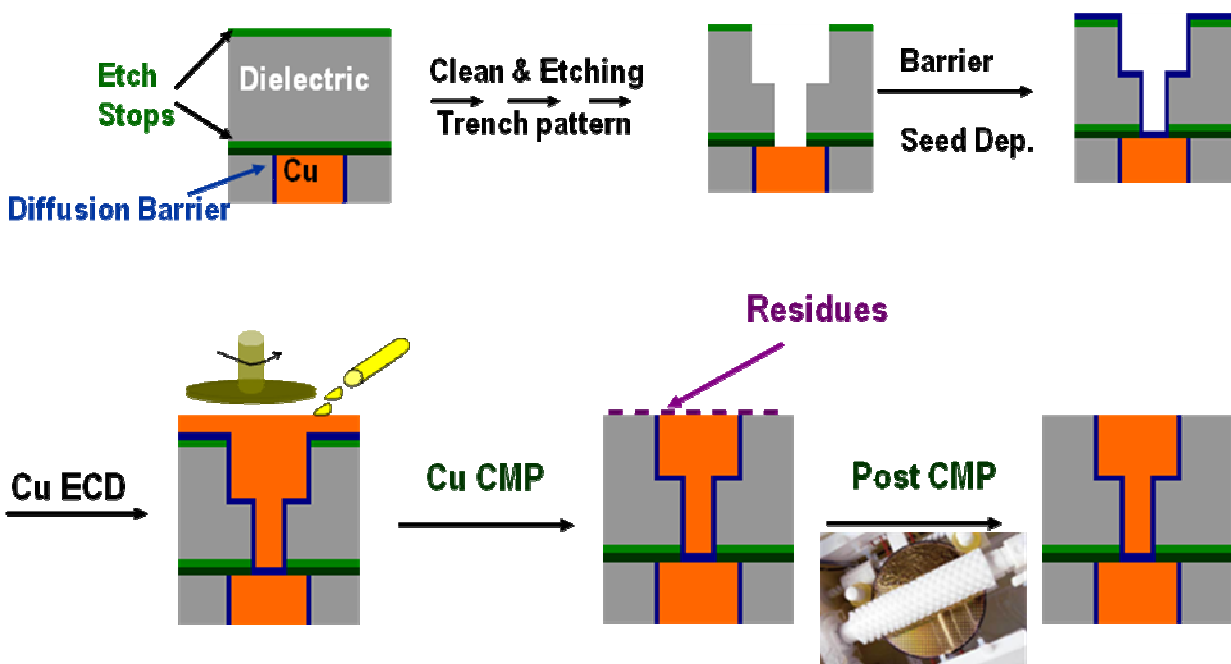
Figure 1.5 Schematic of Cu interconnects dual damascene process

The damascene process involves etching a trench through pattern into a dielectric, the blanket deposition of a diffusion barrier followed by Cu electroplating, and finally removal of Cu overburden by chemical–mechanical planarization (CMP).

The current diffusion barrier material used in the industry is TaN/Ta and when the device dimensions decrease resulting in thinning of the layers, the resistance increases dramatically causing problems during Cu electroplating. Recent results from different research groups have

shown that Pt group metals like ruthenium (Ru), osmium (Os), and iridium (Ir) can act as better copper diffusion barrier [10-16].   On 2003, Chyan et al. [10] and Moffat et al. [11] proposed Ru as the novel copper diffusion barrier with the importance of Ru forming a conductive platform for Cu electrodeposition.   More recently Arunagiri et al. have shown that 5 nm of Ru can even stop Cu diffusion into Si till 450° C [17]. Ru being highly noble metal causes enhanced galvanic corrosion of Cu during CMP process. Therefore, an ideal diffusion barrier layer is desired to have the following characteristics:

1. Good adhesion between interlayer dielectrics and Cu layer

2. Ability to prevent Cu diffusion at elevated temperatures

3. Allow bottom up Cu super-fill with direct electroplating of Cu

4. Conformal deposition

Recently, an alloy of Ru & Ta has attracted much interest in performing as a good diffusion barrier for Cu. Literature support that 15 nm of Ru-Ta alloy can prevent Cu diffusion until after annealing at 700 C and therefore acting as an effective liner material [18]. So far in the literature, only sputtering of Cu has been done to study the barrier properties of Ru-Ta alloys. In this work, direct electroplating of Cu on Ru-Ta is explored.

Chapter 2 deals with preparation of Ru-Ta thin films with various compositions by sputtering technique. The characterizations were done using Rutherford backscattering spectroscopy (RBS) for composition analysis, four point probe for sheet resistance values, atomic force microscopy to study the surface morphology, x-ray diffraction (XRD) for thin film crystalline studies and transmission electron microscope (TEM) for imaging the surface.

Chapter 3 deals with studies of Cu electroplating on Ru-Ta using electrochemical techniques such as cyclic voltammetry (CV), chronoamperometry, open circuit potential (OCP),

bulk electrolysis etc. Also the studies including various surface treatments done on Ru-Ta and the effect of those treatments on improving the Cu plateability of Ru-Ta.

During the plasma etching of dielectrics to create trench / via patterns, the plasma radicals and ions from fluorocarbon gases not only etch away the dielectrics but also interact with Cu surface changing Cu surface chemistry. The corrosion behavior of this plasma treated Cu in post etch cleaning environments is not documented in literature. Chapter 4 includes this study of Cu corrosion behavior treated by etch gas plasma. The obtained micropattern corrosion data reveals the corrosion rate of Cu treated by different fluorocarbon etch gas plasma, interfacial characterization was carried out by x-ray photoelectron spectroscopy (XPS), direct current measurements and water contact angle measurements. The rest of this chapter will discuss about various instrumentation that have been used throughout my research to produce this dissertation.

1.2 Instrumentation

Several surface characterization tools and electrochemical techniques were utilized in this work. The working principles of the following instruments/techniques will be discussed - X-ray photoelectron spectroscopy, x-ray diffraction spectrometry, atomic force microscopy, direct current measurements, electrochemical techniques, etc.

1.2.1 X-ray Photoelectron Spectroscopy

X-ray photoelectron spectroscopy (XPS), also known as electron spectroscopy for chemical analysis (ESCA), is a highly sensitive technique for measuring surface atomic composition [19]. In the microelectronics area, it has been extensively used to evaluate cleaning and surface preparation, as well as composition and bonding structures of barrier and dielectric films. It has also been used to study the fluorocarbon residues that are generated during plasma etching of dielectrics.

XPS is based on measuring the binding energy of photoelectrons emitted from core shells when a monochromatic x-ray beam hits the sample and the schematic of photoelectric effect is shown in Figure 1.6. Binding energy is a measure of the attractive force between the electron and the nucleus. The magnitude of this force depends on the charge of the nucleus – hence, every atom has a characteristic binding energy and XPS uses this principle to identify atoms. During this process, photoelectrons are also emitted from outer shells of the atom – however, the electrons emitted from a core shell without inelastic energy losses are the ones that are used to calculate the composition. The concentration of the atom giving rise to the photoelectron is estimated by taking into account the geometry of the system, atomic mass, photoemission cross-section, electron attenuation length, and spectrometer transmission and detection efficiency. In order to minimize loss of kinetic energy of the photoelectrons, the analysis is done under ultra-low vacuum ($<5\times10^{-9}$ torr) to avoid collisions with other electrons or residual gas molecules. Ultra-low vacuum also prevents spectral interference from adsorbed gas molecules that may occur at higher pressures. An electron energy analyzer collects the photoelectrons and measures their kinetic energy while an electron detector counts the number of photoelectrons emitted. The binding energy of the electrons is related to the kinetic energy by the expression:

K.E. = hυ – B.E. –φ$_{sp}$ --------------- (1)

where, K.E is the kinetic energy of the photoelectron (measured by the detector), hυ is the

energy of the x-ray beam, B.E. is the binding energy of the photoelectron, and φ $_{sp}$ is the work

function (which is a constant for a given spectrometer). Because of the low kinetic energy of the

photoelectrons, the electron attenuation lengths are very small (order of 3 nm) and therefore this

technique is highly surface sensitive. Only electrons emitted within 3-5 times the attenuation

lengths reach the detector and hence only the top1-10 nm of the surface is probed. The

sensitivity of this technique is 0.01-1 atomic%.
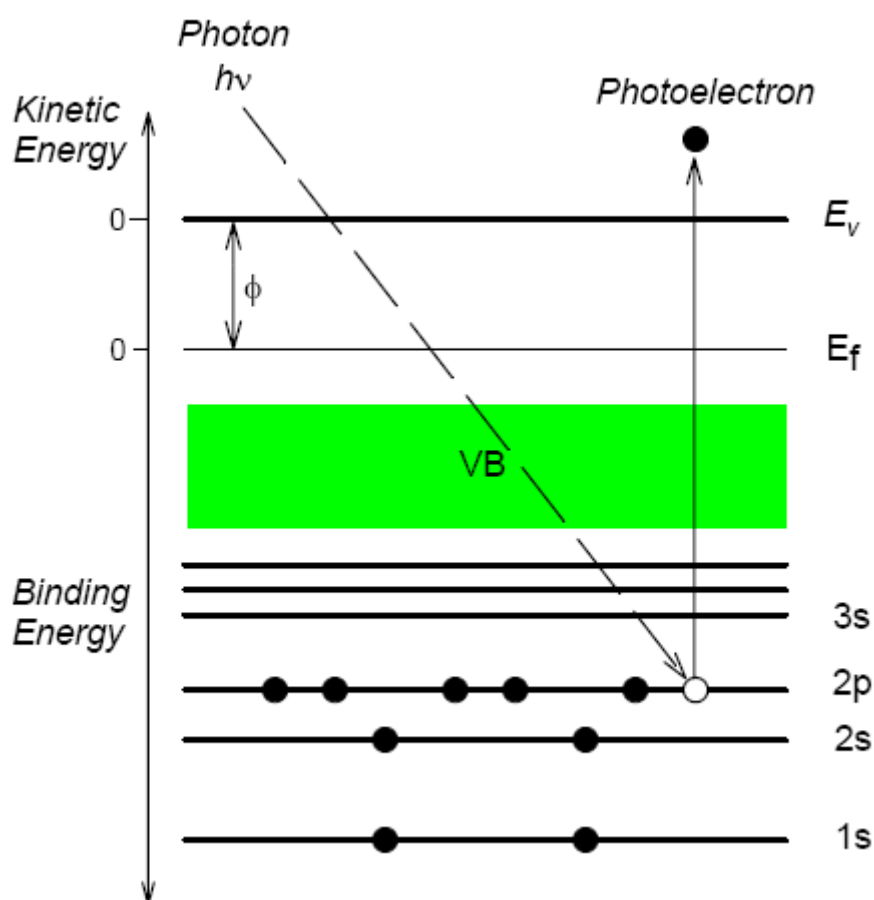
Figure 1.6 Schematic of photoelectric effect which is the basis of XPS

Besides atomic composition, XPS also provides information on the bonding structure and composition variation with depth into a film or surface. When an atom is bonded to a more electronegative atom, the outer shell electrons are pulled towards the electronegative atom leading to a slight positive charge on the nucleus. This leads to the inner core electrons being held more strongly by the nucleus. Hence, the binding energy of the core electrons shifts to higher energies. This shift in binding energy can provide information on the bonding structure of the material being analyzed. If it is bonded to more than one fluorine atom, the shift is even higher (around 290 eV for $-CF_2-$ and 293 eV for $-CF_3$). By fitting Gaussian- Lorentzian shapes to carbon peaks, one can estimate the percentage of atoms with various bonding configurations (from the area under the XPS peaks). The intensity of photoelectrons also depends on the geometry of the XPS system – the angle between the sample surface and total intensity is an integral over the photoelectrons emitted at various depths. The detector can be changed to probe deeper or shallower into the film. All XPS measurements in this dissertation are made on a PHI 1600 model XPS system. It is equipped with a monochromatic Al K α source (1486.7 eV) generated using a water cooled anode operating at a power of 350 W.

Data collection is performed using PHI Explorer software (Physical Electronics, v3.4) and is analyzed using Multipak software (Physical Electronics, v5.0A). The photoelectrons emitted are collected and analyzed in an 180° hemispherical analyzer and multichannel detector. The C1s peak (284.8 eV) is used as a reference to maximize the photoelectron count by adjusting the position of the sample relative to the source and the detector. Survey (low resolution) scans are collected first (0.5 eV, 50 ms/step) to identify all the chemical elements on the surface. Then, high resolution spectra are collected with a different set of conditions (0.05 eV and 200 ms/step) for each of the elements detected. Unless specified, these spectra are collected at 45°

and pass energy of 23.5 eV. XPS was used extensively to collect the fluorocarbon deposits on

Cu surface after treating with plasma, in chapter 4.

1.2.2 Contact Angle

The contact angle is defined as the angle between the tangent to the droplet of a liquid

placed on a flat, homogenous surface, and the surface. The contact angle of a small, sessile (free

standing) drop, is a function of the surface free energy, and is defined by the Young-Dupré

equation [20]

$$\gamma_{LV} \cos\theta = \gamma_{SV} - \gamma_{SL} \qquad \text{------------ (2)}$$

where θ is the contact angle, γ is the interfacial free energy per unit area, and LV, SV, and SL

refer to liquid-vapor, solid-vapor, and solid-liquid interfaces, respectively.
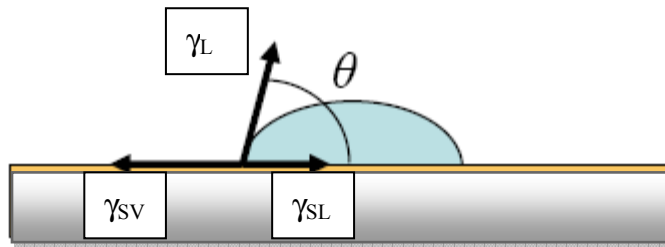
Figure 1.7 A sessile drop on a solid surface in equilibrium with the vapor phase

Figure 1.7 presents an illustration of the parameters used in the Young-Dupré equation.

The angle of a drop on a solid surface is the result of the balance between the cohesive forces in

the liquid and the adhesive forces between the solid and the liquid. If there is no interaction

between the solid and the liquid, the contact angle will be 180º. As the interaction between the

solid and the liquid increases, the liquid spreads until $\theta = 0$ º and equation 1 becomes:

$$\gamma_{LV} = \gamma_{SV} - \gamma_{SL} \qquad \text{------------ (3)}$$

When water is used to measure the contact angle, one determines the hydrophilic or hydrophobic character of the surface. A smooth solid surface exposing closely packed methyl groups ($-CH_3$) has been found to exhibit highly hydrophobic properties. Water contact angles for such a surface range from 105°-110° [21-22]. On the other hand, a solid surface exposing closely packed ethylene groups ($-CH_2-$), as on a smooth polyethylene surface, gives a water contact angle of 100°-103°. The contact angle will mostly be affected by the terminal group of the molecule under investigation. In the case of $-NO_2$ or $-OH$ terminal groups, when the tail group of the molecule is polar, the wetting properties should be more hydrophilic, resulting in smaller contact angles than for methyl group-terminated monolayers. Contact angle measurements, while simple, can provide significant information. Whitesides and co-workers [23] used contact angle measurements to show the effect of burying the polar group in the monolayer by changing the length of the R group in a $HS-(CH_2)_{16}-OR$ monolayer. They concluded that a group buried under more than two methylene groups does not influence the wettability of the monolayer. Studies on mixed monolayers with hydrophilic and hydrophobic terminal groups were conducted by Ulman [24,25]. In this dissertation, contact angle measurements were done on plasma treated Cu surface and are described in chapter 4.

1.2.3 Plasma Treatment

Plasma is a partially-ionized gas consisting of equal numbers of positive and negative charges and a different number of unionized neutral molecules. When a gas is subjected to a direct current (DC) or radio frequency (RF) potential at reduced pressure this is usually accompanied by glow, which is known as glow discharge. The words glow discharge and plasma tend to be used synonymously, although glow discharges are not perfect plasmas. The characteristic glow of these plasmas is due to electronically excited species producing optical

emission in the ultraviolet or visible regions of the spectrum and is characteristic of the composition of the glow discharge gas. For example, argon gives a bright blue color and air or nitrogen gives a pink color that is due to excited nitrogen molecules. Various excitation processes can be initiated by plasma.

Ionization

In the context of plasma-enhanced chemistry reactors, the plasma is created in a vacuum chamber, which contains a constant flow of a gas at reduced pressure - typically in the order of 1mbar. This gas is exposed to a RF potential, which results in the partial ionization of the gas. In the ionization process, a bound electron in an atom is ejected from that atom. For example, the ionization of an argon atom is expressed as follows:

$$e^- - Ar \longrightarrow Ar^+ + e$$
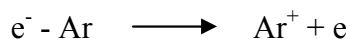
Excitation

A less dramatic transfer of energy allows the electron to jump to a higher energy level within the atom. This process is known as excitation. The excited state of an atom is conventionally shown by an asterisk:

$$e + Ar \longrightarrow Ar* + e$$
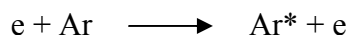
Dissociation

A further process that can occur is the dissociation of a molecule. If oxygen, for example, is the gas subjected to the RF potential, the oxygen molecule can be dissociated into two oxygen atoms, $e + O_2 \longrightarrow e + O + O$ whereas a monatomic gas such as argon cannot be dissociated at all.

Part of the process in creating plasma is radical formation. Oxygen and other reactive gases will also form radicals to certain extent. Ground state oxygen, O_2 is a triplet diradical.

Diradicals are species with a pair of degenerate (equal energy) molecular orbitals and two electrons. There are three possible diradical arrangements: the singlet state, the triplet state and an unstable intermediate state. The following scheme shows the electron arrangement in orbitals for these three diradical species:

Singlet Diradical	Unstable	Triplet Diradical
Two electrons with one in one orbital with other empty Spin Paired	One electron in each of two orbitals Spin Paired	One electron in each of two orbitals Spin Unpaired
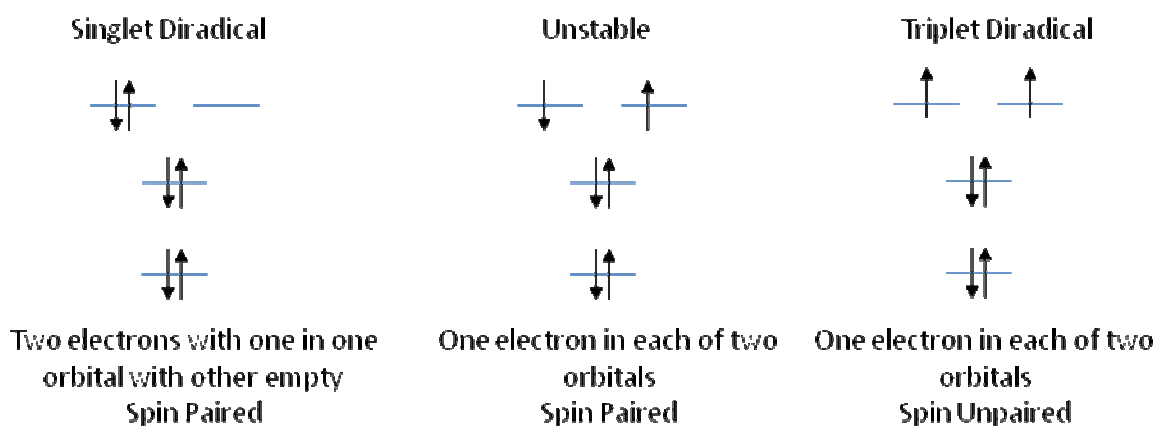
A normal result of dissociation is an enhancement of chemical reactivity, since the products are usually more reactive than the parent molecule. Dissociation may or may not be accompanied by ionization, for example:

$$e + CF_4 \longrightarrow e + CF_3 + F \text{ (Dissociation) or}$$

$$e + CF_4 \longrightarrow 2e + CF_3^+ + F \text{ (Ionization)}$$
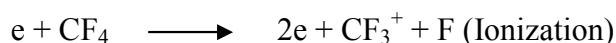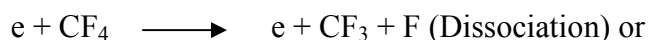
In summary, exposing a gas to the RF potential at reduced pressure creates a plasma which contains active species - for example, in the case of oxygen, atomic oxygen. Oxygen atoms will oxidize organic molecules more readily than oxygen molecules. So typically a cellulose material can be converted to carbon dioxide, carbon monoxide and water at room temperature, rather than at elevated temperatures (e.g. burning) and furthermore the oxidation under plasma treatment is more controllable.

1.2.4 Atomic Force Microscopy (AFM)

Atomic force microscopy is one of the scanning probe microscopes (SPM), developed by Binnig, Quate and Gerber in 1986. It is basically used for imaging, measuring and manipulating matters at the surface of a sample at nanoscale. AFM can be used for imaging both conducting and non-conducting sample to record the contours of repulsion force developed by the overlapping of the electron cloud at the AFM probe tip with those surface atoms [26-29]. Piezoelectric elements that facilitate tiny but accurate and precise movements on (electronic) command enable the very precise scanning.

The AFM consists of a cantilever in micron size with a sharp needle-like tip at its end that is used to scan the sample surface. The cantilever is typically made of silicon or silicon nitride with a tip radius of curvature on the order of nanometers. It works like a spring to keep the tip against the surface when moving back and forth. When the tip is moved closer to the sample surface, forces between the tip and the sample result in deflection of the cantilever according to Hooke's law. Forces in the range of 10^{-13} to 10^{-1} N are measured with AFM. Depending on the situation, forces that are measured in AFM include mechanical contact forces, Van der Waals forces, capillary forces, chemical bonding, electrostatic forces, magnetic forces, and so on. As well as force, additional quantities may simultaneously be measured through the use of specialized types of probe. Basically, a laser beam is incident on the top of the tip and reflected to a photodiode sensor to measure the tiny movement of the tip. A feed-back regulator responds to the changes of the path by activating a piezoelectric control, which adjusts the height of sample to balance the force between tip and surface. Topographic images of the sample are produced by translating the movement to the surface profile. This is enough to create fine

resolution in atomic scales since the resolution can be reached to 1 or 2 angstroms when AFM examined a hard surface [30].

In general, AFM modes are classified into contact (also called static) and non-contact (or variety of dynamic) modes where the cantilever is vibrated. In the beginning, AFM was designed as a contact mode technique. However, in contact mode, it is hard to obtain a good image on surfaces that are soft or a surface under liquid. Non-contact mode AFM, invented by Martin et al. [31], can solve those problems. In non-contact mode, the AFM tip vibrates close to the surface of the sample with low energy due to the weakness of van der Waals forces. However, moving the tip closer to the surface will increase the chance of sticking the tip in the water layer that covers the surface of all samples in the air, which can sharply degrade the quality of images. To improve the application of non-contact AFM, Digital Instruments (Veeco Inc.) has developed a new technique named Tapping Mode AFM (TM-AFM). In TM-AFM, larger vibration amplitude is given to the cantilever; therefore, the cantilever has sufficient energy to overcome the surface tension of the adsorbed moisture layer while vibrating through the sample. Conservative estimate predict the applied force to be in the 0.1 to 1 nano-Newton range, which is significantly lower than the force applied by the contact mode.
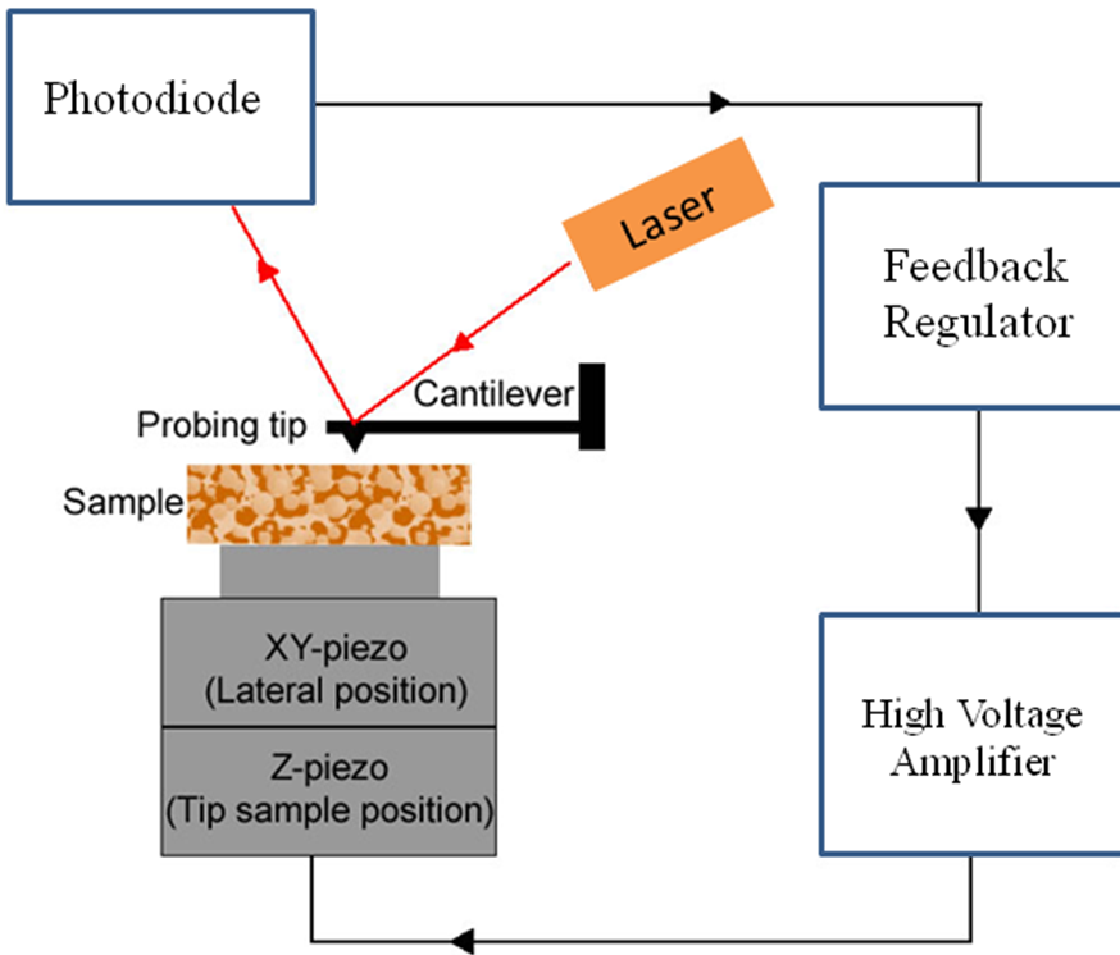
Figure 1.8 Schematic of working principle of atomic force microscopy

Nanoscope III scanning probe microscope Multi-Mode® system (Veeco Inc.) is used to collect the surface image of Ru-Ta alloy, described in Chapter 2. This instrument includes AFM, STM (scanning tunneling microscopy) and EC-AFM (electrochemical atomic force microscopy), and only AFM with J-type scanner is used in experiments. Apart from cantilever, AFM consists of the optical head and the base. The stepper-motor, the alignment screws and the scanner are installed within the base, and the sample is mounted on the top of the scanner. The optical head contains a viewing window at the top, a laser diode, a set of mirrors, and a four-quadrant positional photo detector. The cantilever holder is firmed on top of the alignment screws, with

the tip positioned over the sample. In order to align the laser beam to the top of the tip, an assistance of an optical microscope or a digital camera is used.

1.2.5 Four Point Probe

This technique was used to measure the sheet resistance of thin films in this dissertation the sheet resistance of Ru-Ta alloy thin films. It can measure resistance in the range of $10^{-5}\,\Omega$ to $10^{7}\,\Omega$. As shown in Figure 1.9, it consists of four equally spaced tungsten metal tips which are brought into contact with the surface of the sample to be measured. A high impedance current source is used to supply current through the outer two probes, while a voltmeter measures the voltage across the inner two probes to determine the sample resistivity.   If probes with uniform spacing s are placed on a film with thickness t, then the resistivity, ρ, is given by

$$\rho = (\pi t / \ln 2)(V / I)\,\mu\Omega cm \text{ (s >> t)} \qquad \text{--------------- (4)}$$

Then the sheet resistance, R_s of a thin film is

$$R_s = \rho / t = (\pi t / \ln 2)(V / I) = 4.53 * \text{V/I} \qquad \text{-------------- (5)}$$

It is important to note that R_s is independent of any geometrical dimension and is therefore a function of the material alone. The unit of R_s is $\Omega/\square$ (ohms-per-square). For Ru-Ta alloy samples, sheet resistance was measured at about 4 points and the average was taken for the plot in chapter 2.
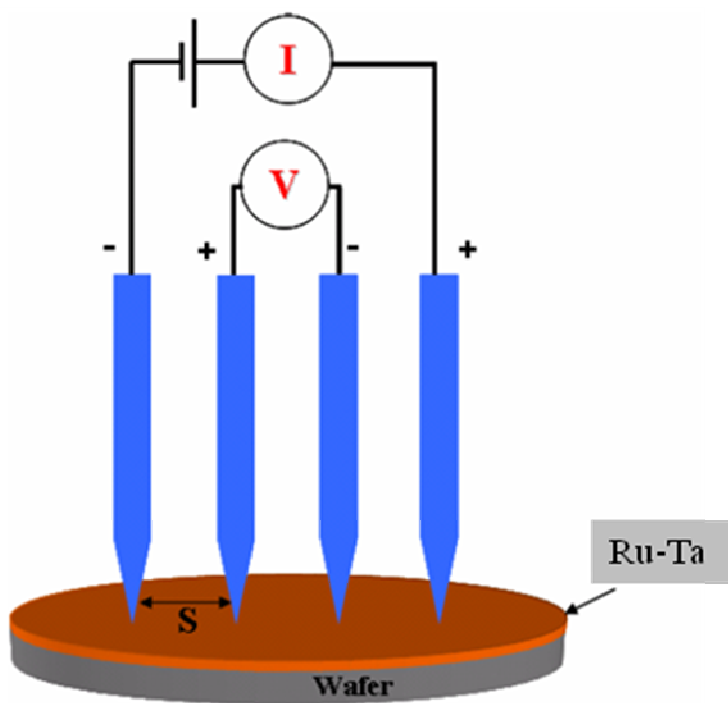
Figure 1.9 Four point probe for measuring the sheet resistance of Ru-Ta thin films

1.2.6 Electrochemical Techniques

Some of the electrochemical techniques such as open circuit potential, cyclic voltammetry etc. are extensively used for the study of Cu electrodeposition on Ru-Ta alloy thin film surfaces in chapter 3. So, it is necessary to give some basic principles about those techniques in this introduction chapter.

1.2.6 A. Open Circuit Potential

Open circuit potential (OCP) or the equilibrium potential is defined as that electrical potential of an electrode measured against a reference electrode when there is no external current or potential applied to an electrochemical cell. OCP reflects the stability of a metal when immersed in an electrolyte. Any change in the OCP value indicates the change in the nature of the metal surface.

1.2.6 B. Cyclic Voltammetry

Cyclic voltammetry is a type of potentiodynamic electrochemical measurement and the graph obtained from this technique is called cyclic voltammogram (CV). In this technique, the voltage across a working electrode like Ru or Ta is varied in a solution and the change in current is measured. Cyclic voltammetry is used for studying the redox properties of chemicals (organic and inorganic) and interfacial structures. For this measurement, a three electrode cell is used. The potential is measured between the working electrode and the reference electrode. The current is measured between the working electrode and the counter electrode. Usually Pt foil is used as the counter electrode. The CV data obtained is plotted as current (i) vs. potential (V). Negative and positive potential regions compared to the equilibrium potential are termed as "cathodic" and "anodic" respectively.
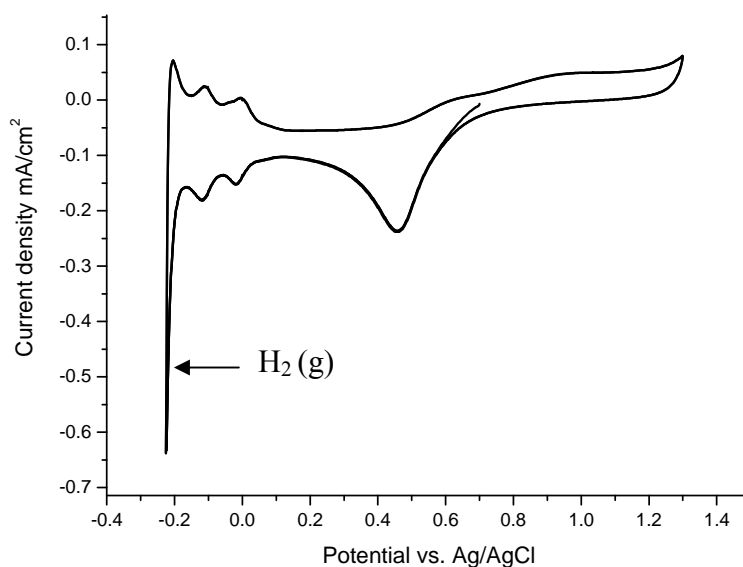
Figure 1.10 Typical cyclic voltammetry of Pt working electrode in 0.5M H_2SO_4 electrolyte

The combination of the solvent, electrolyte and working electrode material establishes the potential range (or window). A typical CV is shown in the Figure 1.10. The application of

20

cathodic and anodic potential can be explained by a simple example by immersing a noble metal electrode platinum (Pt) in sulfuric acid. A metal say Pt is immersed in a solution containing only the supporting electrolyte and then electrochemical potentials were applied to record CV. Applying cathodic potentials make the Pt metal surface to carry negative charge due to the abundant availability of electrons near the surface. The H_2SO_4 supporting electrolyte contains only hydrogen ions (protons), bisulfate anions and H^+ ions will move near the negatively charged Pt metal surface. Protons will gain electrons from Pt surface resulting in the evolution of hydrogen which is the main reaction in the cathodic regime. In contrast, if anodic potential is applied to the metal, the surface gets oxidized due to the interaction between positively charged platinum with water. However when the electrolyte contains metal ions in the solution apart from the hydrogen evolution and oxidation reactions, metal ions will interact with the electrode surface. Scanning to cathodic potential reduces the metal ions on the Pt surface. The reduction of metal ions to deposit metal is called electrochemical deposition (ECD). Scanning to positive potentials will strip any deposited metal on the Pt surface and this process is called anodic stripping.

Two different electrodeposition phenomena namely the underpotential deposition (UPD) and overpotential deposition (OPD) of metals are well known. Underpotential deposition is a specific type of electrodeposition of a metal on a foreign metal at potentials less negative than the Nernst potential of the deposition reaction. UPD will be favorable only if a strong interaction exists between the two metals. For example, Nernst potential for Cu/Cu^{2+} is around 0.06 V vs. SHE and UPD of Cu on Ru takes place prior to 0.06 V. Deposition followed by UPD or after Nernst potential is termed as OPD resulting in the deposition of bulk metal over layers. Overpotential deposition as the name signifies an additional potential or overpotential to force

the electrode reaction to proceed at a required rate. Discussion of Cu UPD and OPD on Ru-Ta alloy thin films is discussed in Chapter 3.

1.2.6 C. Tafel Plots

Tafel plot (Figure 1.11) is an electroanalytical technique from which information relating to the corrosion potential (E_{corr}) and current (I_{corr}) can be obtained. From E_{corr} and I_{corr} values, one can determine the corrosion rate, passivity and pitting susceptibility. Using a potentiostat, graph based on Butler-Volmer equation can be drawn for logarithmic of current vs. potential.
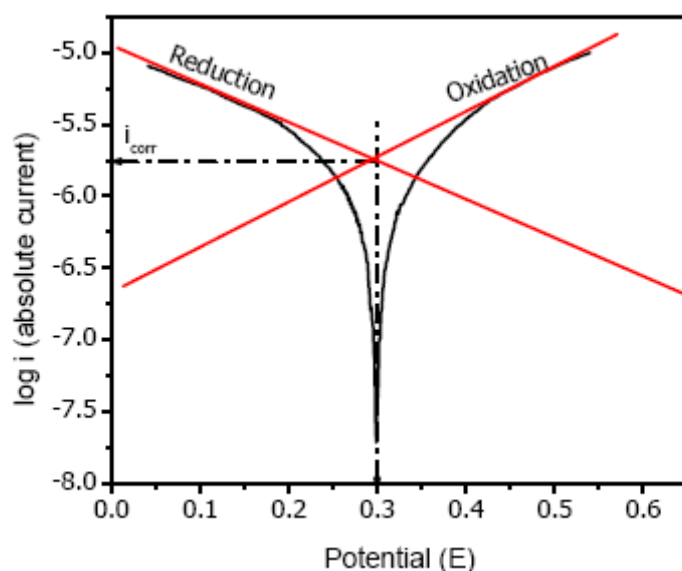
Figure 1.11 Typical Tafel plot showing E_{corr} and I_{corr} [32]

The instrument is set for a series of different parameters like potential, sensitivity, scan rate etc. The initial potential is set close to the OCP of the metal in the test solution or electrolyte and potential ranges are set to OCP ± 250 mV. In chapter 3, E_{corr} values of different compositions of Ru-Ta alloys have been investigated.

1.2.7 Rutherford Backscattering Spectrometry (RBS)

Rutherford backscattering spectrometry (RBS) is a nondestructive analytical technique used in materials characterization [33]. It is a consequence of the seminal experiment involving scattering of high-energy alpha particles from a gold foil performed by Ernest Lord Rutherford in 1911, and, as such, bears his name. Rutherford concluded that alpha particles are backscattered from a thin gold foil by interaction with the positively-charged nucleus of a gold atom. Rutherford correctly described the atom as consisting of a tiny positive nucleus orderly surrounded by negatively charged electrons in contrast to the plum pudding model of the atom as proposed by J. J Thompson [1904].
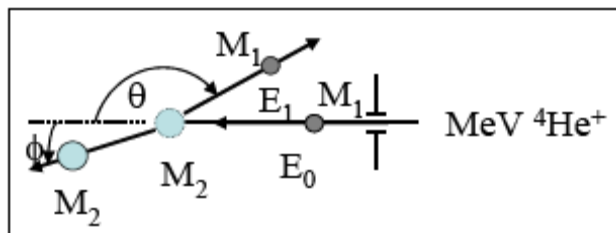
Figure 1.12 Schematic of elastic collision between an ion and a target atom.

With the development of particle accelerators, RBS became a popular technique for thin film characterization, where the energy spectrum of elastically backscattered ions is used to determine the film's parameters, i.e., composition and thickness. The schematic representation of an elastic collision is provided in Figure 1.12. The energy of a backscattered ion is determined by a standard solid-state, surface-barrier detector, which is integrated with standard pulse processing modules to yield a histogram of the backscattering events. Both the intensity and energy of the backscattered ions provide information about the near surface (up to ~0.5 μm depth for $^4He^+$ beam) of materials. The energy of the backscattered beam is proportional to the incident energy within a proportionality constant, the kinematic factor, which is characteristic of

the target and ion mass. Using conservation of momentum before and after collision and solving

the two-particle central force problem in the lab frame, the kinematic factor, K, can be derived

[33].

The experimental setup for RBS is illustrated in Figure 1.13. As mentioned earlier, the

backscattered particles are detected with a solid-state detector. These detectors are made of a

semi-conducting material and are operated much like a solid state diode under reverse bias. The

applied high voltage generates a thick depletion layer and any charge created by the radiation in

this layer is collected at an electrode. The charge, thereby, collected is proportional to the energy

deposited in the detector and therefore these devices can also yield information about the energy

of individual particle or photons of radiation. The detectors are made mostly from silicon or

germanium.
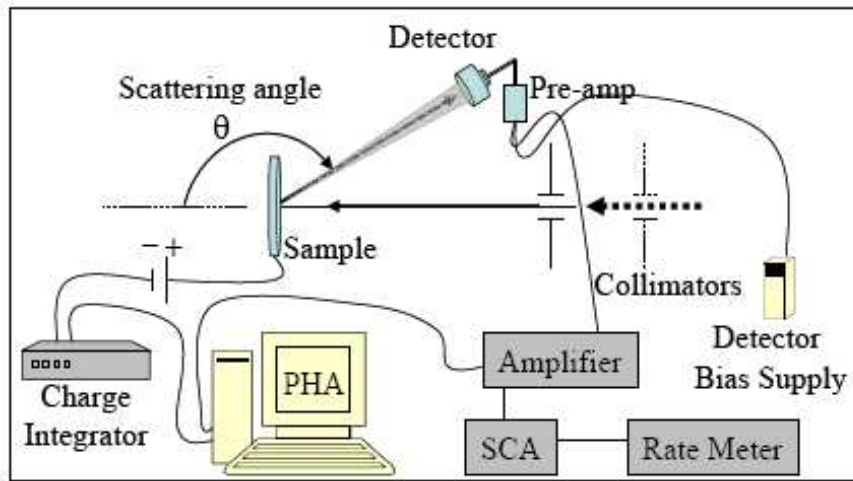
Figure 1.13 Schematic illustrating experimental set up for RBS [34]

The signal from the detector is amplified and analyzed with a multi-channel pulse height

analyzer (PHA). A computer interface module is used to plot counts as a function of channel

number, which represents energy. At near-normal beam incidence the RBS spectral peak can

provide target thin film thickness or the areal density, as atoms/cm^2. RBS spectra of Ru-Ta

alloys were obtained from UNT RBS system located in Prof. Dr. Jerome L. Duggan's lab, Physics department. The results were analyzed by Dr. Khalid Hossain.

1.2.8 X-ray Diffraction

X-ray diffraction is a very powerful determinative technique in material sciences that is used to characterize the crystal structure of thin films and bulk materials. There are various types of XRD instruments available for characterizing different materials such as, powder diffraction, single crystal etc. X-rays can be thought of as waves with wavelengths on the order of 0.1 Å to ~10 Å. The shorter the wavelength, the more energetic the wave. Because of the relatively short wavelengths of electromagnetic radiation in the x-ray region, x-rays are high energy waves and are much more penetrating compared to UV, visible, IR, or radio waves. The conversion between energy, frequency, and wavelength is governed by the well-known de Broglie relationship: $E = h\nu = hc/\lambda$, where ν is the frequency, h is Planck's constant (6.62 x 10^{-34} joule-second), c is the speed of light (2.998 x 10^{8}m/sec), and λ is the wavelength of the radiation (in m).

Generation of x-rays: When electrons strike a metal anode with sufficient energy, x-rays are produced. This process is typically accomplished using a sealed x-ray tube, which consists of a metal target (often copper metal) and a tungsten metal filament, which can be heated by passing a current through it (typically 10-15 mA), resulting in the "boiling off" of electrons from the hot tungsten metal surface. These "hot" electrons are accelerated from the tungsten filament (negative bias) to the metal target (positive bias) by an applied voltage (typically 15-30 kilovolts). The collision between these energetic electrons and electrons in the target atoms results in electron from target atoms being excited out of their core-level orbitals, placing the atom in a short-lived excited state. The atom returns to its ground state by having electrons from

lower binding energy levels (i.e. levels further from the nucleus) make transitions to the empty

core levels. The difference in energy between these lower and higher binding energy levels is

radiated in the form of x-rays. This process results in the production of characteristic x-rays (i.e.

x-rays whose energies are unique to the target metal due to the quantized nature of the electron

energy levels of each atom and the unique energies of these energy levels) [Cu Kα_1 (L$_3$ to K

electronic transition: E = 8047.78 eV, λ = 1.54051 Å), Cu Kα_2 (L$_2$ to K electronic transition: E =

8027.83 eV, λ = 1.54433 Å), Cu Kβ_1 (M$_3$ to K electronic transition: E = 8905.29 eV, λ =

1.39217 Å)].
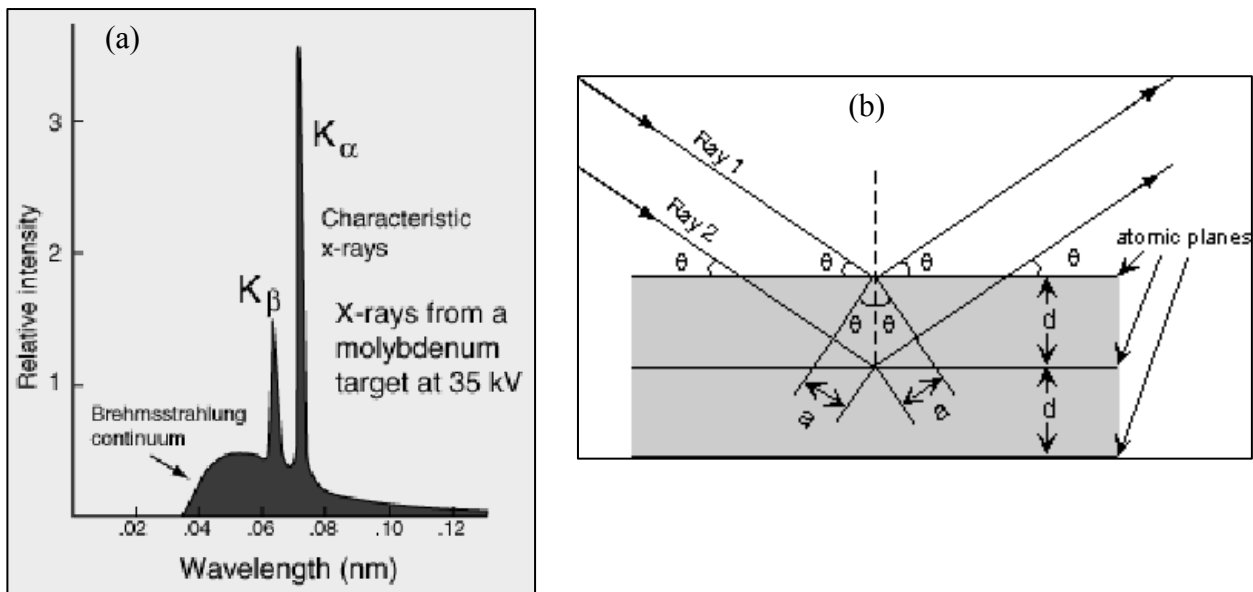
Figure 1.14 a) Characteristic x-ray from Mo target and b) schematic of Bragg's law of diffraction
[35]

Thus x-rays provide a convenient means of determining what elements are present in a

sample because of the unique wavelengths produced by each unique element. A lower energy

process that involves the interaction of electrons with the nucleus of an atom in the target metal

produces a continuum of lower intensity x-radiation over a broad energy range known as

26

Bremstrahllung. As the voltage on an x-ray tube is increased, the characteristic line spectra of the target element are superimposed upon the continuous spectrum.

X-ray diffraction: Crystals are ordered, three-dimensional arrangements of atoms with characteristic periodicities. As the spacing between atoms is on the same order as x-ray wavelengths (1-3 Å), crystals can diffract the radiation when the diffracted beams are in-phase. The Bragg equation is given as $n\lambda = 2d\sin\theta$. For a given wavelength (λ), diffraction can only occur at a certain angle (θ) for a given d-spacing. For Ru-Ta alloy samples, Rigaku Ultima III – XRD technique was used to obtain crystallographic properties. The results are described in chapter 2.

1.2.9 Transmission Electron Microscopy

Transmission electron microscopy (TEM) is a technique where an electron beam interacts and passes through a specimen. The electrons are emitted by a source and are focused and magnified by a system of magnetic lenses. The geometry of TEM is shown in Figure 1.15. The electron beam is confined by the two condenser lenses which also control the brightness of the beam, passes the condenser aperture and "hits" the sample surface. The electrons that are elastically scattered consists the transmitted beams, which pass through the objective lens. The objective lens forms the image display and the following apertures, the objective and selected area aperture are used to choose the elastically scattered electrons that will form the image of the microscope. Finally, the beam goes to the magnifying system that is consisted of three lenses, the first and second intermediate lenses control the magnification of the image and the projector lens. The formed image is shown either on a fluorescent screen or in monitor or both and is printed on a photographic film.

Figure 1.15 Geometry of TEM [36]
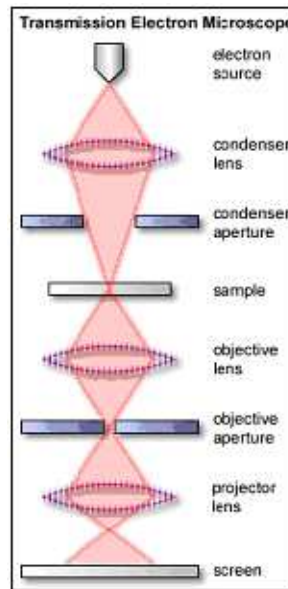
Different types of images are obtained in TEM, using the apertures properly and the different types of electrons. As a result, diffraction patterns are shown because of the scattered electrons. If the unscattered beam is selected, we obtain the bright field image. Dark field images are attained if diffracted beams are selected by the objective aperture. Also in TEM, analysis is done with EDX (energy dispersive x-ray), EELS (electron energy loss spectrum), and EFTEM (energy filtered transmission electron microscopy) etc data. In transmission microscopy, we can actually see the specimen's structure and its atomic columns, thus compositional and crystallographic information is attained.

TEM exploits three different interactions of electron beam-specimen; unscattered electrons (transmitted beam), elastically scattered electrons (diffracted beam) and inelastically scattered electrons. When incident electrons are transmitted through the thin specimen without any interaction occurring inside the specimen, then the beam of these electrons is called transmitted. The transmission of unscattered electrons is inversely proportional to the specimen thickness. Areas of the specimen that are thicker will have fewer transmitted unscattered electrons and so will appear darker, conversely the thinner areas will have more transmitted and thus will appear lighter.

28

Another part of the incident electrons, are scattered (deflected from their original path) by atoms in the specimen in an elastic fashion (no loss of energy). These scattered electrons are then transmitted through the remaining portions of the specimen. All electrons follow Bragg's law and thus are scattered according to

$$n\lambda = 2d\sin(\theta)$$ -------------- (6)

where

λ is the wavelength of the rays

θ is the angle between the incident rays and the surface of the crystal and

d is the spacing between layers of atoms.

All incident electrons have the same energy (thus wavelength) and enter the specimen normal to its surface. All incidents that are scattered by the same atomic spacing will be scattered by the same angle. These scattered electrons can be collated using magnetic lenses to form a pattern of spots; each spot corresponding to a specific atomic spacing (a plane). This pattern can then yield information about the orientation, atomic arrangements and phases present in the area being examined.

1.3 References

1. Bardeen and W. H. Brattain, *Phys. Rev.*, 71, 230 (**1948**)

2. G. Moore, "*Cramming More Components Onto Integrated Circuits,*" *Electronics*,38 (8) (**1965**).

3. http://www.icknowledge.com/history/pointcontacttransistor.gif

4. http://www.ti.com/corp/graphics/press/image/on_line/co1034.jpg

5. http://www.intel.com/idf/

6. J.P. Colinge and C.A. Colinge, *Physics of Semiconductor devices*, Kluwer Academic publisher, Boston (**2002**).

7. T. McMannus, "*Environmental Technology in Semiconductor Manufacturing- Challenges & Opportunities,*" *NSF-SRC center for Environmentally Benign Semiconductor Manufacturing Review meeting*, August (**2004**)

8. R. Rosenberg, *MRS Symposium Proceedings.*, 337, 33 (**1994**).

9. W. W. Lee, S. Russell, "*Integration Challenges of Low k Materials,*" *Future Fab Intl.* Vol. 8 (**2002**).

10. Josell, D.; Wheeler, D.; Witt, C.; and Moffat, T. P.; *Electrochemical and Solid-State Letters*, 6, **2003**, C143-145.

11. Chyan, O.; Arunagiri, T. N.; and Ponnusamy, T. *J. Electrochem. Soc.*, 150, **2003**, C347-C350.

12. Chan, R.; Arunagiri, T. N.; Zhang, Y.; Chyan, O.; Wallace, R. M.; Kim, M. J.; Hurd, T. Q.; *Electrochemical and Solid-State Letters*, 7, **2004**, G154-157.

13. Josell, D.; Bonevich, J. E.; Moffat, T. P.; Aaltonen, T.; Ritala, M.; and Lekela, M.; *Electrochemical and Solid-State Letters*, 9, **2006**, C48-C50.

14. Josell, D.; Witt, C.; and Moffat, T. P. *Electrochemical and Solid-State Letters*, 9, **2006**, C41-C43.

15. Singer, *Peter Semiconductor International*, May **2004**.

16. Goswami, Ishita; and Laxman, Ravi *Semiconductor International*, May **2004**.

17. Arunagiri, T. N.; Zhang, Y.; Chyan, O.; El-Bouanani, M; Kim, M. J.; Chen, K. H.; Wu, T. C., and Chen, L. C. *App. Phys. Letters*, 86, **2005**, 083104.

18. Chun-Wei Chen, J. S. Chen, and Jiann-Shing Jeng *Journal of The Electrochemical Society, 155*, 12, H1003-H1008 (**2008**)

19. D. Briggs, and M. P. Seah, *Practical Surface Analysis: Auger and X-Ray Photoelectron Spectroscopy*, 2nd Edition, John Wiley & Sons Ltd (**1996**).

20. T. Young, in G. Peacock (ed.), *Miscellaneous Works*, Murray, London, 1 (1855) 418

21. A. Ulman, *An introduction to ultrathin organic films*; From *Langmuir-Blodgett to Self-Assembly*, Academic Press, Inc., San Diego (**1991**)

22. A. W. Adamson, A. P. Gast, A. Wiley, *Physical Chemistry of Surfaces*, 6th Ed., John Wiley & Sons, New York (**1997**)

23. P. E. Laibinis, C. D. Bain, R. G. Nuzzo, and G. M. Whitesides, *J. Phys. Chem*. 99 (**1995**), 7663

24. A. Ulman, *Thin Solid Films* 273 (**1996**) 48-53

25. D. J. Olbris, A. Ulman, Y. Shnidman, *J. Chm. Phys*. 102 (**1995**) 6865-6873

26. Wickramashinghe, H. K. *Sci. Am.*, **1989**, 98.

27. Pool, R. *Science*, **1990**, 247, 634.

28. Binning, G.; Quate, C. F.; Gerber, C., *Phys. Rev. Lett.*, **1986**, 56, p930

29. Frommer, J.; Meywer, E. *J. Phys.*: Condens. Matter, 3, S1-S9 **1991**.

30. "Atomic Force microscope" http://en.wikipedia.org/wiki/Atomic_force_microscope.

31. Martin, Y.; Wichramasinghe, H. K. *Appl. Phys. Lett*. **1987**, 50, 1455

32. Shyam S Venkataraman "*Electrodeposition of Cu on Ruthenium Oxides and Bimettallic Corrosion of Cu/Ru in Polyphenolic Antioxidants*", M.S. Thesis, University of North Texas, (**2007**)

33. Leonard C. Feldman, James W. Mayer "*Fundamentals of Surface and Thin Film Analysis*" North Holland, New York (**1986**)

34. Khalid Hossain "*A Novel Process for GeSi Thin Film Synthesis*" PhD Thesis, University of North Texas, (**2007**)

35. B.D. Cullity "*Elements of X-Ray Diffraction*", *Addison Wesley Publishing Company*, Inc. Massachusetts\

36. http://www.mansic.eu/documents/PAM1/Giannakopoulos1

CHAPTER 2

PREPARATION AND CHARACTERIZATION OF RU-TA THIN FILMS

2.1 Introduction

Thin films of tantalum with a melting point of 3000° C have found uses in microelectronics industry in passive components for over 30 years [1]. Ta films are very stable, with elastic stress behavior up to 600° C [2], and form a tetragonal phase structure up to 750° C. Ru is also industrially important element that found usages in many fields including fuel cell catalysts and microelectronics. Ru is one of the noble metals which are called platinum group metals (PGM). Enormous studies have been performed on Ru and on the properties of its surface oxide. For instance, ruthenium tetroxide (RuO_4) is highly volatile, as is ruthenium trioxide (RuO_3). By oxidizing ruthenium (for example with oxygen plasma) into the volatile oxides, ruthenium can be easily patterned. The properties of the common ruthenium oxides make ruthenium a metal compatible with the semiconductor processing techniques needed to manufacture microelectronics. Our research group has previously studied to a great extent on Ru thin films functioning as Cu diffusion barrier in interconnect fabrication process [3-7]. Comparison between Cu deposition on 5 nm Ru/Si by electrochemical deposition (ECD) and physical vapor deposition (PVD) method has revealed facts about the interfaces. The interfacial integrity after vacuum anneal at 300° C is retained for both PVD and ECD Cu/(5nm Ru)/Si structures [3] .

At higher temperature at 450° C, the thermally induced formation of Ru silicide results in failure of Ru as diffusion barrier. Also, Ru has been studied successfully to show its ability to plate Cu directly without any seed layer. Cu under-potential deposition was also demonstrated

33

on both Ru and Ru oxide surfaces [4-5]. Also, the direct plate-ability of Cu on ultrathin Ru films (5 to 20 nm) with over 90% efficiency has been reported [6-7].

On the other hand, an alloy of Ru and Ta is found to have many applications viz. the improved thermal stability and the possibility to tune their work functions allow them to function as metal gates in CMOS devices compared to Ta alone [8]. For barrier application in interconnect fabrication process, Ru has good wettability with Cu but the barrier property of Ru alone is not so good [9-10]. Ru-Ta was studied to be another barrier candidate that has good wettability and also improved barrier property [11]. In this work, various compositions of Ru-Ta were prepared by sputtering technique and thin film characterizations were done. The thin film properties of Ru-Ta samples were studied and explained in this chapter to provide better understanding to serve as Cu diffusion barriers and to evaluate direct Cu plate-ability. Cu electroplating studies were done and explained in chapter 3.

2.2 Experiment

Sputter deposition technique (Denton Vacuum Inc.) was used to deposit both Ru and Ta on Si substrate. At first, a series of thin films of Ru and Ta with linearly varied sputtering parameters were deposited separately on Si coupons for thickness calibration purpose. The thickness information of those Ru and Ta films were obtained using profilometer (Veeco Inc.). And based on the calibration curve, the deposition parameters were optimized to co-deposit Ru and Ta to obtain different compositions of Ru-Ta alloys. The sheet resistances of Ru-Ta thin films were measured using 4-point probe instrument coupled with Keithley source meter. Crystalline studies have been made on Ru-Ta using Rigaku Ultima III XRD instrument with Cu K-alpha radiation and the spectra were taken at 5 deg angle. Surface roughness information was obtained using atomic force microscopy (AFM) and grain size was found from EM 420

transmission electron microscopy (TEM). Electrochemical data were obtained using CHI

potentiostat.

2.3 Results and Discussion

2.3.1 Sputter Deposition of Ru-Ta Alloy Thin Films on Si Substrate

Sputter deposition is a physical vapor deposition method in which deposition of thin

films is achieved by ejecting the material from its target and depositing on a substrate. Ru and

Ta targets were purchased from Haraeus Inc. and the simultaneous sputtering of Ru and Ta was

done using two power sources radio frequency (Ru) and direct current (Ta). Figure 2.1 shows

the picture of Denton vacuum sputtering tool that was used to deposit the thin films. The

thickness of Ta target was 0.25 inch and that of Ru was 0.375 inch. A roughing pump which was

used to create the vacuum in milli-Torr range was connected in turn to Turbo pump to create

higher vacuum.

Figure 2.1 Denton vacuum sputtering tool
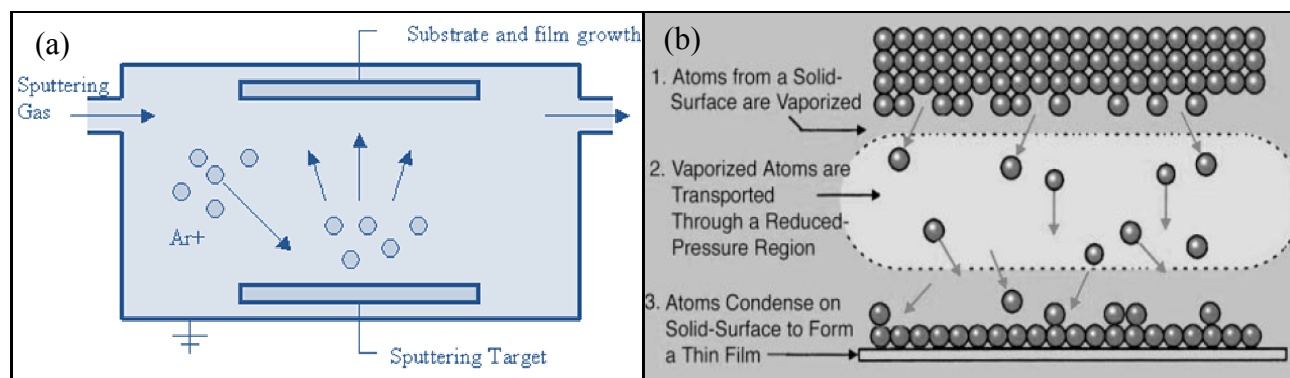
Figure 2.2 (a) Schematic of sputtering process, (b) three step deposition process [12]

The vacuum maintained in the sputtering chamber was about 10^{-6} Torr and the Ar feed gas pressure during sputtering was 5×10^{-3} Torr. The flow rate of Ar feed gas maintained was 16 sccm. The time and power of deposition were adjusted to deposit various compositions of Ru and Ta on Si substrate. Figure 2.2 (a) shows the schematic of sputtering process in which the Ar gas is ionized by either DC or RF potential and the ions which are accelerated towards the target by the magnetic field bombard on the target. The atoms of the target that are ejected due to the bombardment of Ar^+ ions deposit on the substrate as explained in Figure 2.2(b). The thin films were deposited for about 50-100 nm thickness.

2.3.2 Rutherford Backscattering Spectrometry (RBS) of Ru-Ta Oxides

The Ru-Ta samples prepared were characterized by RBS technique to estimate the composition. Four samples were prepared at first named RT-1, RT-2, RT-3 and RT-4 with expected composition of Ru, 90%, 80%, 70% and 60% respectively. Figure 2.3 shows experimental RBS spectra of Ru, Ta and RT samples. The arrows shown in the figure represents the position of backscattered energy from Si and O present on the sample. The atomic composition of Ru-Ta samples were obtained from simulation of raw RBS spectra using a standard computer code, SIMNRA. Figure 2.4 shows the overlay of experimental and simulated

spectra of sample RT-3. The simulated spectrum overlaps with experimental one very well and

it was identified that the samples are composed not only of Ru and Ta but also of their oxides.

For RT-3, the compositions estimated are 44% Ru, 30% oxide, and the remaining Ta. On all the

samples, a first Ru-only layer was deposited for about 5 nm thickness for the purpose of having

better adhesion of Ru-Ta alloy film.
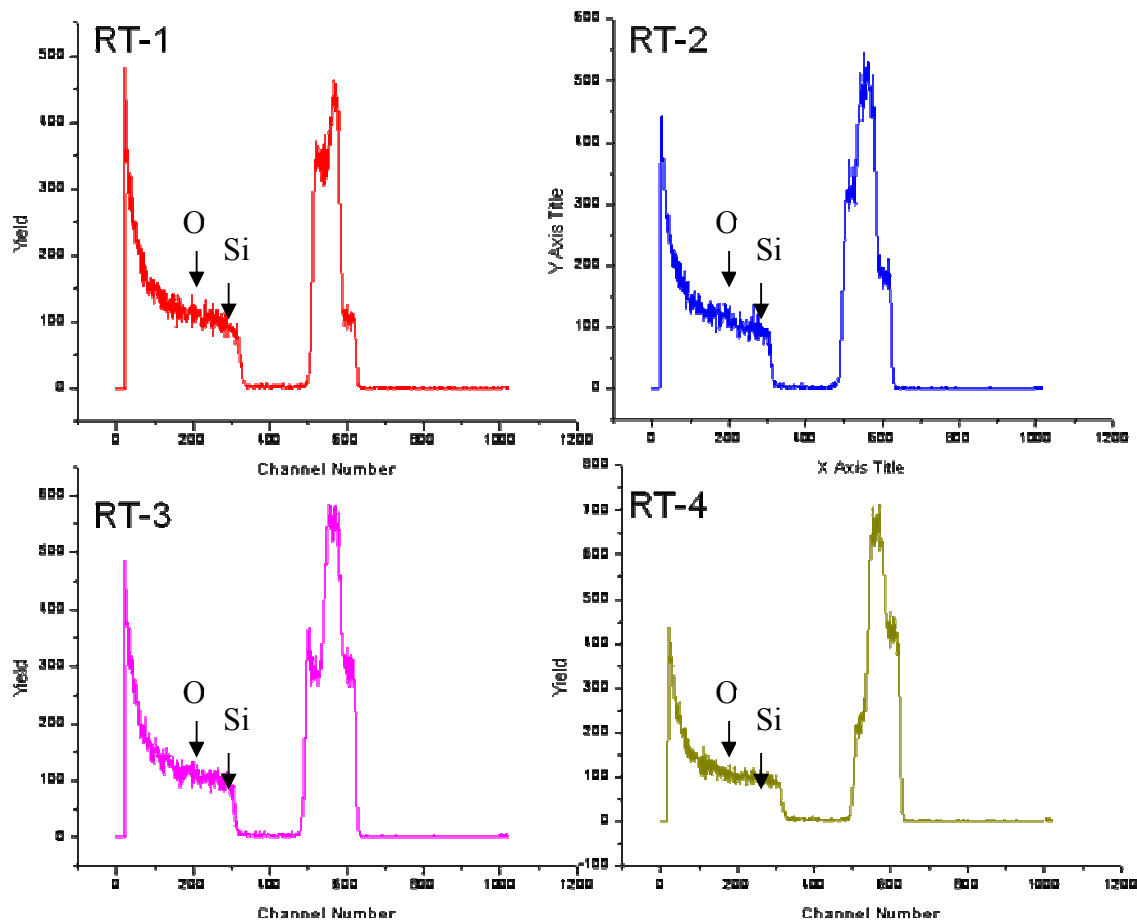
Figure 2.3 (a) Experimental RBS spectra of first set RT oxide samples

37
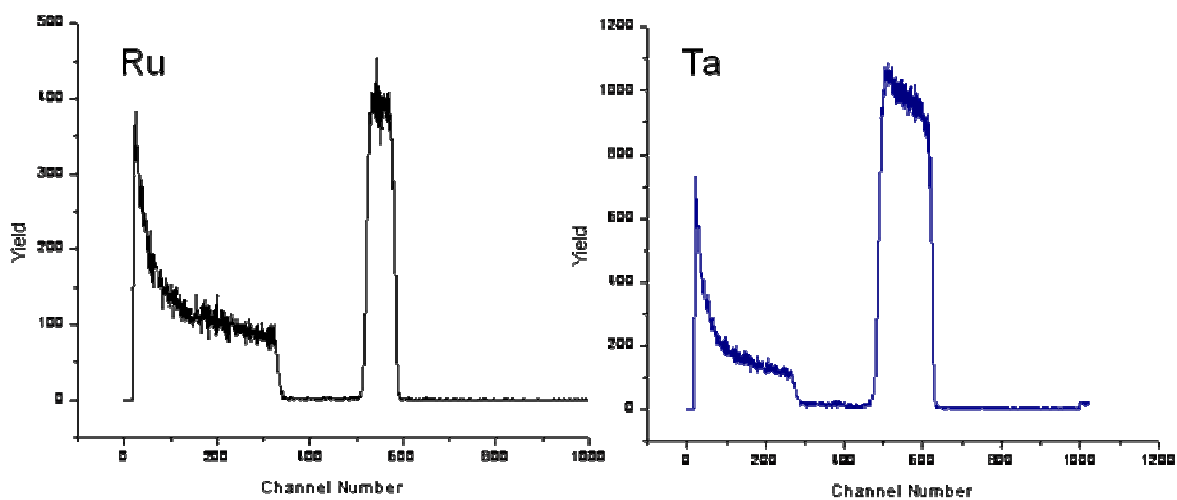
Figure 2.3 (b) Experimental RBS spectra of pure Ru and Ta sample
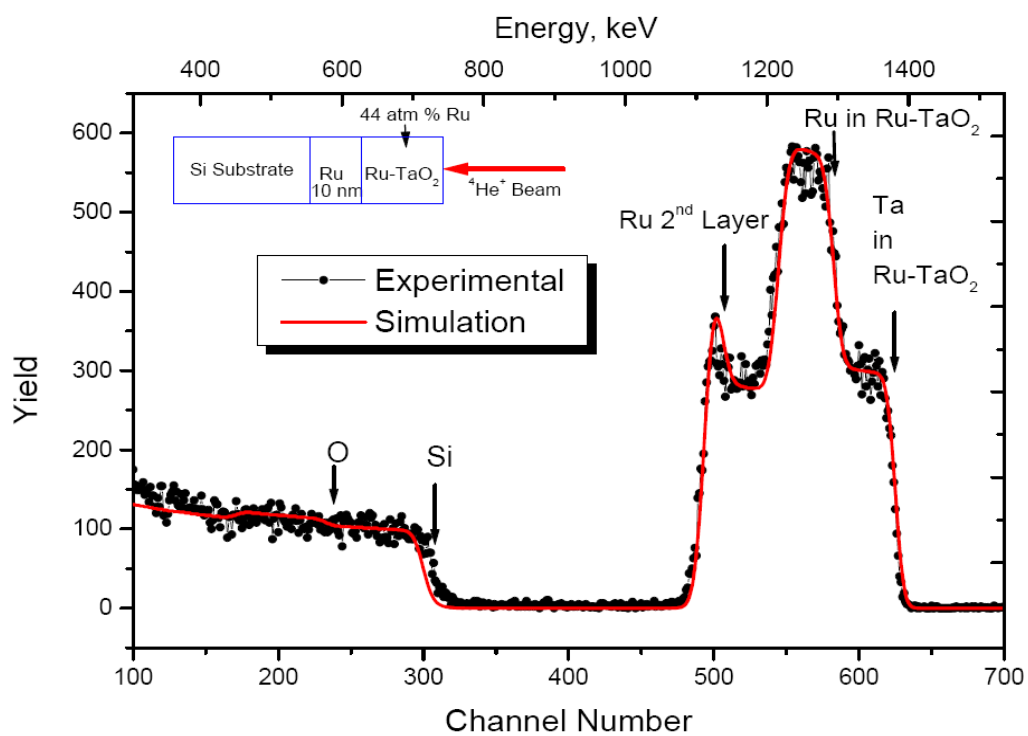
Figure 2.4 Experimental and simulated RBS spectra of sample RT-3 showing the presence of oxides on the surface

From the simulation, it was determined that the samples are composed of oxide. Prior to

depositing another set of oxide-free Ru-Ta samples, it was necessary to evaluate some of the

electrochemical properties of this oxide samples. As a result, preliminary experiments to

evaluate the surface oxide reduction were done using cyclic voltammetry in sulfuric acid

solutions. Following section describes the method of testing the electrochemical properties of

Ru-Ta oxides including the characteristics of Cu electrodeposition.

2.3.3. Electrochemical Characterization of Ru-Ta Oxides

The oxidation and reduction properties of any metal or metal alloy substrate will provide

information about its electrochemical behavior. For example, Ru is known to form native oxide

upon exposure to air and this oxide which is a conductive one can be electrochemically reduced

in 0.5 M sulfuric acid solution. Figure 2.5 shows the CV results of Ru and Ta in sulfuric acid

solution. It can be seen that the Ru native oxide reduction begins at ~0.35 V and the peak

reduction potential is located at +0.12 V vs. Ag/AgCl reference electrode.
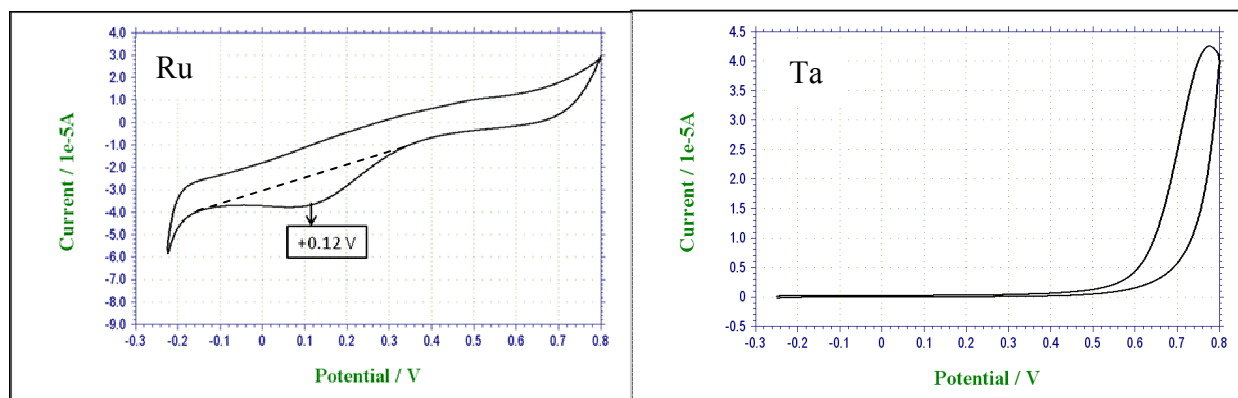
Figure 2.5 Cyclic voltammetry of air exposed Ru and Ta in 0.5 M sulfuric acid

On the other hand, Ta electrode does not show any oxide reduction peak in the provided

potential window region due to its high inert nature of surface native oxide. But it starts to

oxidize at +0.55 V. Similarly Ru-Ta oxide samples were also subjected for electrochemical

behavioral study. Figure 2.6 shows the CV result of RT oxide samples in sulfuric acid solution.

It can be clearly seen from the CV that the charge density in the cathodic region is higher for

sample that has higher amount of Ru and it decreases as the Ta content increases. This suggests

that the passivity for electrochemical behavior of Ru-Ta oxide electrodes increases as the amount

of Ta increases. The cathodic reduction current is proportionate to the amount of Ru present on

the sample.
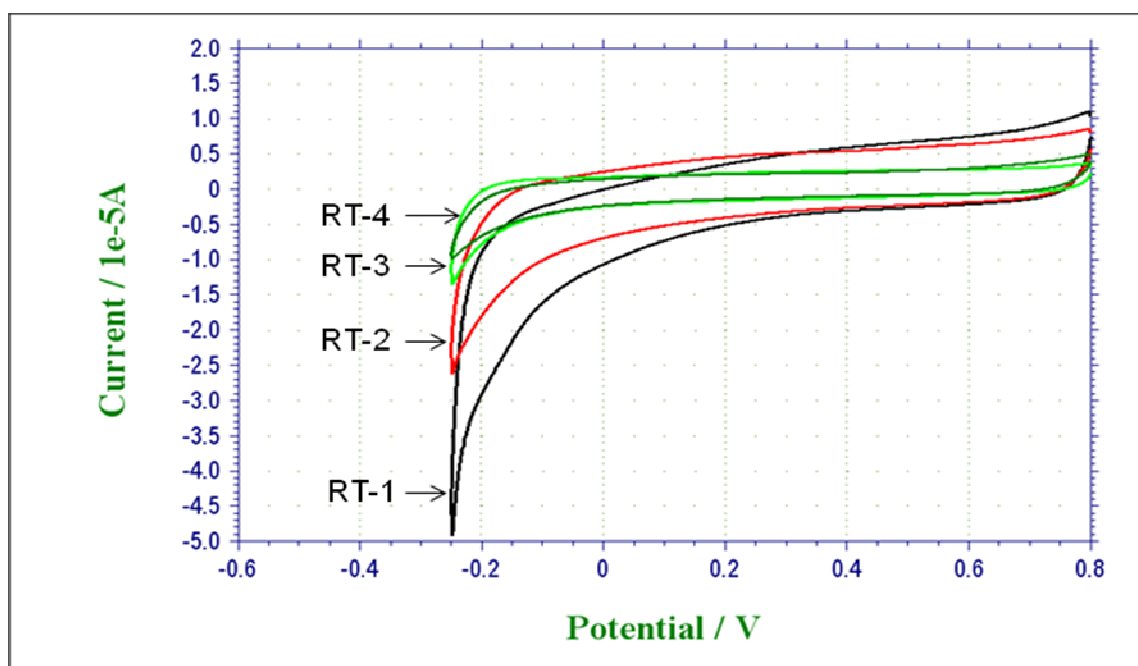
Figure 2.6 Cyclic voltammetry of as-deposited Ru-Ta samples in 0.5 M sulfuric acid

The presence of oxide in Ru-Ta samples will cause the conductivity to increase. In order

to test the improvement in the electrochemical activity for Ru-Ta oxide electrodes, two surface

treatments were adopted to remove / treat the oxide from the surface viz. forming gas and NaOH

treatments. Figure 2.7 shows the evolution of open circuit potential (OCP) in sulfuric acid

solution for both forming gas and caustic NaOH treated samples. The OCPs of as-deposited

samples also were overlaid for comparison. For all the treated and as-deposited samples, the

OCP values are gradually decreasing beginning from high positive potential for Ru to negative

most potential for Ta. This suggests that the nature of electrode surface shifts towards Ta as the

content of Ta increases in the samples.
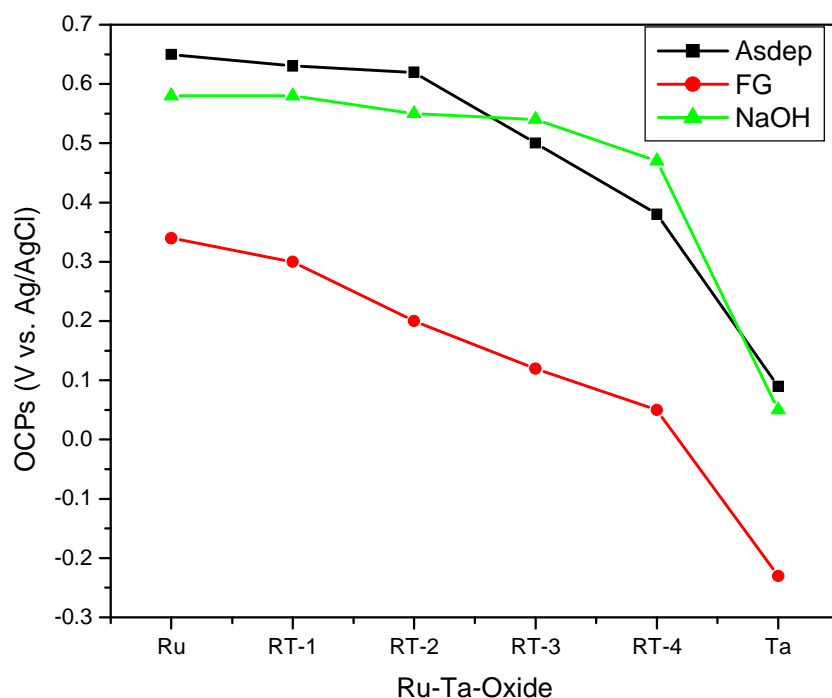
Figure 2.7 OCPs of as-deposited, forming gas and NaOH treated Ru-Ta oxide samples in 0.5 M
sulfuric acid solution

It was also observed that, the OCPs are much negative for forming gas treated samples

than the untreated and NaOH treated samples suggesting that the surface oxide has been reduced

to a large extent and the OCP being dominated mostly by metallic behavior. Not the slight

alkaline but caustic NaOH is highly alkaline solution that is known to be corrosive for metal

oxides such as Ta oxide [13]. The dissolution of surface oxide in caustic solution can be

observed from the in-situ measurement of OCPs. After treating the samples in NaOH solution for about 30 min, the samples were sonicated in DI water for 3 min and were subjected to OCP measurement in 0.5 M sulfuric acid solution. The data in Figure 2.7 shows that the OCPs have slightly shifted negative compared to as-deposited samples suggesting that some of the native oxides have been dissolved. A crossover was observed between the OCPs of as-deposited and NaOH treated samples when Ta content is higher. For RT-3 and RT-4, the OCPs shifted above that of as-deposited samples indicating that more of the surface Ta oxides have been dissolved in NaOH solution and the surface nature shifting a little towards Ru.

Our research group has previously demonstrated that copper electrodeposition on Ru and its oxide can be done successfully [4, 6] without the need of a Cu seed layer. Also the phenomenon of Cu under-potential deposition (UPD) was observed on Ru substrate. Cu UPD will be explained in detail in chapter 3. While Ru has better Cu plateability, Ru-Ta oxide samples were subjected for the study of Cu electrodeposition characteristics.
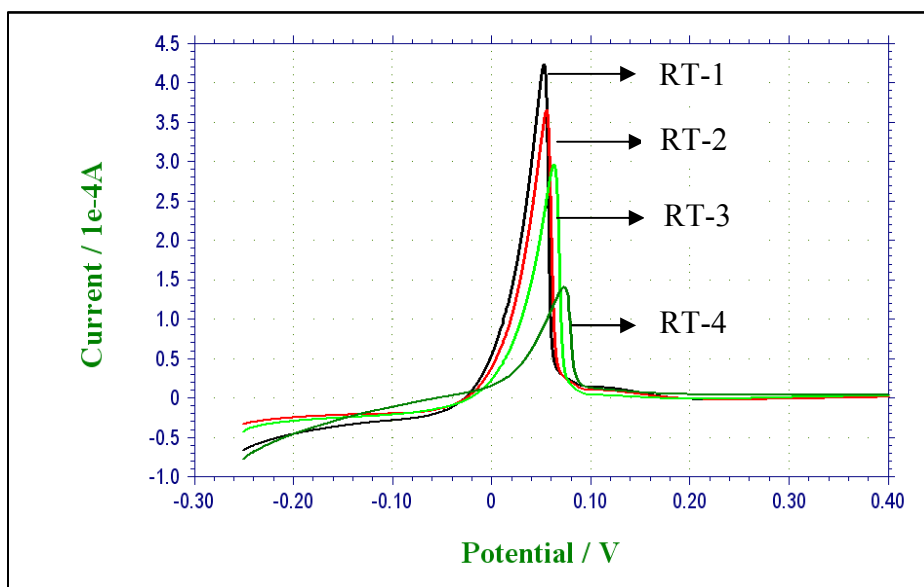
Figure 2.8 Anodic stripping of Cu from NaOH treated Ru-Ta oxide samples

42

It was observed using cyclic voltammetry that, Cu electrodeposition was poor on as-deposited samples due to the presence of oxide on the surface. Figure 2.8 shows the anodic part of cyclic voltammograms in 2mM $CuSO_4$/0.5M H_2SO_4 (Cu UPD) solution of all four Ru-Ta oxide samples after treatment in NaOH solution. Cu electrodeposition was found to be improved after NaOH solution treatment.

It was observed that the anodic stripping current of Cu oxidation was highest for RT-1 (0.4 mA/cm^2) and as the Ru content is decreased, the stripping current also is decreased indicating that the amount of Cu deposited during cathodic potential sweep is decreased when Ta content is increased.
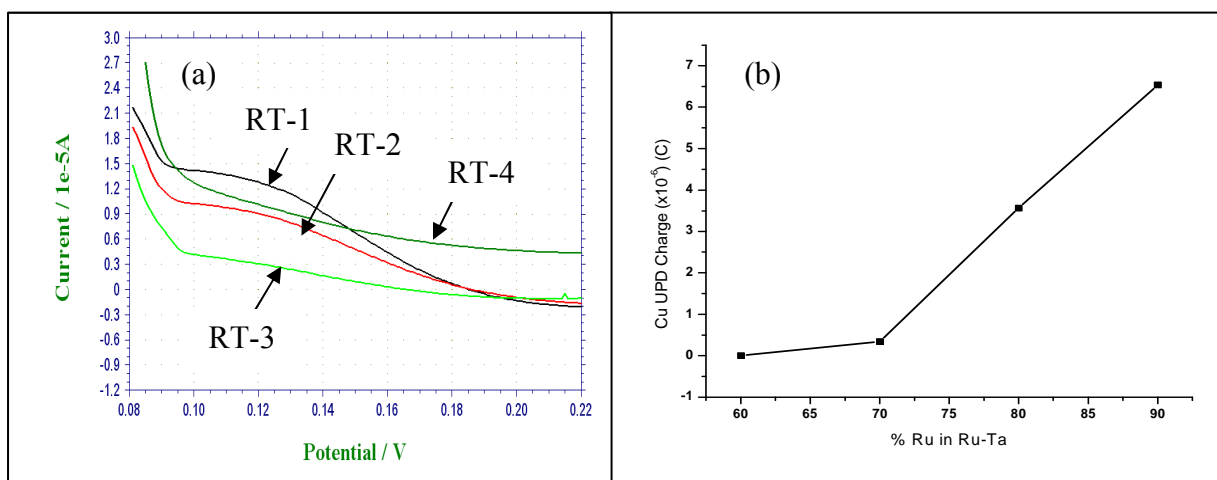
Figure 2.9 (a) Anodic UPD stripping current from cyclic voltammetry and (b) the plot of UPD charge vs. RT samples

Cu UPD stripping peak observed for the NaOH treated RT samples is shown in Figure 2.9a. The plot of UPD charge vs. RT samples is shown in Figure 2.9b. For up to 20% Ta present on the film, the underpotential deposition of Cu was still observed and the UPD charge density appears to decrease linearly with the decrease in Ru content. For RT-1 and RT-2, the UPD charge was about 6.54 μC (0.01 monolayer) and 3.5 μC (0.005 monolayer) respectively

indicating the decrease in UPD for decrease in Ru content. For the rest of the samples, they were almost zero.

In order to have Ru-Ta alloys without any oxides in the film, a second of samples were prepared more carefully preventing any oxygen leakage into the sputtering chamber. Since the UPD phenomenon was observed on the first set of samples having Ta up to 20%, this time four more samples were prepared with higher amount of Ta starting from 30%, 40%, 50% and 60% and were named as RT-7/3, RT-6/4, RT-5/5 and RT-4/6 respectively. Figure 2.10 shows the RBS spectra obtained on those samples to verify the composition.

2.3.4 RBS Analysis of 2nd set Ru-Ta Samples
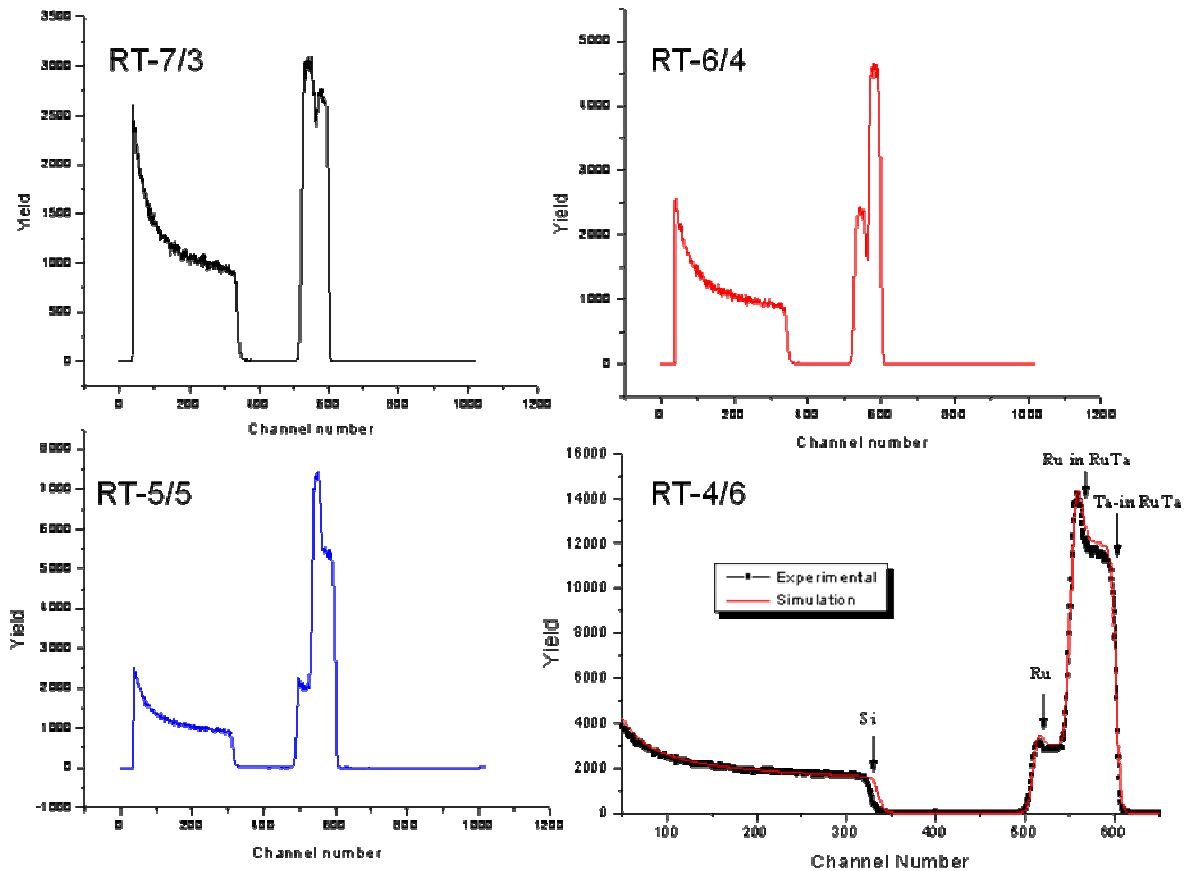
Figure 2.10 RBS spectra of II-set Ru-Ta samples

44

Sample	RBS Data Composition
RT-4/6	40/60
RT-5/5	47/53
RT-6/4	59/41
RT-7/3	70/30

Table 2.1 Compositions of Ru-Ta from RBS analysis

2.3.5 Sheet Resistance Measurement Using Four Point Probe

Sheet resistance is defined as the electrical resistance of a square sheet of a film. It is independent of the size of the square, but depends only on the film resistivity and the thickness of the film. Refer to chapter 1 for more theory and experimental details. The thickness of the films was around 100nm and these films are quite adhesive on Si substrate. Figure 2.11 shows the sheet resistance data measured by four point probe for a series of fresh deposited, air exposed samples, forming gas treated Ru-Ta films. For fresh deposited RT films sheet resistance starts to increase for 30% Ta and it reaches the maximum of 29 Ω/sq for 40% Ta content. Sheet resistance decreases for samples that have more than 40% Ta as it goes towards Ta. As Ta is very well known for its oxidation tendency, it will quickly be oxidized upon exposure to atmosphere and forms a defective layer of Ta-O and the thickness of the oxide layer will be more for samples that have increased Ta content. Over time, as the samples are kept in atmosphere, Ta oxide will keep on growing and as a result, the sheet resistance of aged samples increased.
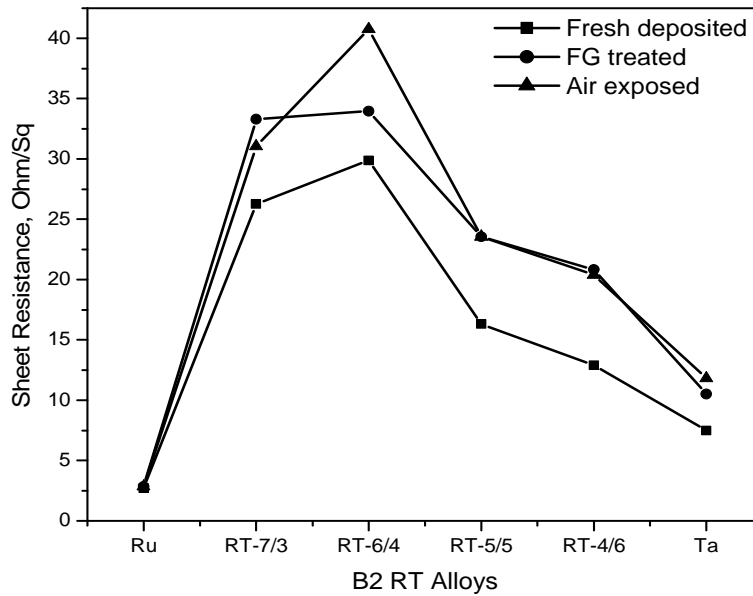
Figure 2.11 Sheet resistance values of fresh, aged and forming gas treated Ru-Ta samples

	Ru	RT- 7/3	RT-6/4	RT-5/5	RT-4/6	Ta
Resistance , Ω	0.6	5.8	6.6	3.6	2.85	1.58
Sheet Resistance, R_s (x 4.53), Ω/sq	2.72	26.27	29.89	16.31	12.91	7.15
Sheet resistance for Aged samples	2.72	6.85x4.53 = 31.03	9.0x4.53 = 40.77	5.2x4.53 = 23.55	4.5x4.53 = 20.39	12.1

Table 2.2 Sample sheet resistance calculations

The increasing trend of sheet resistance when two dissimilar metal atoms are sputtered together is reasonable because Ta atoms can be considered as impurity atoms to diminish the degree of crystalline perfection of the pure Ru metal. The Ta atoms will carry an effect of electric charge that is different from that of Ru and thus serving as source of electron scattering [14]. This scattering will hinder the movement of electrons and results in increase in resistivity.

46

The samples were treated with forming gas (95% Ar + 5% H$_2$) at a temperature of 400° C for 15 min in order to reduce the surface oxide. The resistivity of these forming gas treated samples found to increase slightly more than the fresh deposited films for samples that have low Ta content. This may be due to the formation of ruthenium silicide (Ru$_x$Si$_y$) at the interface of Ru and Si substrate at higher temperature. For samples that have >30% Ta, the resistivity is found to increase a little higher than the as-deposited samples. It was observed, for the air exposed RT-3 sample sheet resistance has increased to quite a higher value to 40 Ω/sq.

2.3.6 XRD Characterization of Ru-Ta alloys

It is important to know the crystallinity of Ru-Ta thin films for the purpose of serving as Cu diffusion barriers. Previous studies on Ru barrier film shows a columnar microstructure on 20 nm Ru but amorphous structure on 5 nm Ru [4,5,7]. If the barrier layer is amorphous, then the Cu atoms diffusion is prevented to a greater extent due to the absence of clear grain boundaries through which Cu might diffuse at elevated temperature if present. Figure 2.12 shows the XRD patterns of Ru and RT alloy thin film samples. Ru has atomic plan reflections corresponding to hexagonal close packed (HCP) structure and the miller indices are (100) at 2θ = 38.4°, (002) at 44°, (101), (102) and (103) at angles shown in the figure. For RT-7/3 sample, we observed that there was a decrease in peaks intensity and broadening of peak widths in the XRD patterns. This suggests that the grain size of RT-7/3 has been decreased and we also observed that the peaks shifted slightly to a lower angle indicating that the lattice size is increased. For higher RT-5/5 sample, the peak at lower 2θ angles has become too broad indicating the crystal phase is dominated by Ta.
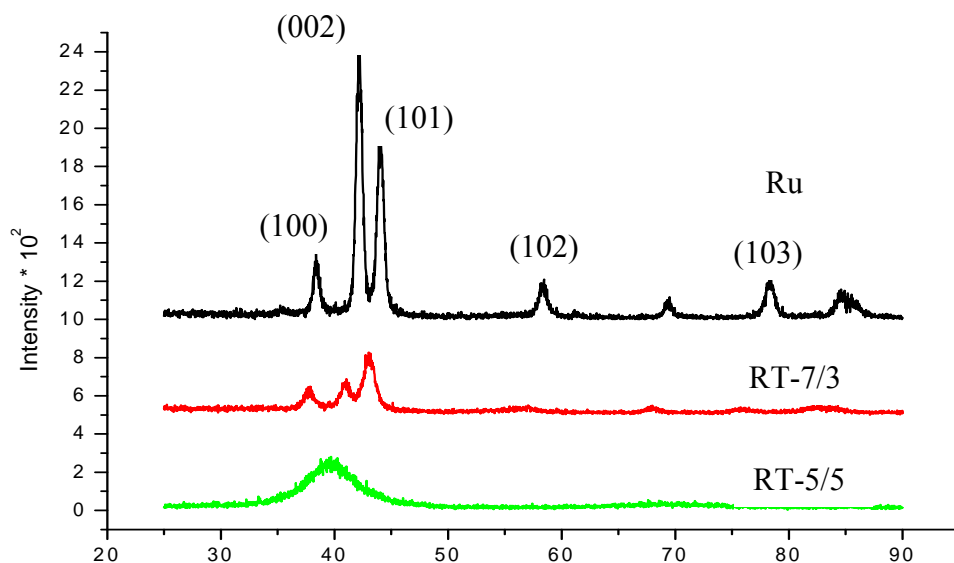
Figure 2.12 X-ray diffraction patterns of Ru and RT samples.

2.3.7 Atomic Force (AFM) and Transmission Electron Microscopy (TEM) Characterization

NaOH etching of Ru-Ta samples was found to dissolve the surface oxide mostly Ta oxide and the surface is mostly dominated by Ru particles. This was evident from the appearance of Cu bulk deposition and stripping peak resembling pure Ru electrode (refer section 3.3.2.3, Figure. 3.10).
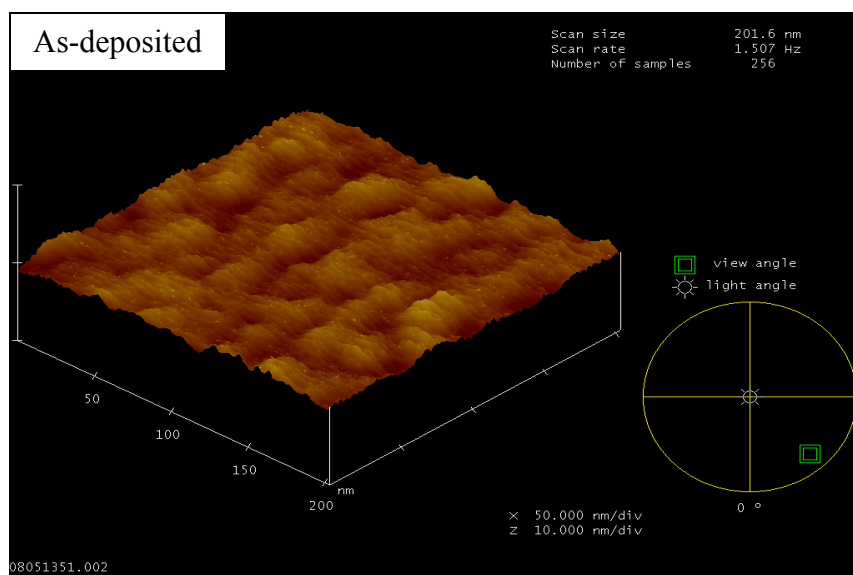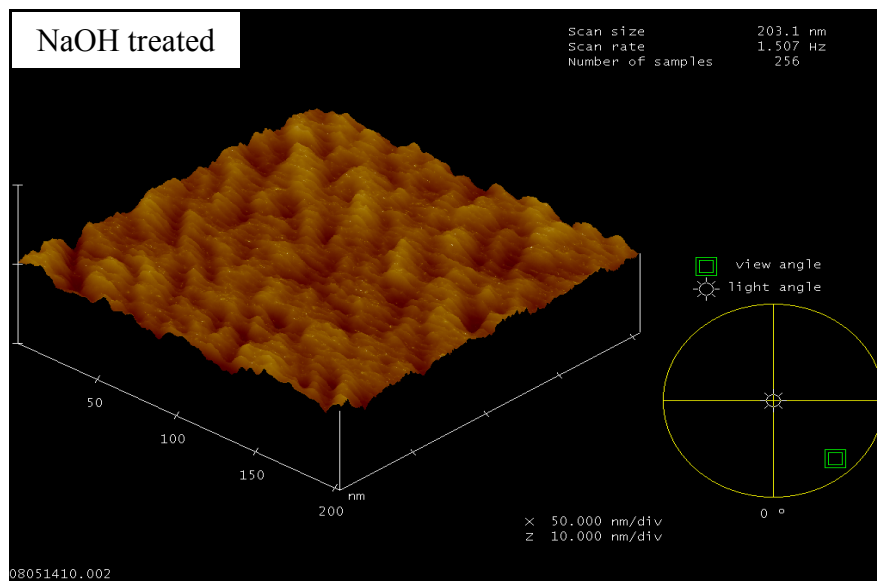
Figure 2.13 AFM image of as-deposited RT-5/5 sample and after NaOH etching for 25 min

Similar kind of surface treatments and their effect on Cu electrodeposition characteristics is also studied and documented in chapter 3 which deals with deposition on Ru-Ta as opposed to this chapter that dealt with deposition on Ru-Ta oxides. It is important to know if the NaOH treatment etches away all the Ta oxide and Ta particles from both the surface and bulk. The reason behind this requirement is to make sure the thin film still consists of both Ru and Ta together which basically is a better Cu diffusion barrier than either one alone. Hence, AFM in contact mode was used to identify the surface morphology of Ru-Ta films before and after NaOH etching. The surface roughness information was expected to be helpful to identify to some extent the complete or partial removal Ta micro-particles. Figure 2.13 shows the AFM image of sample RT-5/5 as deposited and after NaOH etching for 25-30 min. The surface roughness was calculated to be 0.45 nm for as-deposited sample and 0.47 for sample that has undergone etching process. There was only a slight increase in roughness for about 0.2 Å and this suggests that the etching process might not have removed Ta particles completely.
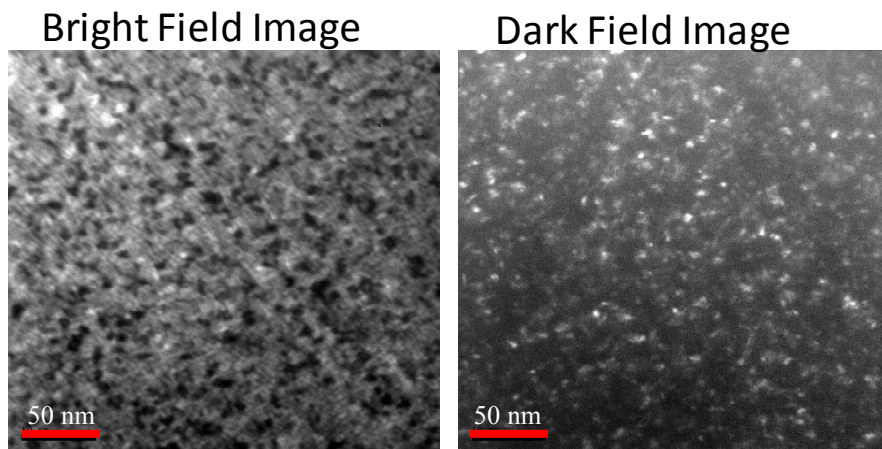
Figure 2.14 TEM bright field (a) and dark field (b) image of RT-7/3

TEM is one of the best techniques for examining the microstructure of Ru-Ta alloys, firstly because it is capable of producing small probe sizes for the crystallographic examination of individual grains or domains and secondly because the stronger interaction between electrons and the sample, relative to that of x-rays, enhances electron diffraction and thus facilitates observation of weak diffraction signals. Additionally, the other imaging techniques that are available in TEM can provide microstructural information that can be directly correlated to crystallographic information. Figure 2.14 shows the bright field and dark field images of RT-7/3. It can be seen from the images that the alloy thin film is composed of many small grains of sizes in the range of about 10 – 20 nm. Compared to a Ru sputter deposited thin film which has the grain size of about 25 - 50 nm, the Ru-Ta has resulted in decreased crystallinity.
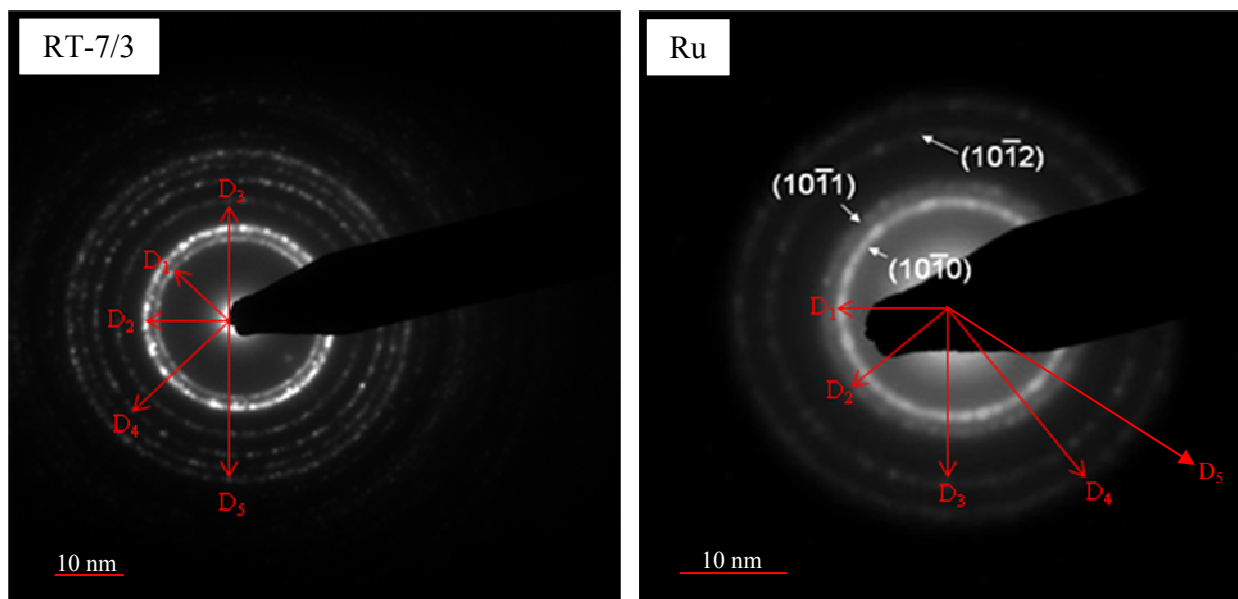
Figure 2.15 Selected area diffraction patterns of RT-7/3 and Ru

	Ru	RT-7/3	D Ratios for Ru	D Ratios for RT-7/3
D$_1$	10	10	$\bar{}$	$\bar{}$
D$_2$	10.96	11.93	0.912	0.838
D$_3$	15.8	15.64	0.633	0.639
D$_4$	18.71	18.71	0.534	0.534
D$_5$	24.67	20.64	0.405	0.484

Table 2.3 Interplanar distances and the ratios for Ru and RT-7/3
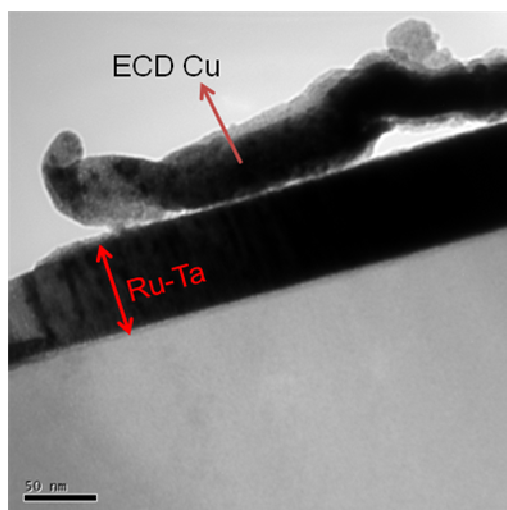
Figure 2.16 Cross sectional TEM image of electrodeposited Cu/RT-7/3

A typical TEM electron diffraction pattern of RT-7/3 sample is shown in fig. 2.15 along with that of Ru. Comparing the interplanar spacings from the diffraction rings of Ru with that of RT-7/3, it shows that the ratios D_1/D_3, D_1/D_4 for both Ru and RT-7/3 are similar but they are different for D_1/D_2 and D_1/D_5. The differences are likely due to the diffusion of Ta atoms into Ru crystallites to some extent resulting in different d-spacings. This change in d-spacing is also supported by the lower angle peaks shift in XRD spectra. Figure 2.16 shows the cross-sectional image of RT-7/3 that has a thin film of electrodeposited Cu. It was observed that the thickness was 50 nm.

2.4 Conclusion

Thin films of various compositions of Ru-Ta oxide and Ru-Ta alloy were deposited on silicon wafer and sputtering parameters were optimized to yield a thickness in the range of 50-100 nm. Atomic percentage of Ru and Ta were obtained using RBS and observed the presence of oxides in first and not in the second set of samples. Electrochemical characterizations including Cu electrodeposition were done on Ru-Ta oxide samples using cyclic voltammetry and observed that the under-potential deposition of Cu was appearing only after removing the surface Ta oxide by caustic NaOH treatment and it does appear only for samples that contain Ta up to 20%. Cu UPD charge was linearly decreasing for decreasing amount of Ru. Second set of Ru-Ta samples contain no detectible amount of oxides verified by RBS and the crystalline studies by XRD suggests that the pure crystallinity of Ru has been diminished due to the presence of co-sputtered Ta atoms for sample that contain ~30% Ta (RT-7/3). Diffracted peaks for RT-7/3 resemble pure Ru but peak broadening and peak shifting to lower angle suggests that the grain size has been decreased with increased lattice parameter because of substitution of Ta atoms in Ru crystallites. AFM results provide surface roughness information and hypothesize that there

52

must not be complete removal of Ta micro-particles from the thin film after NaOH etching. Cross-sectional TEM image provides thickness information of Ru-Ta film and more importantly it evinces the grain size which was around 10-20 nm for RT-7/3 sample. As a whole, the thin film surface properties have been studied for Ru-Ta oxide and oxide free samples for further evaluation on electrochemical Cu deposition and the results constitute chapter 3.

2.5 References

1. W.D. Westwood, N. Waterhouse, P.S. Wilcox, *Tantalum Thin Films*, Academic Press, London, **1975**, p. 406.

2. L.A. Clevenger, A. Mutscheller, J.M.E. Harper, C. Cabral Jr., K. Barmark, J. *Appl. Phys*. 72 (**1992**) 4918.

3. Tiruchirapalli N. Arunagiri, Yibin Zhang, Oliver Chyan, Moon J. Kim, and Trace Q. Hurd *Journal of The Electrochemical Society,* 152 (11) G808-G812 (**2005**)

4. O. Chyan, T. N. Arunagiri, and T. Ponnuswamy, *J. Electrochem. Soc.*, 150, C347 (**2003**).

5. Y. Zhang, H. Long, T. N. Arunagiri, O. Ojeda, S. Flores, O. Chyan, and R. M. Wallace, *Electrochem. Solid-State Lett.*, **7**, C107 (**2004**)

6. T. N. Arunagiri, Y. Zhang, O. Chyan, M. El-Bouanani, M. J. Kim, C. T. Wu, L. C. Chen, and K. H. Chen, *Appl. Phys. Lett.*, **86**, 083104 (**2005**)

7. R. Chan, T. N. Arunagiri, Y. Zhang, O. Chyan, R. M. Wallace, M. J. Kim, and T. Q. Hurd, *Electrochem. Solid-State Lett.*, **7**, G154 (**2004**)

8. H. Zhong et al, *IEDM Tech. Dig*. **2001**, pp. 467

9. C-C. Yang, et al., *Proc. of IITC* **2006**, pp.187-189

10. M. Abe, et al., *Proc. of IITC* **2007**, pp.4-6

11. Kenichi Mori, Kazuyuki Ohmori, Naoki Torazawa, Shuji Hirao, Syutetsu Kaneyama, Hayato Korogi, Kazuyoshi Maekawa, Shoichi Fukui, Kazuo Tomita, Makoto Inoue, Hiroyuki Chibahara, Yukari Imai, Naohito Suzumura, Koyu Asai and Masayuki Kojima **2008** *IEEE*

12. Kiyotaka Wasa, Shigeru Hayakawa "*Handbook of Sputtering Deposition Technology*" Noyes Publications, Westwood, New Jersey, USA.

13. ASM Handbook, Vol. 13, Corrosion. *ASM International, MetalsPark*, (**1993**) p. 725.

14. L. I. Maissel, in *Handbook of Thin Film Technology*, edited by L. I. Maissel and R. Glang, *McGraw–Hill*, New York, **1983**, p. 13-3.

CHAPTER 3

ELECTRODEPOSITION OF CU ON RU-TA THIN FILMS

3.1 Introduction

Copper (Cu) interconnects have been widely used for advanced ultra large scale integrated circuits (ULSIs) to minimize the resistance of wiring. When Aluminum was used as a interconnect material, the metal patterning was formed by techniques such as photoresist masking and plasma etching. Since Cu cannot be patterned by that process due to the lack of volatile Cu compounds, it is done by a process called dual-damascene process in which a dielectric layer (SiO_2 or low-k dielectrics) is first deposited and etched with fluorocarbon gas plasma to create trenches and vias. A thin layer of TaN/Ta is deposited conformally inside the trench and via followed by depositing a Cu seed layer by physical vapor deposition technique. Next, the trenches/vias are bulk filled with Cu from bottom up by bulk electroplating followed by chemical mechanical planarization (CMP) process to remove the excess Cu. For the integration of Cu interconnects with low-k dielectrics, one of the most challenging issues is to achieve a highly reliable performance against stress-induced voiding, electromigration and so on. In addition, continuous miniaturization of device dimensions demands thinner Cu diffusion barrier layer and seed layers to keep enough open-space at the top of trenches and vias to fill them with an electroplated Cu film to minimize resistivity. However, as the dimensions decrease, a thinner Cu seed layer tends to be agglomerated and have discontinuous surface, resulting in the formation of voids inside trenches and vias. Therefore, it becomes another challenging issue to fill trenches and vias completely with a thin Cu seed layer.

Recently, new barrier materials, which have better wettability with Cu compared to that of a conventional Ta-based barrier, have been studied to obtain continuous and smooth

morphology even with a very thin Cu film for the improvement of the filling property of electroplated Cu [1-4]. Among such materials, Ruthenium (Ru) has superior wettability with Cu, however, barrier property of pure Ru against Cu diffusion is not so good [3-4]. A 20 nm Ru film can be an effective barrier up to 450 C, but a 5 nm Ru fails at only 300°C [5]. The pure Ru film is not a perfect diffusion barrier because of its distinct crystallinity as deposited. Recently, an alloy of Ru & Ta has attracted much interest in performing as a good diffusion barrier for Cu. Literature support that 15 nm of Ru-Ta alloy can prevent Cu diffusion until after annealing at 700 C and therefore acting as an effective liner material [6]. According to international technology roadmap of semiconductors, it has been projected that the thickness of diffusion barrier layer has to be reduced and should be directly plateable with Cu. So far in the literature, only sputtering of Cu has been done to study the barrier properties of Ru-Ta alloys. In this chapter, electrodeposition of Cu on various compositions of Ru-Ta alloys using sulfuric acid and other baths has been reported.

3.2 Experiment

Different compositions of Ru and Ta were co-sputtered on Si wafer and the sputtering process information and other surface characterizations can be found in chapter 2. The wafers were cut into small pieces of 2 cm x 1cm to make electrodes. The area of the electrodes exposed to the solution is 0.173 cm^2 unless otherwise mentioned. Scotch tape is used to mask other area and the backside of electrodes that are not desired to be exposed into the solution. Cyclic voltammetry and other electrochemical data were obtained using CHI Potentiostat. All the potentials mentioned are with respect to Ag/AgCl standard reference electrode. The details of XRD technique that was used to obtain the crystalline properties is explained in chapter 2.

3.3 Results and Discussion

3.3.1 Cyclic Voltammetry of Ru and Ta in Cu Plating Solution

Ru and Ta shot electrodes were first polished and used to run cyclic voltammetry to see the Cu electrodeposition characteristics. Figure 3.1 shows the CV of fresh polished Ru and repeated CV scans of fresh polished Ta in 2mM $CuSO_4$ / 0.5M H_2SO_4 solution. Ru is a good substrate for Cu electrodeposition and shows better deposition characteristics. This is attributed to the presence of Cu under-potential deposition (UPD) peak at ~0.1 V vs. Ag/AgCl and the UPD stripping peak is present at ~0.17 V. Underpotential deposition is a phenomenon of electrodeposition of a species (typically reduction of a metal cation to a solid metal) at a potential less negative than the equilibrium (Nernst) potential required for the reduction of this metal.

The occurrence of underpotential deposition is often interpreted as a result of a strong interaction between the electrodepositing metal Cu (M) with the substrate Ru (S). The M-S interaction needs to be energetically favored to the M-M interaction in the crystal lattice of the pure metal M. This mechanism is deduced from the observation that UPD typically occurs only up to a monolayer of M (sometimes up to two monolayers). The electrodeposition of a metal on a substrate of the same metal occurs at an equilibrium potential, thus defining the reference point for the underpotential deposition. Underpotential deposition is much sharper on mono-crystals than on polycrystalline materials [7].

On the other hand, there is no Cu under-potential deposition peak in the CV of Ta in Cu plating solution. And the overpotential deposition peak was observed for a larger cathodic potential which explains that the energy requirement for Cu plating on Ta is higher compared to that on Ru. Also, Ta has high affinity towards reacting with oxygen which results in the

formation of thin layer of oxide on surface upon exposure to air. This oxide layer on Ta surface

is observed to be affecting Cu deposition.
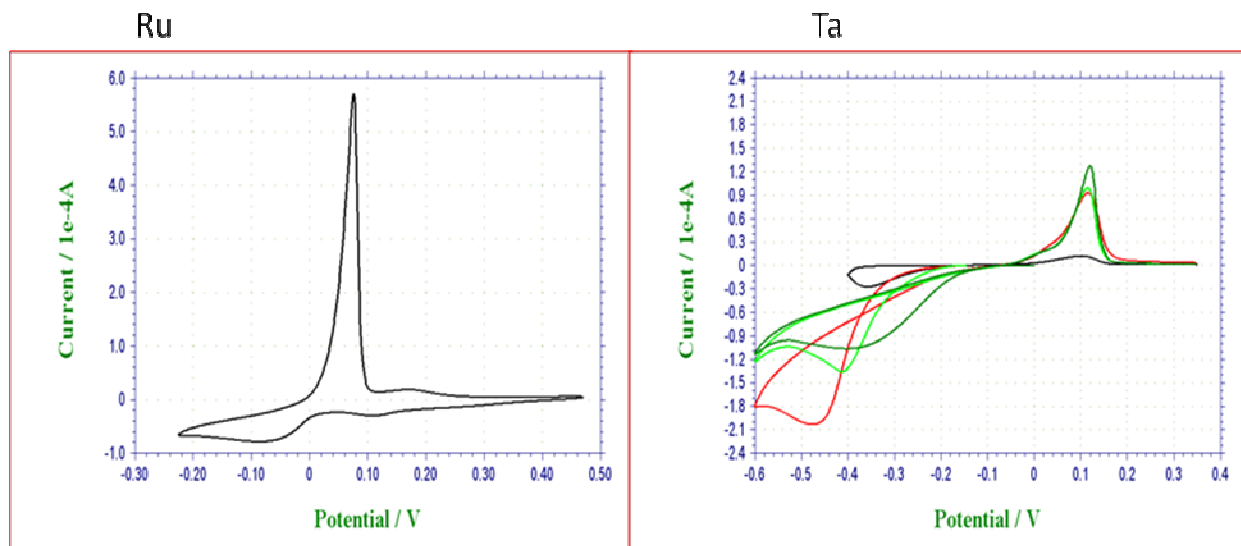
Figure 3.1 Cyclic voltammetry of Ru and Ta in 2mM $CuSO_4$ / 0.5M H_2SO_4 solution without any
surface treatments

3.3.2 Cyclic Voltammetry of Ru-Ta Alloys in Cu Plating Solution

3.3.2.1 As-Deposited Ru-Ta in Cu Plating Solution

The as-deposited Ru-Ta samples were tested for Cu plateability using cyclic voltammetry

technique. Figure 3.2 shows that the sample RT-7/3 which has higher Ru showed comparatively

better Cu diffusion limited reduction and stripping peak.
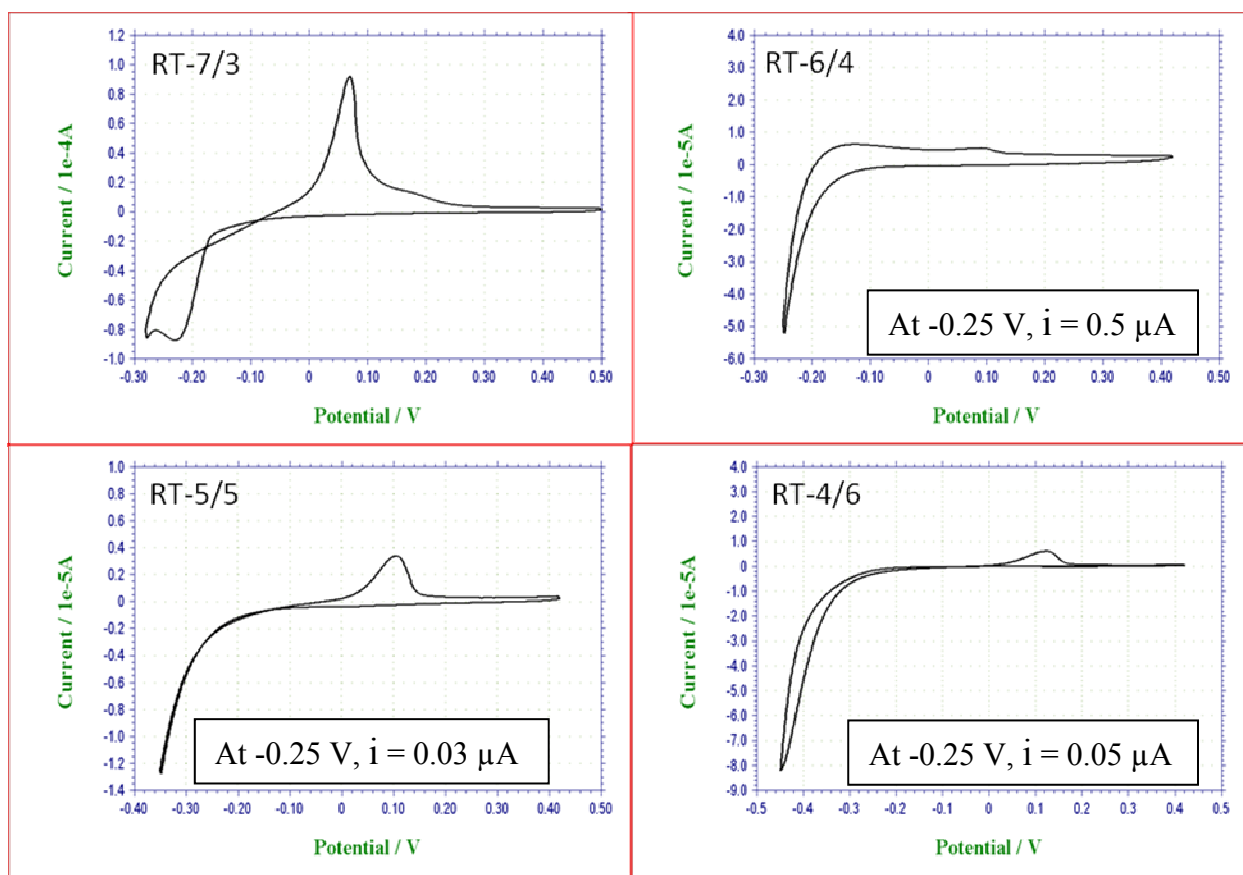
Figure 3.2 CV characteristics of RT-7/3, RT-6/4, RT-5/5, RT-4/6 samples in 2mM CuSO$_4$ / 0.5M H$_2$SO$_4$ solution without any surface treatments

Rest of the other samples had poor Cu deposition characteristics i.e. they did not yield well defined Cu reduction / stripping peaks as the amount of Ta increases above 40%. Among the four different composition samples, RT-6/4 which has higher sheet resistance inhibited Cu reduction but due to higher Ru than RT-5/5 and RT-4/6, it enhanced H$_2$ evolution. When the amount of Ta is higher than 50%, Cu does electro-nucleate on the surface which was confirmed by the presence of stripping peak. Since the presence of thicker Ta oxide inhibits smooth Cu nucleation, and it requires a method to either reduce or remove the oxide.

3.3.2.2. Effect of Forming Gas (FG) Treatment on Cu Deposition on Ru-Ta

Forming gas is a mixture of 5% H_2 and 95% Ar which was used to treat Ru-Ta surface.
The samples were kept inside an annealing tube chamber with a temperature of about 150° C. A
slow flow rate of forming gas was maintained inside the annealing tube. The samples were
treated for about 15 min in FG environment at set temperature and allowed to cool to room
temperature without taking them out to air. After the samples were cooled, they were transferred
to Cu plating solution one by one to run the cyclic voltammetry. Figure 3.3 shows the cyclic
voltammetry results of forming gas treated RT samples.

Figure 3.3 CV characteristics of RT-7/3, RT-6/4, RT-5/5, RT-4/6 samples in 2mM CuSO4 /
0.5M H_2SO_4 solution after FG treatment. Ec: Crossover potential where two current intercept
together in the reversal sweep

It was clearly evident that the FG treatment reduces the surface oxide which can be seen from the disappearance of capacitance current in the CV of sample RT-7/3. Due to the higher Ru content and oxide reduction from FG treatment, the Cu deposition is enhanced on RT-7/3. This can be seen from the development of Cu diffusion limited reduction into fine peak compared to untreated sample. Also the onset of reduction potential has shifted earlier from -0.18 V on untreated RT-7/3 to -0.1 V in FG treated. The stripping peak has become sharper which indicates the electrode processes are faster and efficient. On the other samples that have higher amount of Ta, 40% and above, the FG treatment only slightly improves the Cu nucleation compared to untreated samples due to the limited extent of oxide reduction by FG. On RT-6/4 and RT-5/5, upon the reverse potential sweep in crossover potential (Ec), the two current crossovers appear indicating the formation of stable growth centers at the substrate surface.   For a longer time of treatment, it will result in increased sheet resistance which is also an undesired process for Cu electrodeposition.

3.3.2.3. Effect of Hydrogen Plasma Treatment

Plasma is a partially ionized gas consisting of equal number negative and positive charges and a different number of unionized neutral molecules. Hydrogen gas plasma is usually used to reduce the metal oxides to metal. Direct current plasma sources are not commonly used in processing applications because DC power cannot be coupled through insulating substrates, the pressure required is relatively high, the discharge is not efficient and the cathode voltage is not controllable. Radio frequency (rf) or microwave powers are generally used to produce and sustain the plasma in plasma processing tools. Many types of RF plasma sources are available for plasma processing and they normally classified into capacitive, inductive, and wave sources [8,9]. Although most experiments of hydrogen reduction of metal oxides were carried out in

thermal plasmas, non-equilibrium plasma has major advantage. Non-equilibrium plasma has high energy efficiency for generation of excited hydrogen molecules, atomic hydrogen and other active species stimulating the reduction process at low temperatures of gas and solid oxides. Atomic hydrogen generated in the plasma reaches the surface of metal oxide and it stimulates the reduction process according the following equation:

$$M_mO_n + 2n\ H \ -----> \ mM + n\ H_2O$$
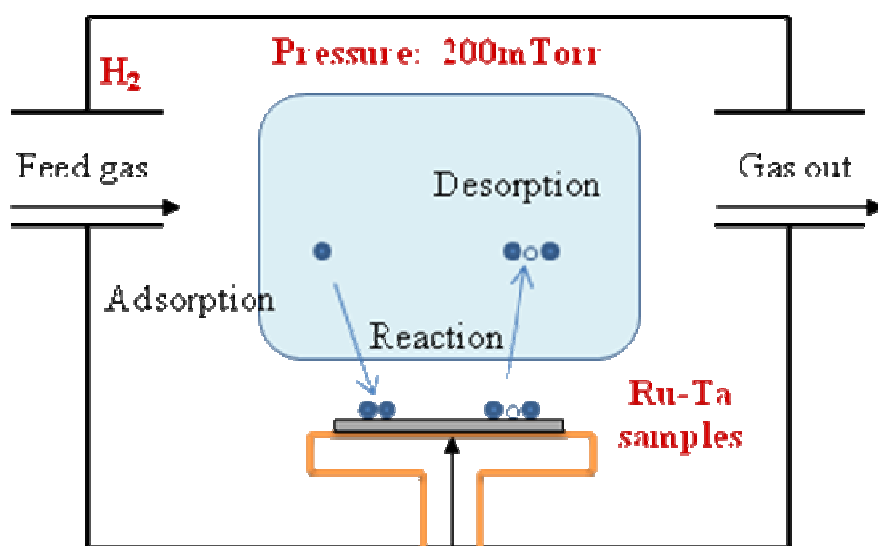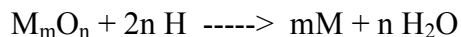
Figure 3.4 Schematic view of the plasma treatment on Ru-Ta samples

The reduction process is stimulated by vibrationally excited H_2 molecules through their surface dissociation and diffusion of H atoms into the crystal structure. Metal reduction starts from the surface and the front of metal formation propagates from the surface into the solid body. Figure 3.4 shows the schematic of plasma processing.

Figure 3.5 shows the cyclic voltammetry results of hydrogen plasma treated RT samples. As expected RT-7/3 sample shows good Cu diffusion limited reduction peak and a sharp

stripping peak compared to untreated sample indicating the oxide reduction and efficient electrode kinetic processes. RT-6/4 and RT-5/5 did not have any crossover potential as in the case of forming gas treated samples indicating that the FG treatment was better than hydrogen plasma in Ru-Ta surface oxide reduction process.
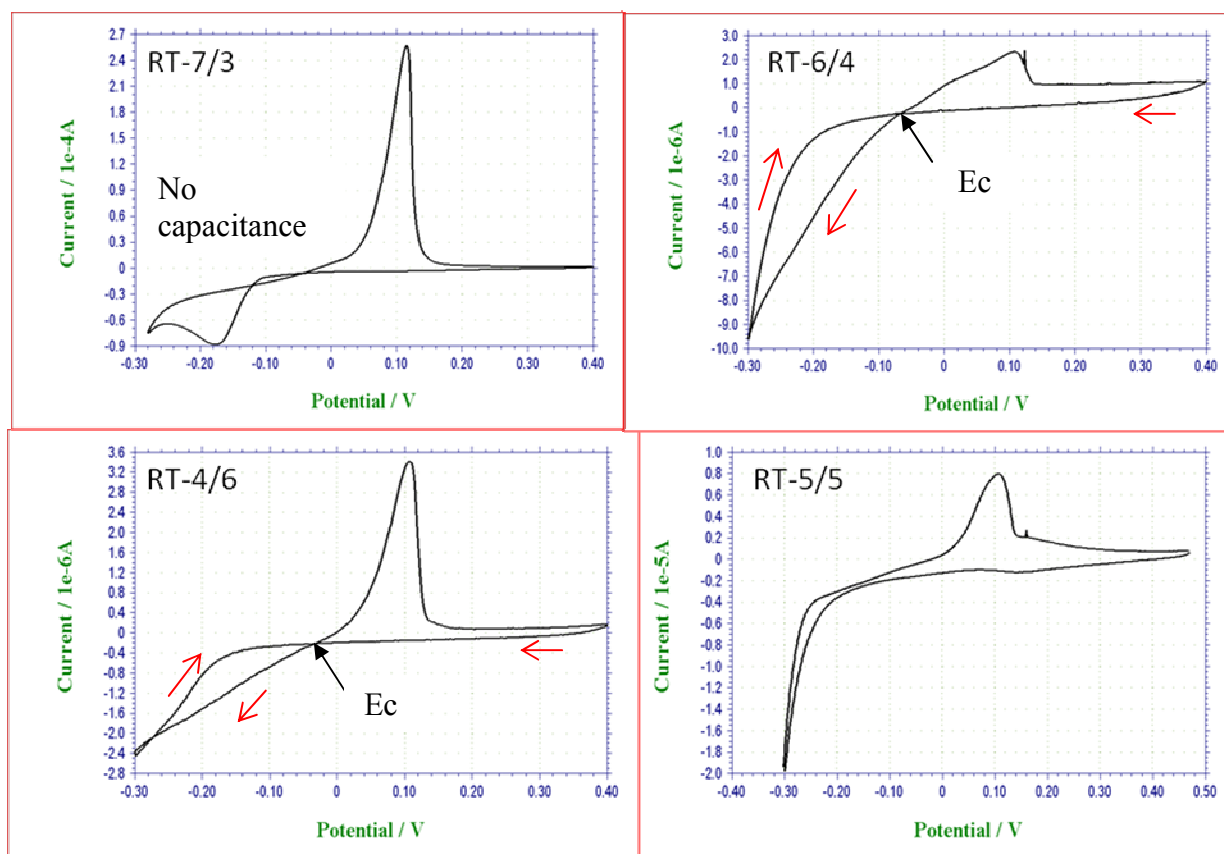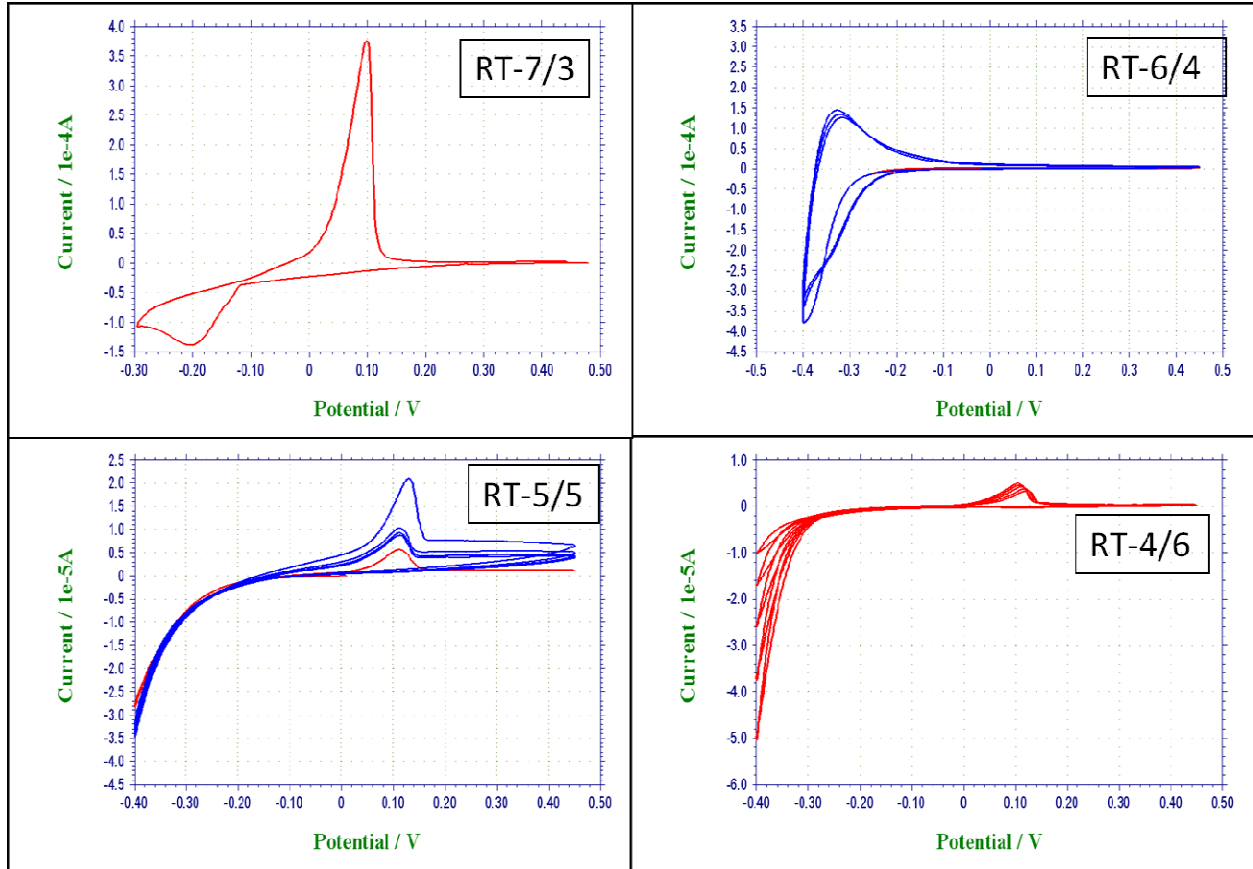

Figure 3.5 CV characteristics of RT-7/3, RT-6/4, RT-5/5, RT-4/6 samples in 2mM $CuSO_4$ / 0.5M H_2SO_4 solution after hydrogen plasma treatment

3.3.2.4. Effect of Caustic NaOH Treatment

Since the presence of Ta oxide is found to inhibit the Cu nucleation on the RT surface, there comes a need to either reduce or remove the oxide from the substrate. Ta is known to form a combination of the following stoichiometric oxides such as TaO, Ta_2O_5, TaO_2 but the thermodynamically stable oxide is its pentaoxide. It has been studied that the Ta_2O_5 is highly resistant and robust material which if polarized anodically grows more in thickness [10]. Also,

64

in acid solution Ta oxide cannot be electrochemically reduced in the cathodic potential region because of its high inertness. But it can be broken down or attacked even at room temperature by concentrated alkaline solutions. So, conc. NaOH solution was used to treat the Ru-Ta samples in order to remove the oxide from the surface.
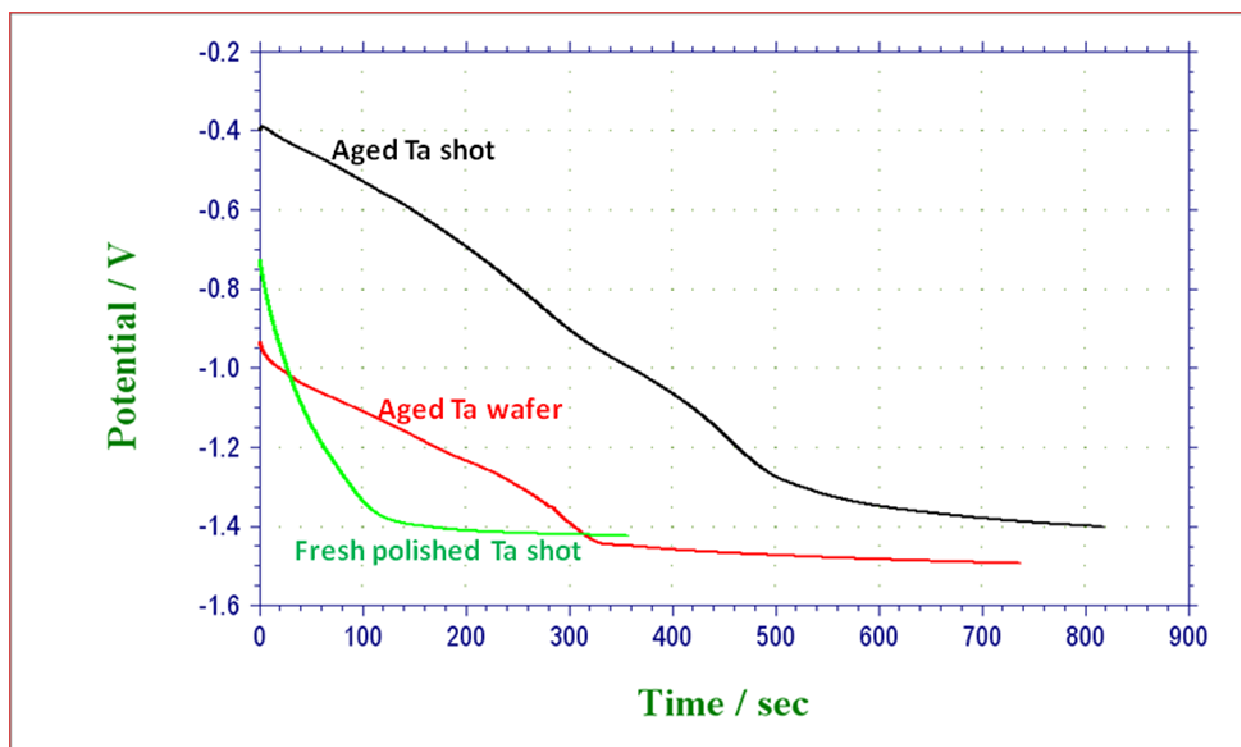
Figure 3.6 Open circuit potential measurements of Ta samples having different oxide thickness in 50% NaOH solution

In order to evaluate the oxide removal from the surface, at first Ta electrodes with different oxide thickness were chosen to be treated in caustic solution. Open circuit potential (OCP) measurement is a technique from which the electrode surface potential is measured against a standard reference electrode potential (in this case Ag/AgCl). From this, the nature of a metal surface in terms of its oxide formation or dissolution can be evinced. For this purpose, electrodes were made from aged Ta, fresh polished Ta and aged Ta wafer which were composed of oxides that are different in thickness. The area of electrode exposed into the solution was

65

same for all the electrodes. The OCP measurement was started as soon as the electrode is dipped in the 50% NaOH solution. Figure 3.6 shows the OCP trend for all the three electrodes. The OCPs shifting in the negative direction for all the electrodes indicates the continuous dissolution of air formed Ta oxide from the surface into to the solution. As the native oxide is dissolved, the surface is continuously refreshed and becomes more active over time causing the OCP to shift negative. The time it takes to reach a stabilized potential is called the induction time. The induction time is longer (~ 10 min) for aged Ta shot electrode for the obvious reason that it is composed of much thicker oxide and hence the OCP starts from more anodic region at -0.34 V. Fresh polished Ta electrode has much thinner oxide having more cathodic OCP onset at -0.72 V. It takes around 2 min to dissolve the surface oxide from fresh polished Ta and for aged Ta wafer it takes approx. 5 min. Further treatment results in dissolution precipitation according the following reaction equations.

Air-formed oxide dissolution:
$$3Ta_2O_5 + 8NaOH \longrightarrow Na_8Ta_6O_{19} + 4H_2O$$

Dissolution Precipitation:

$$6Ta + 8NaOH + 30OH^- \longrightarrow Na_8Ta_6O_{19} + 19H_2O + 30e^-$$
$$30H_2O + 30e^- \longrightarrow 15H_2 + 30OH^-$$
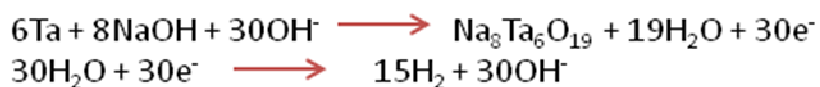
Treating air exposed Ta in conc. NaOH solution dissolves the native oxide as described in previous paragraph. The Cu electrodeposition CV on bulk oxide removed Ta surface is shown in Figure 3.7. It was observed in the first CV scan, the huge cathodic reduction charge indicating a large amount of Cu reduction has happened and no anodic charge relating to Cu stripping.
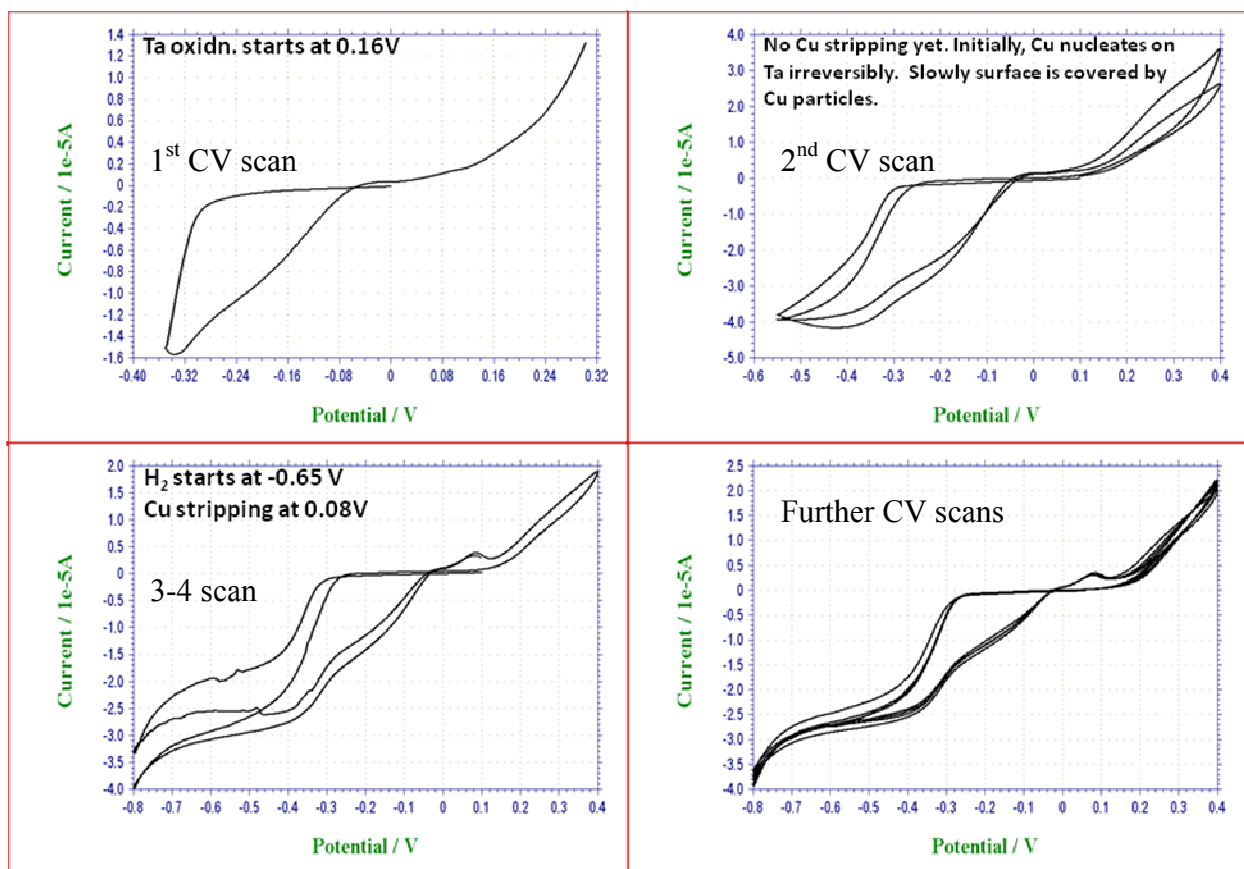
Figure 3.7 Cyclic voltammetry of Ta after NaOH treatment in 2mM $CuSO_4$/0.5M H_2SO_4 solution

But scanning the potential to further positive region oxidizes the Ta surface and the oxidation of the same starts at 0.16 V vs. Ag/AgCl reference. Cu anodic stripping peak was still not observed in the second CV scan but having more or less the same amount of Cu reduction charge. The Cu stripping peak was observed only in third CV scan slightly and this indicates that the Cu deposited on Ta surface during first 2 CV scans is an irreversible electrochemical process i.e. only the Cu electrodeposition happens and not the oxidation. The anodic peak observed in the 3rd CV scan arises from Cu stripping from previously deposited Cu layers on Ta surface. Further increasing the number of potential cycle results in stabilized amount of Cu cathodic reduction and anodic stripping charge. This kind of behavior of Ta electrode i.e. irreversible metal layer formation constitutes an effect called diode effect or Schottky behavior

[11]. This explains that there is a presence of thin TaO_x layer on Ta surface which acts as n-type region and is an electron donor.
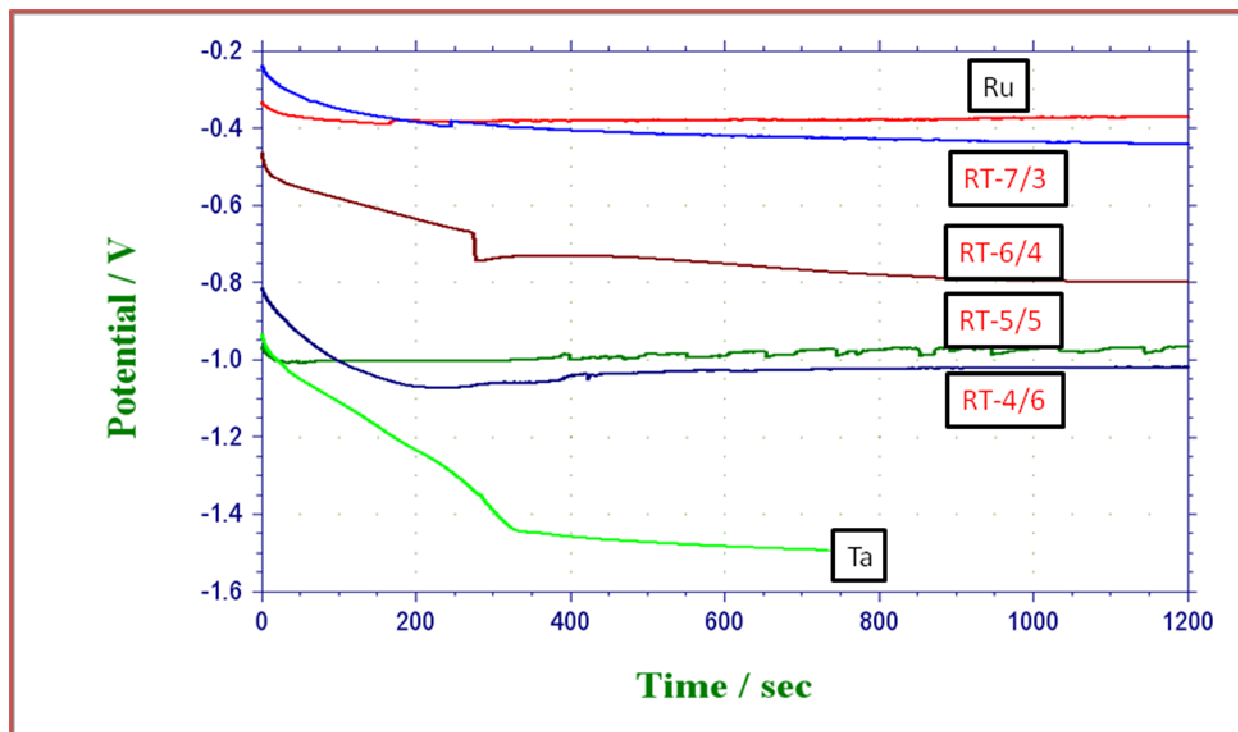
Figure 3.8 Open circuit potential measurements of Ru-Ta samples in 50% NaOH solution

Similarly, Ru-Ta samples were also treated in 50% NaOH solution to remove the native oxide from the surface. Figure 3.8 shows the evolution of open circuit potential from Ru, Ta and Ru-Ta samples in NaOH solution. Ta has far negative potential as it is more active and Ru has far positive potential and it is because Ru is nobler than Ta. The induction time for Ta is higher (~ 10 min) than Ru (~2 min) because of higher affinity of Ta towards oxide formation compared to Ru. The bond strengths of Ru and Ta with oxygen are 43 and 198 kcal/mol respectively and this explains the result of thicker oxide formation on Ta than Ru. The OCP value for Ta in 50% NaOH is in the range of -1.5 V to -1.0 V vs. Ag/AgCl and thus the cathodic reaction taking place in that range would be the following:

68

$$2H_2O + 2e^- \longrightarrow H_2 + 2OH^- \qquad E = -1.10 \text{ V}$$
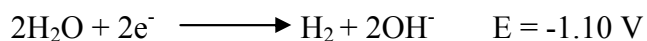
The observed evolution of gaseous products for longer time of immersion on Ta samples in 50% NaOH solution at room temperature corroborates this reaction. As the amount of Ta present on RT samples increase, the onset OCP values shift in negative direction indicating the surface nature shifts towards Ta surface. This result also serves as an evidence for the RT sample composition. The induction time for RT samples is not as long as in pure Ta because of the effect from the presence of Ru. Ruthenium dissolves in caustic solution as per the following reaction equation.

$$RuO_2 + 4OH^- \longrightarrow RuO_4^{2-} + 2H_2O + 2e^-$$
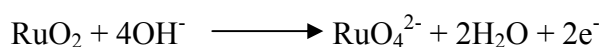
Both the Ru oxide and Ta oxide dissolution supposed to be happening in the solution but because the Ta has higher affinity towards oxidation, the rate of oxide formation on the very surface will be faster and dominated by Ta particles. This makes it reasonable to assume that most of the surface is with Ta oxide. It is also assumed that the OCP is affected only slightly from Ru oxide dissolution. Presence of two dissimilar metals on a surface and exposing it to a corrosive medium constitutes a galvanic couple. Here in this case, Ta behaves as anodic component because of its easier oxidative property and Ru behaves as cathodic component being protected from oxidation by Ta.
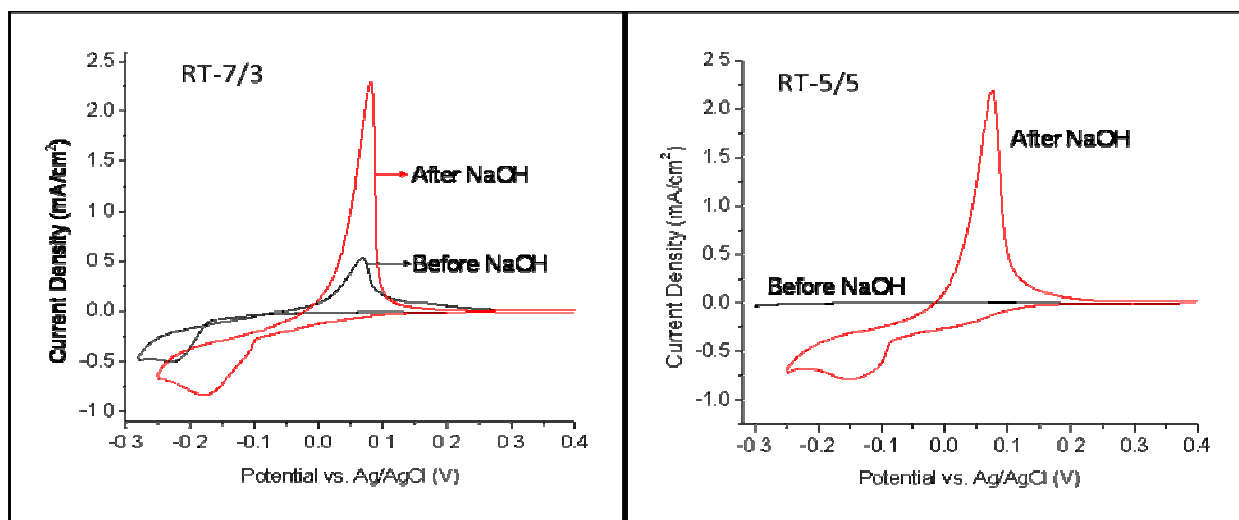
Figure 3.9 Cyclic voltammetry of RT samples before and after NaOH treatment in 2mM CuSO$_4$/0.5M H$_2$SO$_4$ solution

The effect of NaOH treatment on the improvement of Cu electrodeposition process is studied. As shown in Figure 3.9 the cyclic voltammetry results (shown here are only RT-7/3 and RT-5/5) for all the RT samples in Cu plating solution show better Cu diffusion limited reduction peak after the caustic solution treatment. The improvement of Cu reduction process on RT-5/5 is tremendous as observed from the enormous increase in Cu reduction charge compared to that observed before treatment. The stripping peaks have become sharper which indicate that the kinetics of electrode processes has improved. In case of RT-7/3 sample, compared to CV before treatment, the Cu onset reduction potential has shifted ~ 100 mV earlier after caustic solution treatment. All these observations provide evidences clearly that the Cu^{2+} ion reduction has improved after NaOH treatment of RT alloy samples.

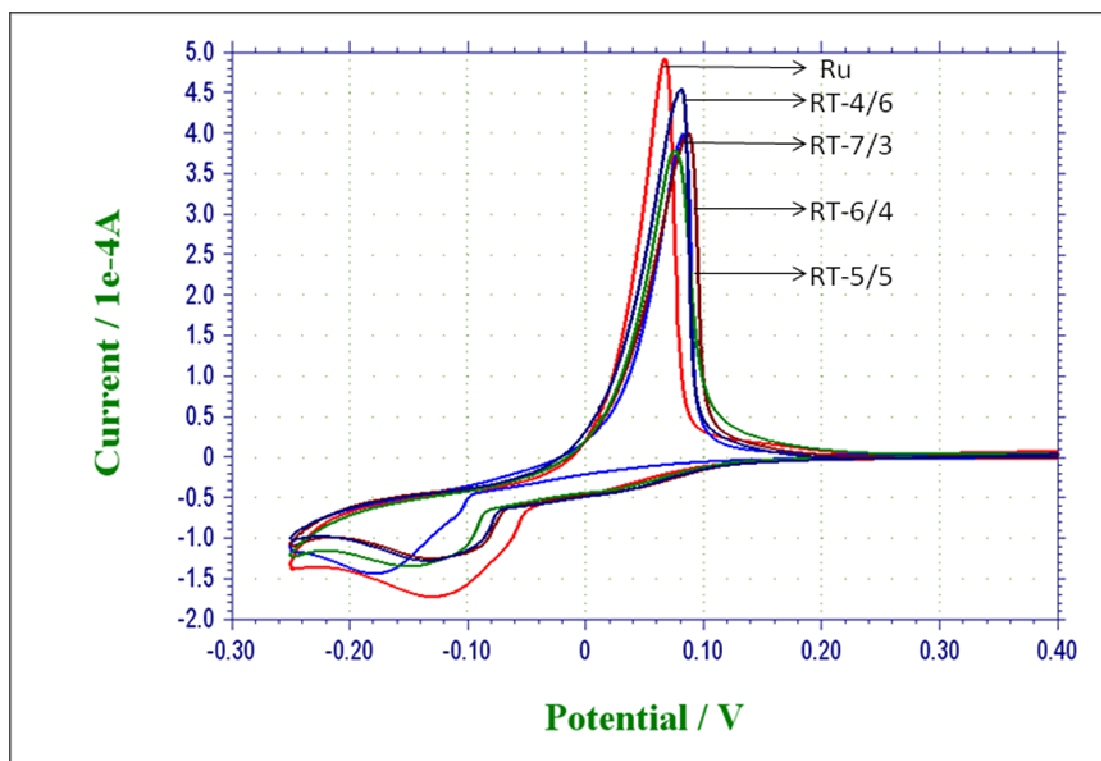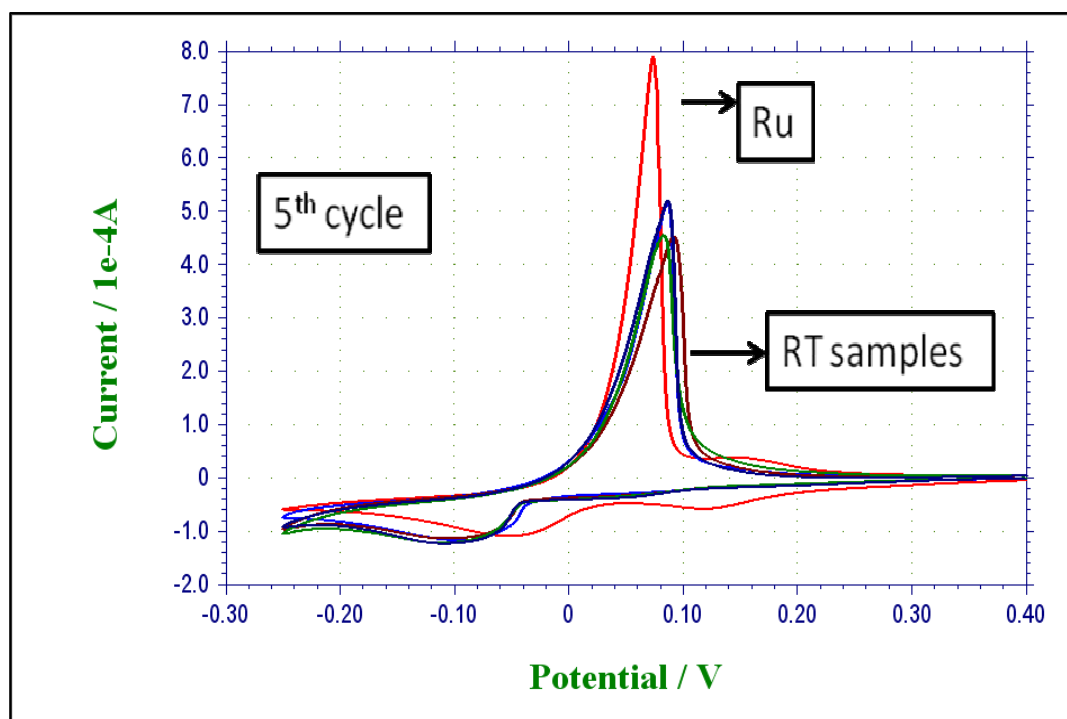Figure 3.10 First CV scan overlays of Ru & RT samples after NaOH treatment in 2mM CuSO$_4$/0.5M H$_2$SO$_4$ solution

Figure 3.11 CV 5th cycle overlay of Ru & RT samples after NaOH treatment in 2mM CuSO$_4$/0.5M H$_2$SO$_4$ solution

The first CV scan of NaOH treated RT samples in Cu plating solution (Figure 3.10) showed a little variation in the onset Cu reduction potential and started at -0.1 V but for Ru, the onset reduction was earlier i.e. at -0.05 V. Though the onset reduction potentials are different for different RT samples in first CV scan, they were stabilized at 5th CV scan, shown in Figure 3.11. The onset of Cu reduction started at -0.05 V. This indicates the transformation of surface into more favorable condition. The difference between Ru and RT samples with reference to Cu plating is that, Ru after NaOH treatment still possessed Cu under-potential deposition phenomenon but it was not observed in RT samples. Other than UPD, the CV scans of RT samples resemble the pure Ru metal; this resemblance and the absence of UPD suggest that after NaOH treatment all the surface Ta oxides have been removed and the surface is mostly left with Ru grains but not 100%.

3.3.2.5. Cu Adhesion Test by Scotch Tape Method

Interconnect reliability is a major issue concerning the microprocessor industry; and electromigration failure has been linked to interconnect interface defects, which suggests that poor adhesion between the copper and diffusion barrier should be of significant concern [12,13]. Thus, it is necessary that adhesion be considered in the initial stages of a seedless direct Cu electrodeposition. Potential controlled experiments have been carried out to electrodeposit a thin film of Cu on NaOH treated RT samples. For all the RT samples, the potential was held at -0.08 V which was the Cu^{2+} peak reduction potential, for 1 min in 50 mM $CuSO_4$/0.5M H_2SO_4 Cu bulk plating solution. Shown in the Figure 3.12 are the Cu film on RT-6/4 and RT-5/5 after making ASTM Standard Tape Test Method (REF: "Cross-cut tape test by ASTM D3359-95," Annual Book of ASTM Standards, Vol. 06.01). The steps involved in the tape test are: making a scratch on Cu film by using a diamond scriber, sticking a piece of scotch tape strongly and removing it.

If the Cu film remains on the substrate without sticking to the tape, then it is considered the adhesion is good. It was observed the Cu film adhesion was better on NaOH treated RT sample surfaces as proved by Scotch tape method.
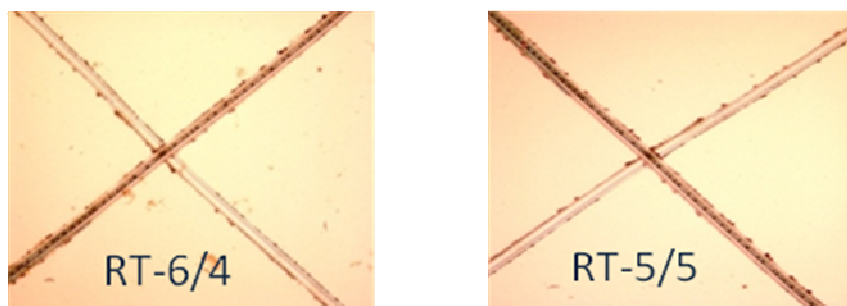
Figure 3.12 Adhesion of Cu film on NaOH treated RT samples by Scotch tape peel method

Table 3.1 shows the observations on Cu film formation and adhesion properties on differently treated RT sample surfaces. It shows the Cu film can be made by controlled potential electrodeposition on all NaOH treated surfaces and the adhesion is also good. But for forming gas treated samples, for the increased Ta content samples it was hard to deposit the film.

Surface Treatments	RT-7/3	RT-6/4	RT-5/5	RT-4/6
NaOH treated	Film formed but bad adhesion	Film formed, good adhesion	Film formed, good adhesion	Film formed but adhesion of Ru-Ta was bad.
FG treated	Film formed but peeled off very bad	Cu film was not formed	Cu film was not formed	Cu film was not formed
Untreated	Film formed at more −ve potential but peeled off	No film formed	No film formed	No film formed

Table 3.1 Cu film formation and adhesion properties on differently treated RT surfaces

3.3.2.6 X-Ray Diffraction Characteristics of RT-7/3

Treating the RT samples in NaOH solution improves the Cu nucleation process but it is important to know if NaOH actually removes only Ta oxide or also Ta particles from the film structure. X-ray diffraction pattern was obtained for RT-7/3 sample before and after NaOH treatment (see Figure 3.13).   It was observed that the atomic plane reflections of the phases resemble those that are before NaOH etching. A slight decrease in one of the peaks intensity has been observed after NaOH etching indicating the removal of that particular phase crystallites from the thin film. Since there are not much changes present in the diffraction pattern before and after NaOH etching, it can be concluded that the etching process just removes most of the oxides from the surface without changing its crystalline structure. In other words, the bulk of the film still retains the Ru-Ta alloy structure which is what is desired for improved Cu diffusion impediment.

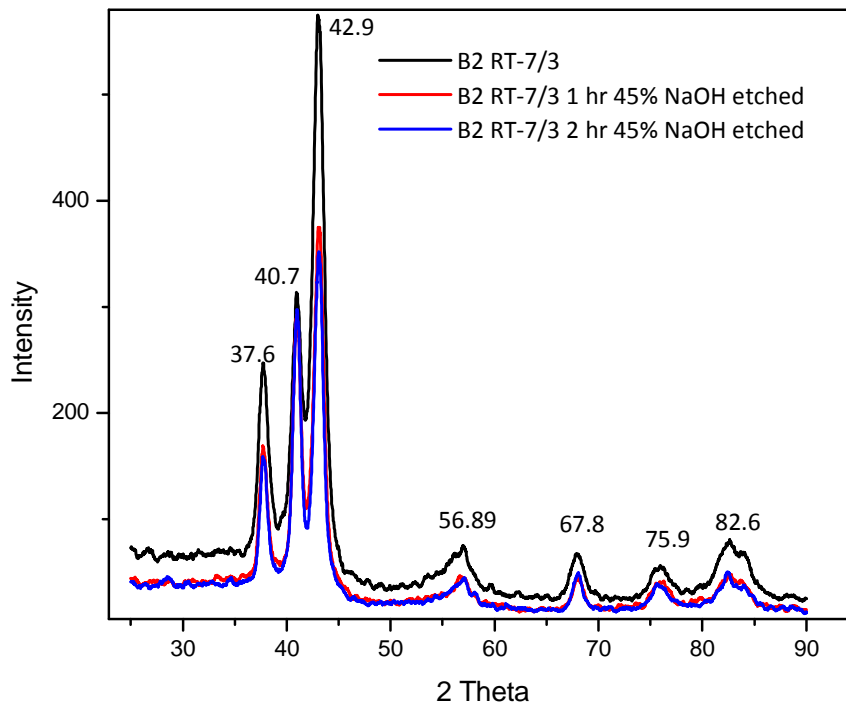Figure 3.13 XRD Pattern of RT-7/3 before and after NaOH treatment
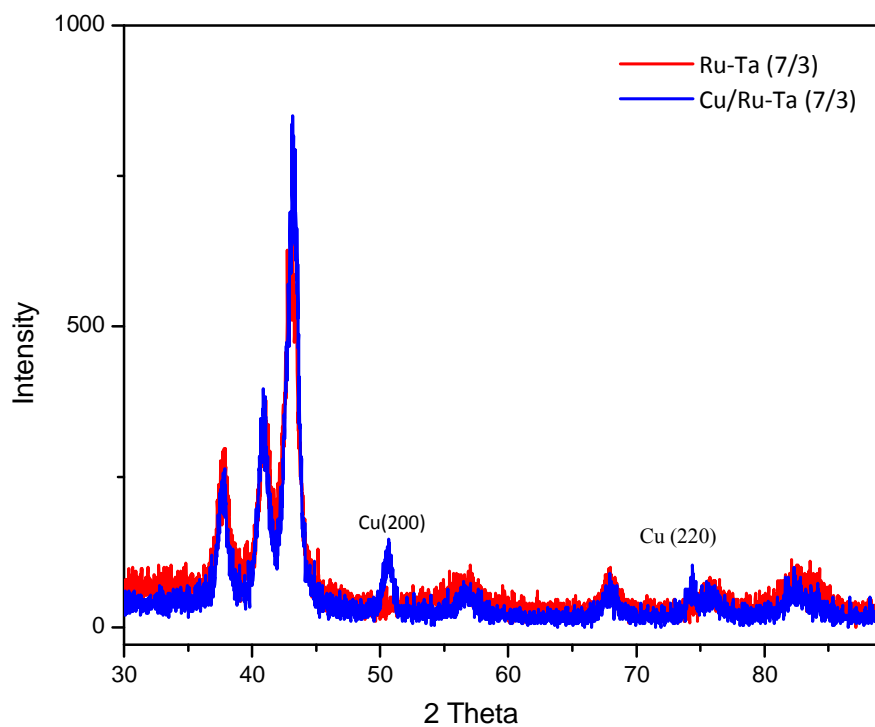
Figure 3.14 XRD Pattern of Cu deposited RT-7/3

Cu was electrodeposited on NaOH etched RT-7/3 by holding the potential at peak reduction region. Fig. 3.14 shows the presence of Cu (200) and Cu (220) peak on RT-7/3.
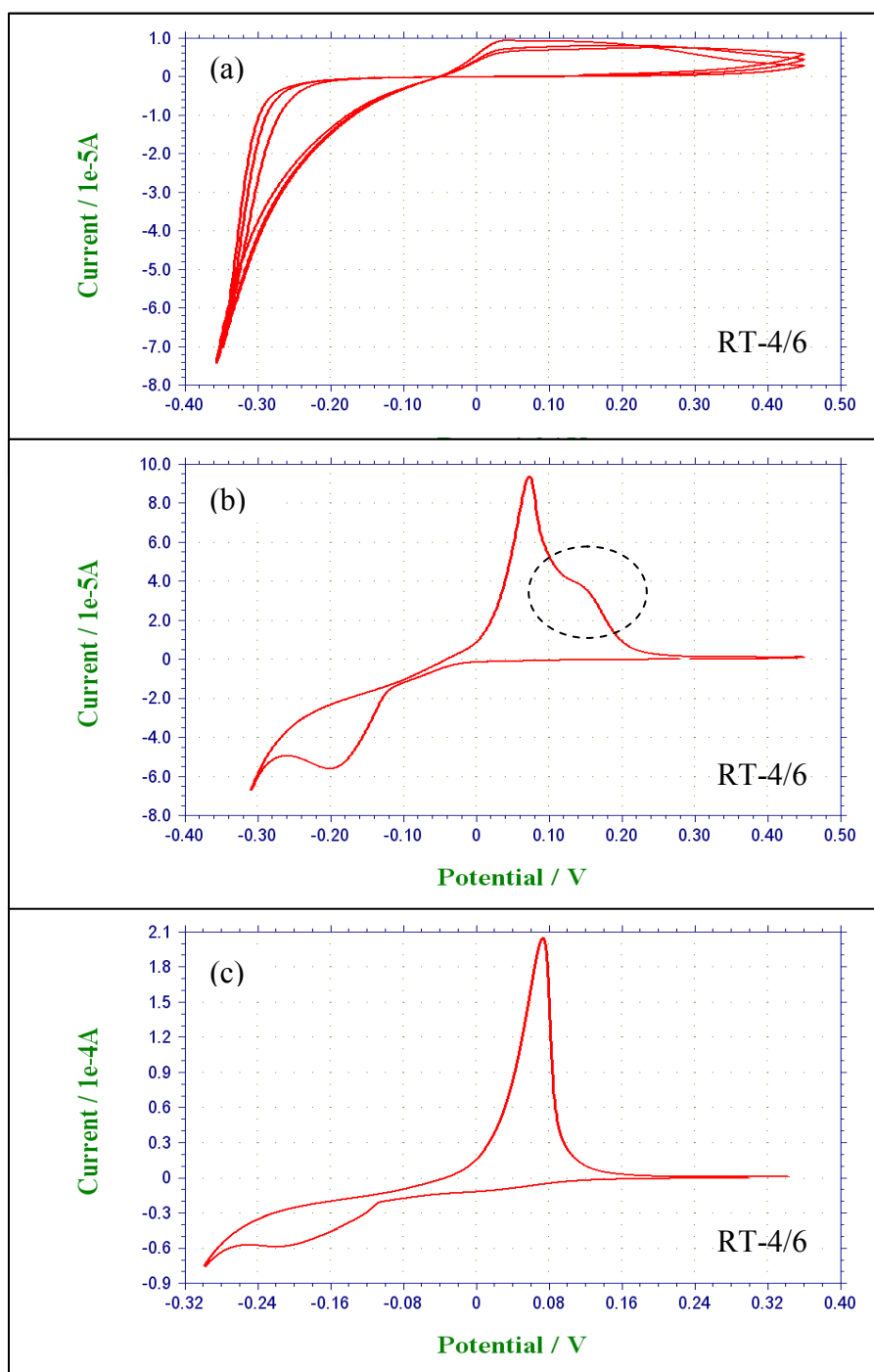
Fig. 3.15 Time dependent NaOH etching and the effect on Cu electrodeposition on RT-4/6 (a) 3 min, (b) 6 min and (c) 10 min of etching

Optimization of parameters for any experiment will be necessary and so the sample RT-4/6 was first used to optimize the NaOH treatment time. Figure 3.15 shows the cyclic voltammetry results after treating RT-4/6 in NaOH solution for various times. For 3 min of etching, the surface was not activated and stays resistive for Cu electrochemical deposition. For 6 min of etching, we observe that the surface started to enhance Cu nucleation as it was evident by the appearance of Cu diffusion limited reduction peak. Interesting observation was the presence of a shoulder on the Cu anodic stripping peak. This shoulder peak may be attributed to Cu particles intercalated between defective sites of Ta-Ru oxides due to insufficient etching. Further etching for 10 min was found to be sufficient for observing better kinetics of Cu electrochemical deposition and stripping.

3.3.3 Surface Treatments and Electrolytes Effect

Since Ru-Ta alloy thin film has been a recent topic of study for the application of better Cu diffusion barrier, and all the other research groups have studied its barrier properties having Cu deposited by sputtering process, it was necessary to explore more surface treatments and to study the effect of the same. Hence this section will discuss about the effect of following treatments on Cu cyclic voltammetry:

1. Iodine pretreatment

2. Tetra-methyl ammonium hydroxide treatment

3. CV using Cu citric acid bath

4. CV using ammoniated citric acid bath

3.3.3.1 Iodide Pretreatment

Surface oxidation of Ta upon exposure to air and in solution is the main issue for the disability of Cu electroplating on it. Also as the semiconductor device dimensions decrease, the currently used diffusion barrier layers such as Ta or TaN would become too thin and as a result the resistance increases [14]. Ru is another alternative for diffusion barrier layer because of its high melting point (2310 C), higher conductivity (7.6 $\mu\Omega$cm) and better oxidation resistance than Ta at ambient conditions. For direct electroplating of Cu, prevention of surface oxide formation will be very helpful. Iodine adsorption on metal surface layer has been demonstrated to be a good method to prevent the surface from oxidation and to protect it from ambient contaminations [15-18]. Other than protecting the surface from oxidation, iodine adsorption on surface is also known to have an effect on Cu electrodeposition acting as a surfactant to enhance conformal Cu growth [19].

For that reason, a solution of 1mM KI in 0.5M H_2SO_4 is prepared for electrochemically treating the RT electrodes with iodine. The native oxide on Ru electrode is at first electrochemically reduced by cycling the potential in sulfuric acid. The electrode is then transferred into iodine containing solution and the potential is cycled between -0.3V and +0.3 V for 5 cycles. The electrode is then rinsed slightly, transferred in to Cu UPD solution and the obtained cyclic voltammetry results are shown in Figure 3.16 a. It was observed that the Cu overpotential deposition has turned out to be happening over a broad potential window region on iodine modified Ru. But in case of RT-7/3 with the same kind of surface oxide reduction and iodine pretreatments, the Cu reduction peak was observed to occur at an earlier potential of -0.18 V. Figure 3.16 c shows the overlay CV of RT-7/3 with and without iodine pretreatment. This time in I-solution, the potential was not cycled; it was held at constant value of -0.15 V for 60 s.

78

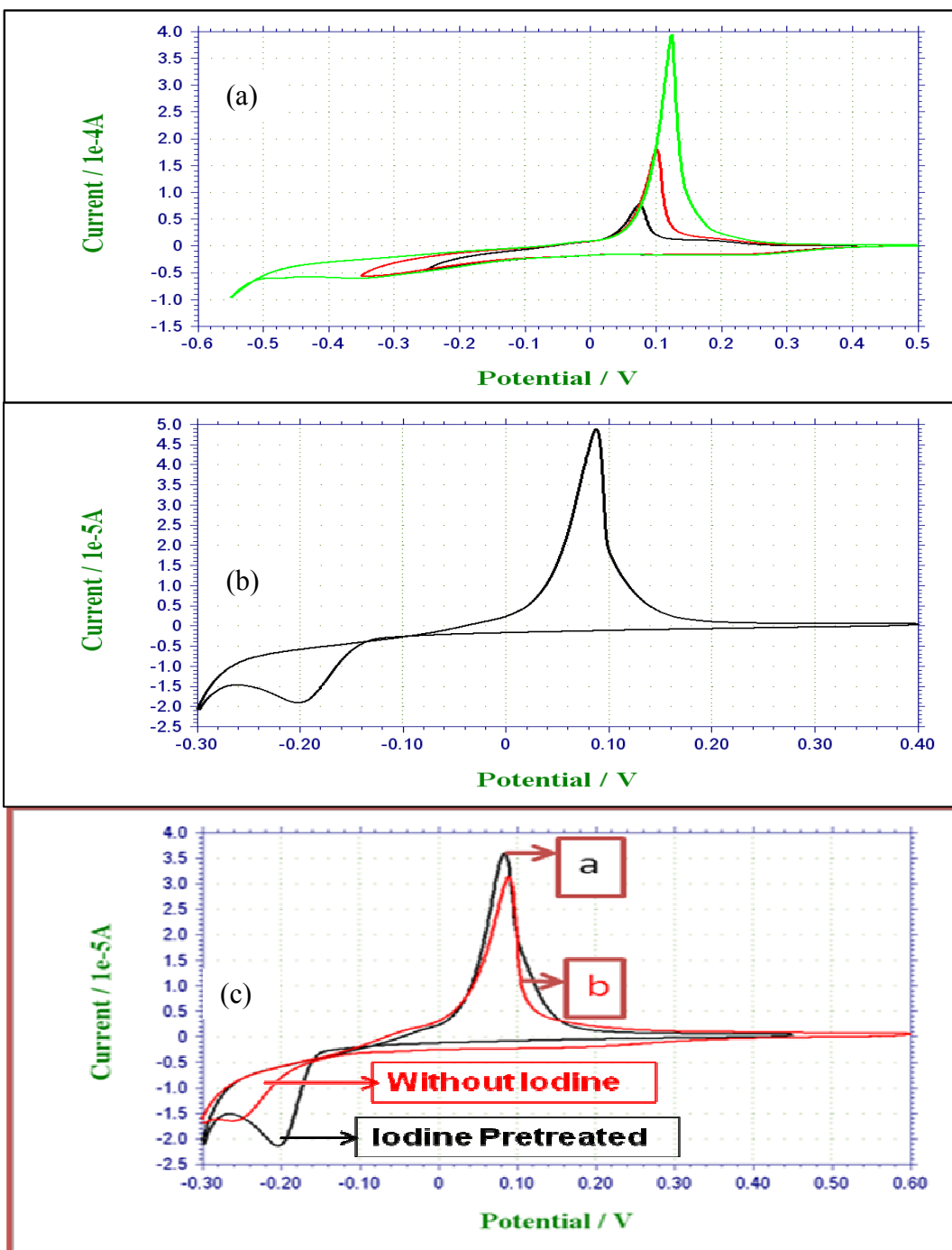Figure 3.16 CV of Ru (a), RT-7/3 (b) in Cu UPD solution after oxide reduction in sulfuric acid and iodine treatment by potential cycling in I-containing solution; Overlay of RT-7/3 CV (c) in UPD solution with and without iodine pretreatment.

When RT-7/3 was polarized at constant potential instead of cycling, the Cu reduction

peak has become sharp and the onset shifted a little earlier. This certainly proves that the iodine

layer on RT-7/3 prevents further oxidation upon exposure to air and Cu reduction becomes enhanced. More work can be done on exploring iodine adsorption using XPS.

3.3.3.2 Oxide Reduction in Tetra-methyl Ammonium Hydroxide (TMAH)

Studies on Cu nucleation and growth mode have been made to get insights on the conformal trench filling. It is found that the oxide surface on Ru or Ta barrier layers is one of the major problems in obtaining a smooth Cu deposition with better adhesion. Failure to remove the air-formed 3D oxide film results in Volmer-Weber (island) growth and consequently poor trench filling, as well as poor adhesion between Cu and Ru [20]. Electrochemical surface oxide reduction of Ru in sulfuric acid prior to Cu deposition yields highly coalesce Cu film. Similarly, tetra-methyl ammonium hydroxide was also used to reduce the surface oxide on Ru [21].
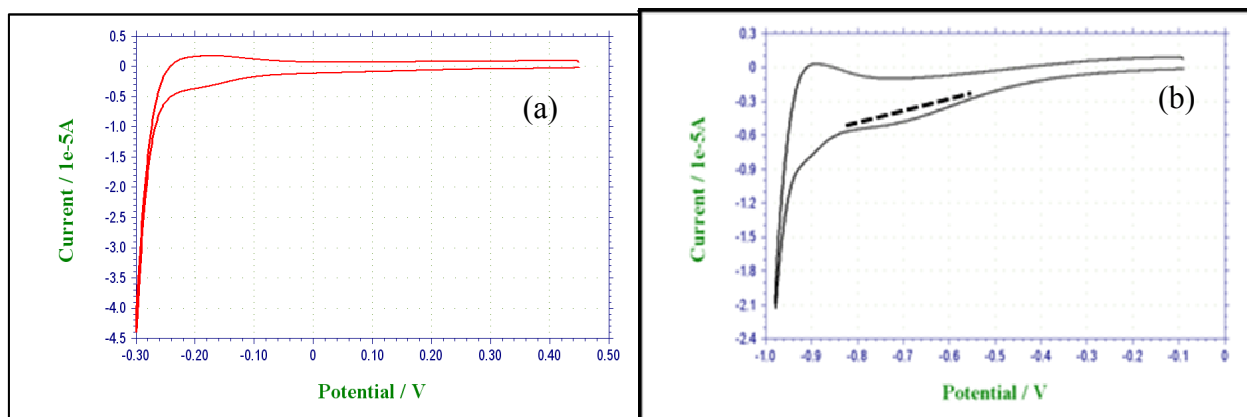
Figure 3.17 CV of RT-7/3 in (a) 0.5 M H_2SO_4 and (b) 0.05M TMAH, pH 13 solution

In Figure 3.17, CV shows the comparison of surface oxide reduction charge for RT-7/3 in sulfuric acid and TMAH solution.   It was observed that the oxide reduction charge in the first CV scan is higher in TMAH solution than sulfuric acid which suggests that TMAH alkaline solution is very effective in removing oxide from resistive substrates like RT alloy samples.
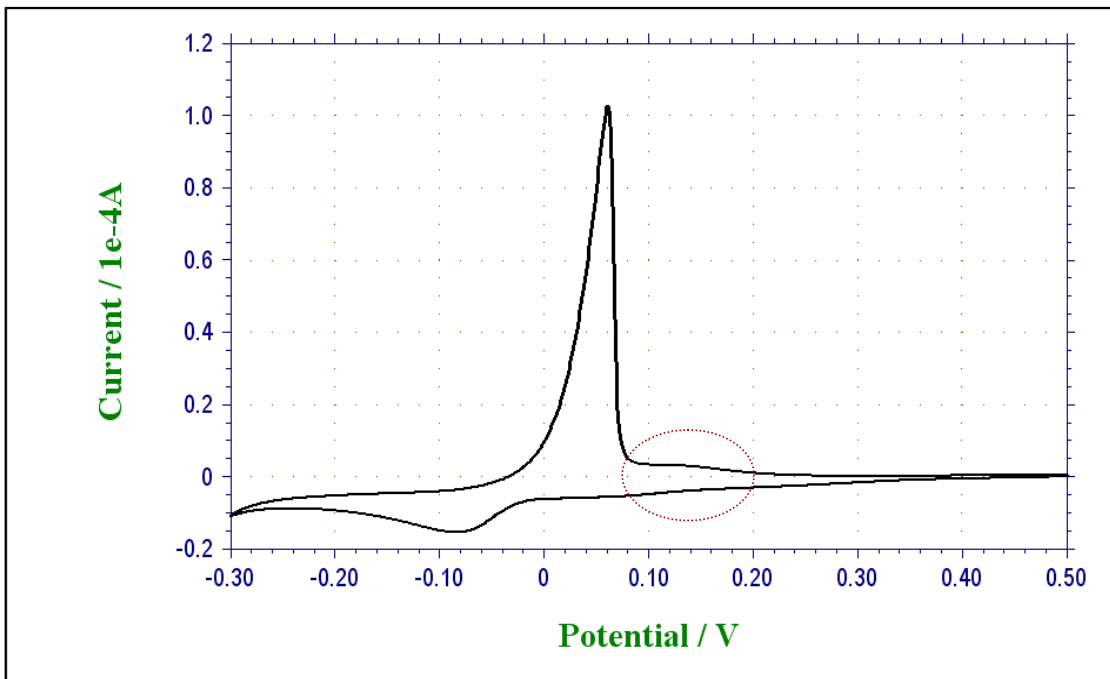
Figure 3.18 CV of RT-7/3 in 2mM $CuSO_4$/0.5 H_2SO_4 after reducing the oxide in 0.05 M tetra-methyl ammonium hydroxide, pH 13

After reducing the surface oxide by cycling the potential in 0.05M TMAH, pH 13 solution, CV characteristic was obtained for RT-7/3 in Cu plating solution. As shown in Figure 3.18, the wettability of Cu on RT-7/3 reduced in TMAH has improved and that was evident by the slight appearance of Cu UPD-like peak. This suggests that reducing native oxide on Ru-Ta by electrochemical method is an effective when done in TMAH solution and this also works better for resistive substrates.

3.3.3.3 Cu Electrodeposition on Ru-Ta using Complex Electrolytes

Cu electrodeposition on resistive surfaces such as Ta, TaN, TiN etc. have been studied and observed to be occurring smoothly using Cu-Complex bath [22].
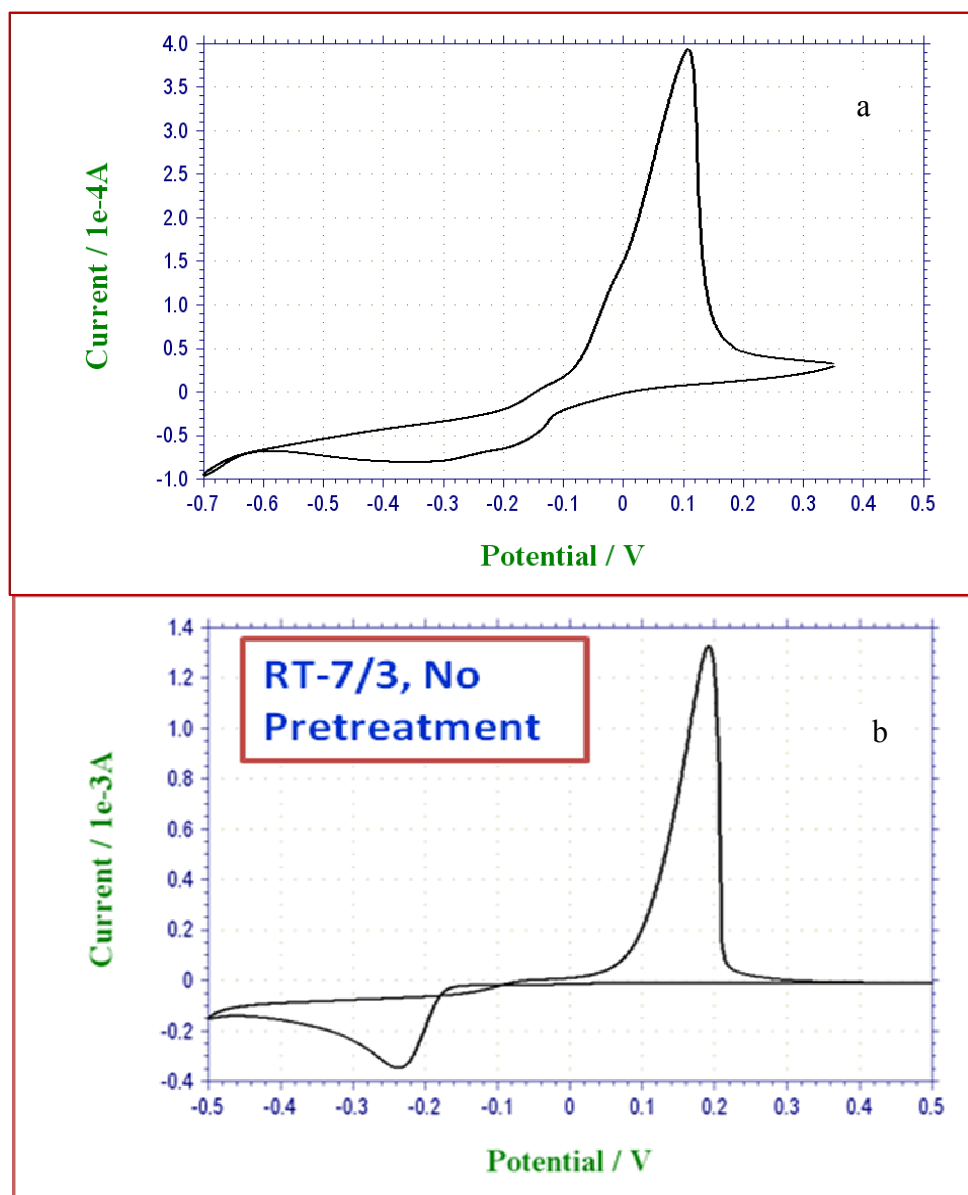
Figure 3.19 CV of RT-7/3 in a) 0.08 M each of CuSO$_4$ + ammonium citrate + KOH, pH 5 and b) 25mM of CuSO$_4$ + 250mM of citric acid + 0.93M of Na$_2$SO$_4$

The citrate ion has been studied to work as a brightening, leveling and buffering agent [23] and the chemical formula for ammonium citrate is (NH$_4$)$_2$HC$_6$H$_5$O$_7$. Kim et al. found that with careful adjustments in the pH of about 3, citrate ions will form complex with Cu and produce good deposition and adhesion properties on TaN and TiN [24]. In ammonium citrate

electrolytes, Cu forms complex with ammonia as $Cu(NH3)_x^{+2}$ which acts as the key reducing agent [25]. As part of that, two different Cu complex electrolytes were used to observe the change in cyclic voltammetry for Ru-Ta electrodes. Figure 3.19a shows the CV of RT-7/3 sample in electrolyte that contains 0.08 M each of $CuSO_4$ + ammonium citrate + KOH, pH 5 and Figure 3.19b shows that in electrolyte that contains 25mM of $CuSO_4$ + 250mM of citric acid + 0.93M of Na_2SO_4. Citric acid, $CitH_3$, is an organic acid with three carboxylic functional groups and a ternary hydroxyl group with the following formula: $COOH-CH_2-COH(COOH)-CH_2-COOH$. The Cu reduction kinetics is found to be faster in citric acid electrolyte than in ammonium citrate which is evident from the well defined reduction peak. It is noted to avoid ammonium complex for depositing Cu on resistive substrates.

3.3.4 Cu Corrosion on Ru-Ta Substrate in CMP Related Environments

In the fabrication of microelectronics, copper was chosen to be the interconnect material because of its high electrical conductivity and higher resistance to electromigration. Cu interconnects are fabricated by a process called dual damascene process due to the lack of volatile byproducts in the reactive ion etching process. The damascene process (Figure 3.20) involves etching a trench through pattern into a dielectric, the blanket deposition of a diffusion barrier followed by Cu electroplating, and finally removal of Cu overburden by chemical–mechanical planarization (CMP) [26-27]. Since the CMP process exposes the Cu interconnect and metal barrier to the continual presence of corrosive chemicals, the resulting bimetallic corrosion can be detrimental to the overall production yields of integrated circuit devices.
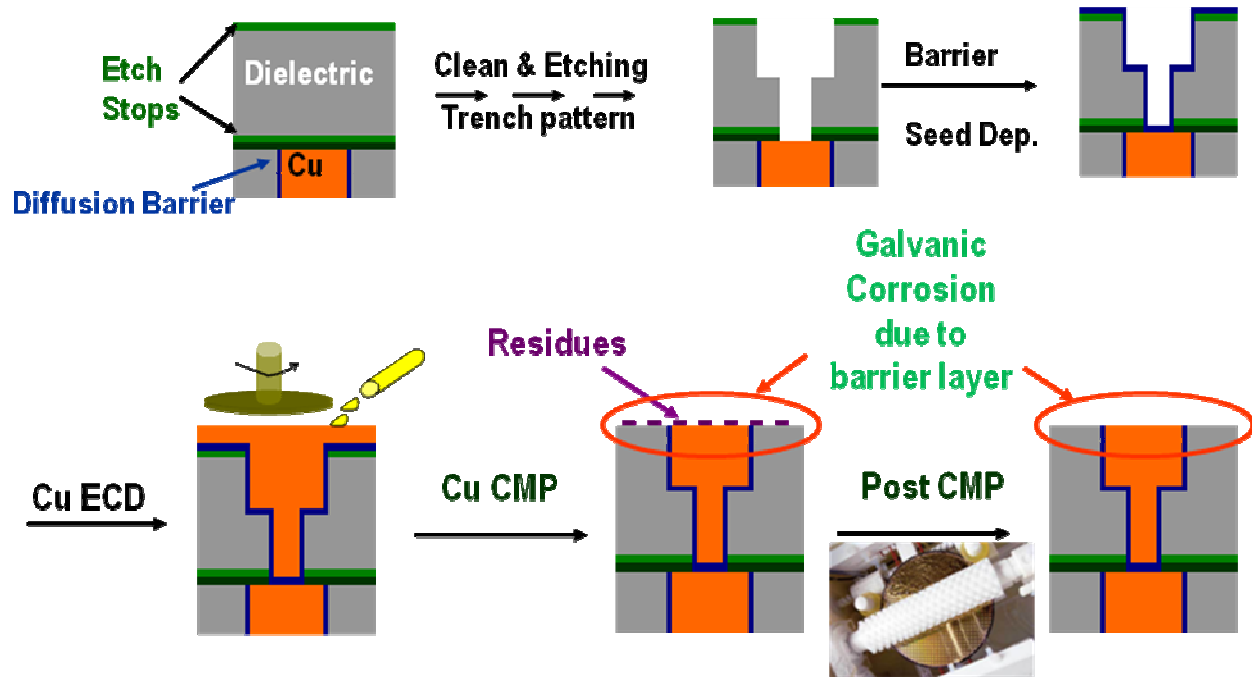
Figure 3.20 Schematic of Cu dual damascene processes showing the location where galvanic corrosion of Cu occurs during CMP.

A methodology is developed to study the bimetallic corrosion rapidly in different corrosive mediums. Fig. 3.21 illustrates the micropattern corrosion screening method [28] used to study the corrosion of Cu on various substrates and in this case Ru-Ta substrate in ammonium citrate solution at pH 9.

Due to the poor adhesion of Cu microdots on the Ru-Ta native oxide surfaces found to be affecting when deposited by sputter deposition technique, the samples were first subjected to surface treatments. The same surface treatments such as forming gas, hydrogen plasma and NaOH immersion were done on Ru-Ta and then they were transferred into the sputtering chamber as quickly as possible to deposit Cu microdots.
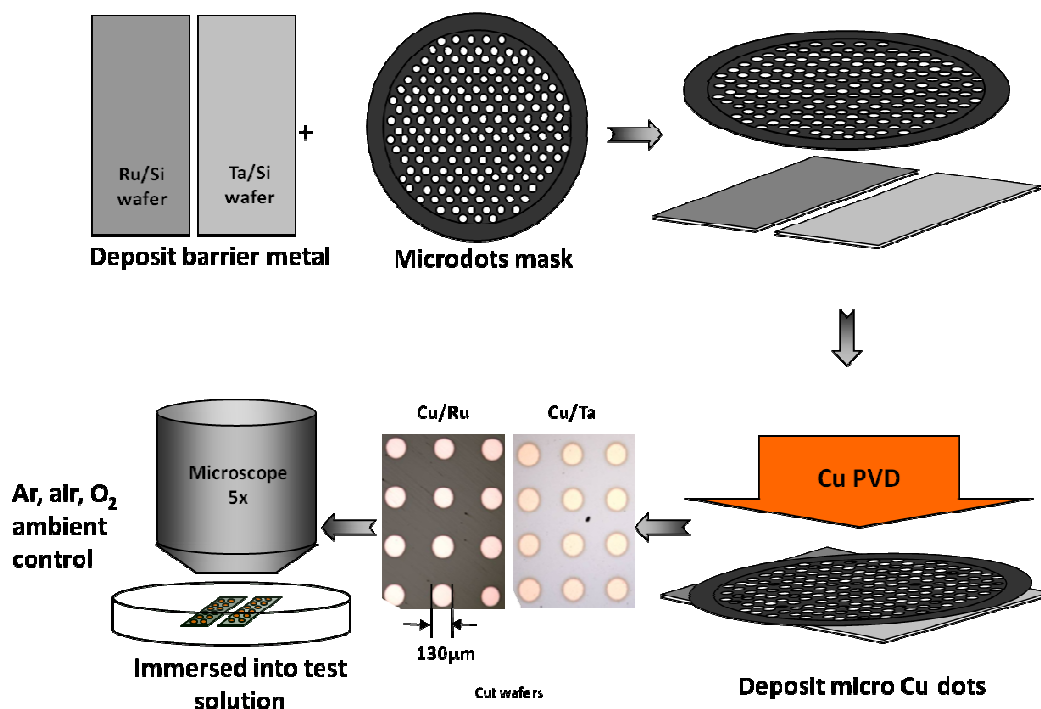
Figure 3.21 Micropattern corrosion screening method
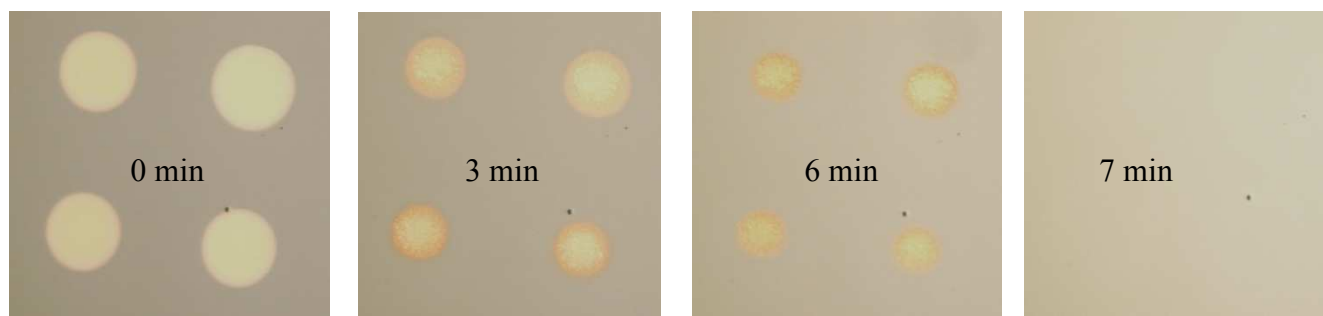
Figure 3.22 Progressive corrosion images of Cu on NaOH etched RT-5/5 in amm. citrate, pH 9

The Cu microdots were deposited for about 25 nm of thickness and the samples were cut into small chips to immerse in the corrosive medium. The progressive corrosion of Cu microdots is observed under 5X magnification optical microscope. Figure 3.22 shows an example for Cu corrosion on NaOH treated RT-5/5 sample in 0.1 M ammonium citrate at pH 9. Similar experiments were done to obtain the corrosion time for all the Cu micropattern on Ru-Ta samples that were treated by various treated by forming gas and hydrogen plasma treatment. The

corrosion time was plotted against all the four Ru-Ta composition samples for different

treatments and shown in Figure 3.23.
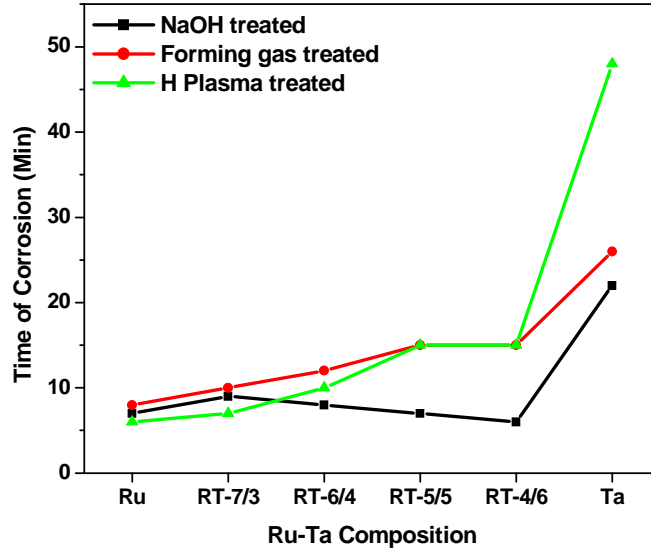
Figure 3.23 Time taken to corrode Cu vs. RT samples for NaOH, FG & HP treatments

For all the NaOH treated Ru-Ta samples, the time taken for corroding the Cu is very

similar to Ru which confirms the previous observation that after NaOH treatment, the surface has

become mostly Ru-like. But for forming gas and hydrogen plasma treatment, the corrosion time

increased when Ta content is increased. This is attributed to the fact that both hydrogen plasma

and forming gas treatment do not remove any Ta from the surface but only reduce the oxides and

thereby having the effect from Ta.   For the reason that Ta provides cathodic protection, Cu on

Ta only surface took the maximum time to corrode which was about 60 min for hydrogen

plasma, 25 min for FG and 23 min for NaOH treatment.
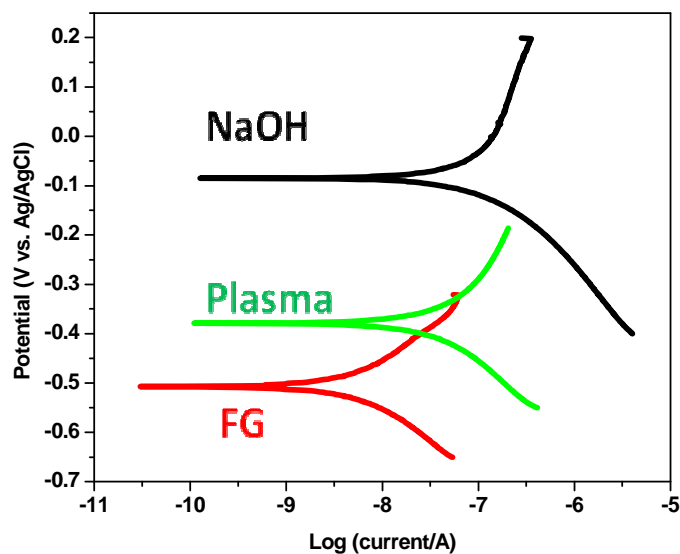
Figure 3.24 Tafel plot for NaOH, FG & HP treated RT-5/5 sample in ammonium citrate, pH 9 solutions
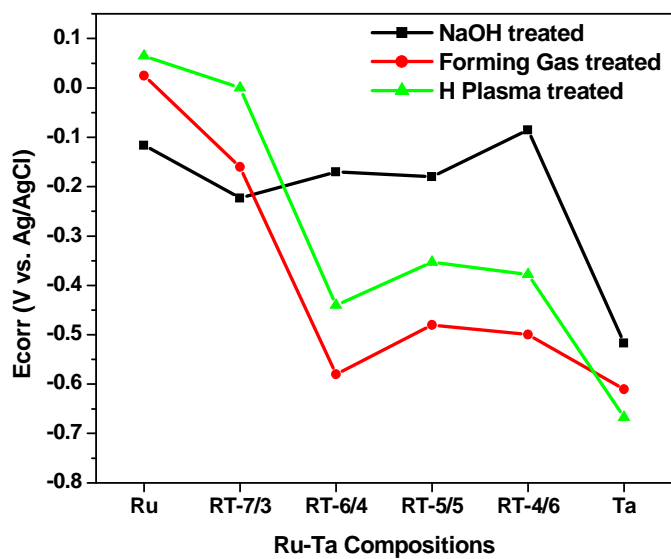
Figure 3.25 Corrosion potentials of all RT samples in 0.1M ammonium citrate, pH 9 solution after different surface treatments

Tafel plot was used to obtain the corrosion potentials of differently treated Ru-Ta samples. Figure 3.24 shows the actual Tafel plot for NaOH, FG & HP treated RT-5/5 sample in 0.1 M ammonium citrate, pH 9 solution. It can be seen from the figure that, the corrosion

potential for NaOH treated sample was very high, about -0.1 V vs. Ag/AgCl and for hydrogen plasma treated sample, it was -0.38 V and -0.6 V for forming gas treated sample. This result was supportive to the observation made on corrosion time. Figure 3.25 shows the corrosion potentials of all different Ru-Ta composition samples treated by all three different surface treatments.

3.4 Conclusion

Electroplating of Cu on various compositions of Ru-Ta thin films have been studied. Cyclic voltammetry results show that the as-deposited RT films form oxide layer on the surface which is found to be preventing Cu nucleation process. Various surface treatments such as forming gas, hydrogen plasma and caustic NaOH treatments have been adopted to evaluate the oxide reduction process in order to improve the Cu deposition. Though forming gas and hydrogen plasma treatment do reduce the surface oxide to certain extent, the Cu reduction was found be very effective in NaOH treated samples irrespective of the amount of Ta present. Adhesion of Cu film was evaluated by Scotch tape method and found to be better in NaOH pretreated samples. Initial studies on the effect of iodine pretreatment, TMAH pretreatment on Cu deposition were done. Using micropattern corrosion screening and Tafel plot techniques, the bimetallic corrosion of Cu deposited on NaOH treated RT samples found to be behaving more like Ru. But the corrosion of Cu microdots deposited on forming gas, hydrogen plasma treated RT samples show a decreased corrosion rate for the increased amount of Ta.

3.5 References

1. H. Kim and Y. Shimogaki, *Proc. of AMC* **2004**, p.551

2. A. Sakata, et al., *Proc. of IITC* **2006**, pp.101-103

3. C-C. Yang, et al., *Proc. of IITC* **2006**, pp.187-189

4. M. Abe, et al., *Proc. of IITC* **2007**, pp.4-6

5. T. N. Arunagiri, Y. Zhang, and O. Chyan, M. El-Bouanani and M. J. Kim, K. H. Chen, C. T. Wu and L. C. Chen, *Applied Physics Letters*, *86*, 083104 (**2005**)

6. Chun-Wei Chen, J. S. Chen, and Jiann-Shing Jeng *Journal of The Electrochemical Society, 155*, 12, H1003-H1008 (**2008**)

7. J.O"M.Bockris, A.K.N.Reddy and M.Gamboa-Aldeco, "*Modern Electrochemistry*", 2nd edition, Volume 2A, Kluwer Academic/Plenum Publishers, **2000**

8. M.A. Lieberman, A.J. Lichtenberg, *Principles of Plasma Discharges and Materials Processing, John Wiley & Sons, Inc.*, New York, **1994**.

9. R. J. Shul and S. J. Pearton (Eds.) *Handbook of Advanced Plasma ProcessingTechniques, Springer*, **2000**.

10. Irina V. Sieber and Patrik Schmuki, *Journal of The Electrochemical Society,* 152 (9) C639-C644 (**2005**)

11. H. Shimizu, F. Sugeno, S. Nishimura, H. Endo and M. Honda, Electrical characterization of anodically oxidized Ta_2O_5 films, *Electrochemistry* 72 (**2004**), pp. 737–742.

12. H.-W.Wang, *J. Mater. Sci. Mater. Electron.* 10, 267 (**1999**).

13. C.-L. Liu, *Appl. Phys. Lett.* 74, 34 (**1998**).

14. K. M. Takahashi, *J. Electrochem. Soc.,* 147, 1414 (**2000**)

15. A. Wieckowski, S. D. Rosasco, B. C. Schardt, J. L. Stickney, and A. T. Hubbard, *Inorg. Chem.,* **23**, 565, (**1984**)

16. F. Lu, G. N. Salaita, H. Baltruschat, and A. T. Hubbard, *J. Electroanal. Chem.,* **222**, 305, (**1987**)

17. A. T. Hubbard, *Chem. Rev. (Washington, D.C.),* 88, 633 (**1988**)

18. G. A. Garwood, Jr. and A. T. Hubbard, *Surf. Sci.,* 121, L524 (**1982**)

19. Hwang, E. S. and Lee, J., *Electrochem. Solid-State Lett*. 3 (**2000**) 138.

20. T. P. Moffat, M. Walker, P. J. Chen, J. E. Bonevich, W. E. Egelhoff, L. Richter, C. Witt, T. Aaltonen, M. Ritala, M. Leskela, and D. Josell, *J. Electrochem. Soc.*, 153, C37 (**2006**)

21. Hyo-Chol Koo, Sung Ki Cho, Chang Hwa Lee, Soo-Kil Kim, Oh Joong Kwon, and Jae Jeong Kim; *Journal of The Electrochemical Society,* 155 (5) D389-D394 (**2008**)

22. Sunjung Kimz and David J. Duquette, *Electrochemical and Solid-State Letters,* 9 2 C38 C40 (**2006**)

23. Aleksandar Radisic, Yang Cao, Premratn Taephaisitphongse, Alan C. West, and Peter C. Searsona, *Journal of The Electrochemical Society*, 150 (5) C362-C367 (**2003**)

24. Kim S "*Seedless copper electrochemical deposition on diffusion barrier materials for ULSI interconnect*", PhD thesis, Rensselaer Polytechnic Institute, **2003**.

25. Banerjee G, Rhoades RL (**2008**) ECS Trans 13:1

26. Armini S, Whelan CM, Moinpour M, Maex K (**2009**) *J Electrochem Soc* 156:18

27. Park JG, Busnaina AA, Hong YK (**2008**) Microelectronic applications of chemical mechanical planarization. Wiley, New York, p 467

28. Kyle Kai-Hung Yu, Karthikeyan S. M. Pillai, Praveen R. Nalla, Oliver Chyan; *J Appl Electrochem* (**2010**), 40(1), 143-149

CHAPTER 4

INTERFACIAL CHARACTERIZATION OF PLASMA TREATED CU SURFACES
RELATED TO ADVANCED CU INTERCONNECTS

4.1 Introduction

The miniaturization of functional elements in integrated circuits (IC) follows Moore's

law which states that the number of transistors on an IC chip doubles every two years.[1] Simple

reduction in the dimensions of components has been successful only to a certain extent beyond

which several problems started to begin. For example, decrease in the thickness of gate

dielectrics resulted in more leakage current through thin oxide layer. Also decrease in dimension

of metallization resulted in increase in the resistance (R) and capacitance (C) of interconnections

and thereby increasing the RC delay [2-3]. It was required to find new materials in order to

follow Moore's law and not simply just reducing in dimensions which did not seem to solve the

problems. RC delay can be reduced by using Cu instead of Al for approximately 35% resistance

reduction; or by using inter-metallic dielectric with dielectric constant k lower than that of SiO_2

(k = 4), so called low-k dielectrics. Replacement of SiO_2 by air ($k = 1$) and Al by Cu with the

same geometry can reduce RC delay by 75% [4]. Two ways to reduce the dielectric permittivity

are to decrease the polarizability of molecules and to decrease the density of dielectric by

imparting porosity [5].

Most popular method to manufacture the low-k dielectric materials is to replace Si-O

bonds in $Si-O_2$ by $Si-CH_3$ and this is commonly referred as "SiOCH" materials. The film

densities and film compositions of SiOCH varies and depends on the method of fabrication.

Plasma processes based both on reactive species and intense ion bombardment are widely used in

the semiconductor manufacturing [6]. The reactive species plasma is used for deposition of

dielectrics and photoresist removal whereas the ion-induced processes find wide use in precision

patterning processes. The main advantage of using plasma etching to make patterns on

dielectrics as opposed to wet etching is its high anisotropy i.e. the ability to provide vertical

etching in the direction normal to substrate and practically no lateral etching in the direction

parallel to the substrate. Though Cu is more conductive and highly favorable than Al, it has

significant drawback with respect to patterning ability. Copper halides are non-volatile and

hence it is difficult to pattern copper by plasma etching [7].   Several approaches have been

investigated to improve the volatility of copper halides, such as wafer heating [8] and exposure

to ultraviolet (UV) radiation [9]; however, none of these methods led to a controllable

manufacturing process. Thus, an alternative method known as 'damascene processing' is used

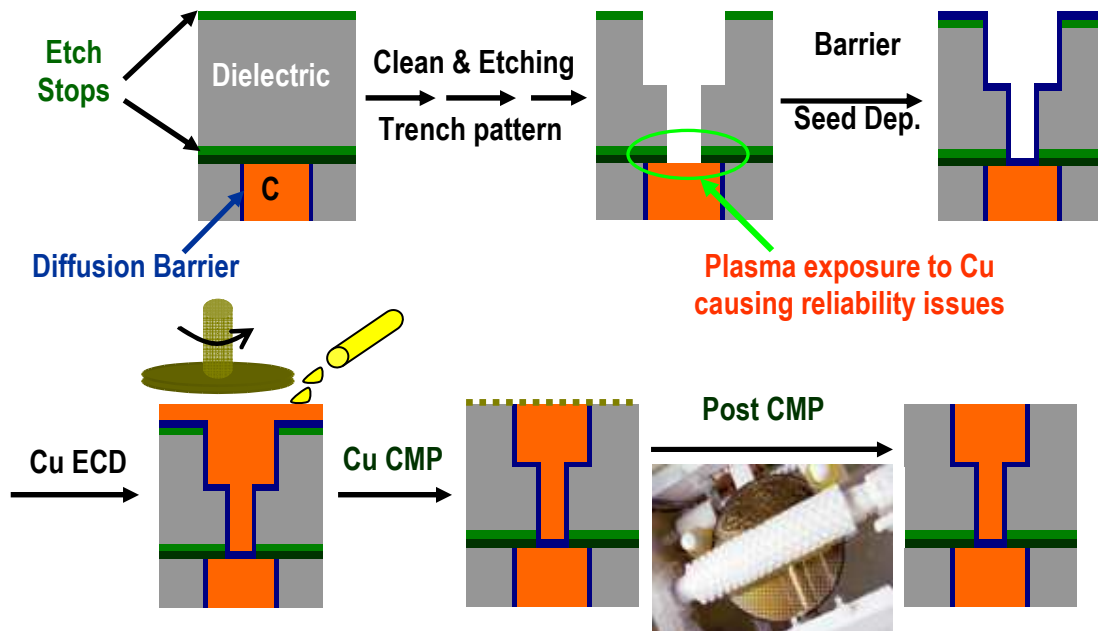instead, to pattern copper [7] and a typical metallization scheme is illustrated in fig. 4.1.

Figure 4.1 Plasma etching of dielectrics and Cu metallization scheme

In this method, the dielectric is first patterned, thereby forming holes or vias to the

underlying conductor layer; copper is then deposited into the vias to form interconnect between

conductor (metal) layers. In the 'dual damascene' method, both via and the metal line are patterned at the same time to reduce the number of processing steps. Copper deposition is performed by electroplating, which effectively fills the vias after they are defined in the dielectric. Excess copper is then removed by chemical mechanical polishing (CMP) [7]. Intermediate layers such as etch stop layers and hard mask layers are used to assist in obtaining precise end or stop points (during plasma etching) and planar surfaces.

Generally fluorocarbon gas plasmas such as CF_4, C_2F_6, CHF_3, and C_4F_8 are used for the etching of dielectrics [10]. Some of the undesired results of this plasma patterning process are the formation of fluorinated layer [11], diffusion of ions into dielectrics etc. All of these undesired processes results in the increase in dielectric constant. When CF_4 gas is used, it results in formation of fluorocarbon polymer deposits on the dielectrics sidewall. Oxygen is used along with CF_4 so that the O atoms decompose CF polymer on the porous silica surface during plasma etching, thereby increasing etch rate. The amount of F radicals generated in CF_4 plasma depends on the amount of O_2 addition because the density of F radicals reaches its maximum value at a certain amount of O_2 [12].

After the low-k dielectric has been etched away for creating vias and trenches, SiN or SiC which is a stopper material to suppress Cu diffusion into the low-k materials was etched by fluorocarbon plasma. During this over etching process, the surface of Cu is also exposed to plasma. Although the plasma will not etch the Cu surface but these fluorocarbon radicals and ions interact with Cu and change the Cu surface chemistry. Since the Cu surface is very reactive, the F ions induce degradation of Cu and results in reliability problems when packaging the electronic components.

After the plasma etching of dielectrics, the photoresist and other plasma residue removal is accomplished by oxygen- and nitrogen- containing plasma ashes but the problem with ash process is that the surface becomes carbon depleted and becomes more hydrophilic [13-14]. An alternative process for post-etch cleaning is done by organic solvents which shows a complete removal of photoresist without carbon depletion and low-k increase [14-16]. It has been shown that the presence of additives in organic solvent had a large impact in photoresist stripping efficiency [17-21]. In order to improve removal efficiency, chemical additives containing fluorine and ammonium hydroxide were considered. Dilute HF and ammonium fluoride (NH_4F) were used due to their different degree of dissociation (in aqueous solution). Tetra methyl ammonium hydroxide (TMAH) was chosen as a source of OH^-. During this cleaning, the underneath Cu surface which has been modified by the interaction of plasma etch gases, is exposed to TMAH which is a most commonly used chemical. To our knowledge, the plasma modified Cu surface chemistry in post-etch cleaning solutions has not been extensively documented in the literature. In order to help creating highly reliable interconnects, knowledge on the behavior of this plasma modified Cu in post-etch cleaning solution is required.

In this work, for the first time we have studied the surface chemistry and corrosion behavior of plasma modified Cu in post-etch cleaning solution. To do this, we deposited Cu microdot patterns on Ru and Ta thin film substrates that are known to be used as Cu diffusion barrier layers and micropattern corrosion testing method was used for corrosion study. The micropattern corrosion scheme is illustrated in Figure 4.2. The Cu/Ru and Cu/Ta micropattern samples were then treated with five different fluorocarbon based gas plasmas from CF_4, CF_4+O_2, CH_2F_2, C_4F_8 and SF_6. Direct corrosion current measurements were done to verify the corrosion trend obtained from micropattern testing results. XPS was used to study the Cu surface chemical

94

bonding. Results of above characterization along with water contact angle measurements are discussed.

4.2 Experiment

The Cu microdots are sputter deposited on Ru and Ta substrates using microdots mask. The diameter of Cu microdots is about 130 micron and thickness is about 50 nm. The Cu/Ru and Cu/Ta micropattern coupons are treated with CF_4, CF_4+O_2, CH_2F_2, C_4F_8 and SF_6 etch gas plasmas. The plasma treatments of these samples were done in Intel lab unit using an OXFORD PLASMALAB 100 system. It is an ICP system where the top and bottom plate bias can be controlled independently. The plasma treatment time was 30 sec for all samples. The pressure maintained was 5 mTorr and temperature was 20°C with 400W top and 50 W RF bias applied. The etch gas at each run are maintained at following flow rate (sccm): 20 C_4F_8/30 Ar, 50CF_4, 50 CF_4/5 O_2, 10 CH_2F_2/30 Ar, 20 SF_6/30 Ar.
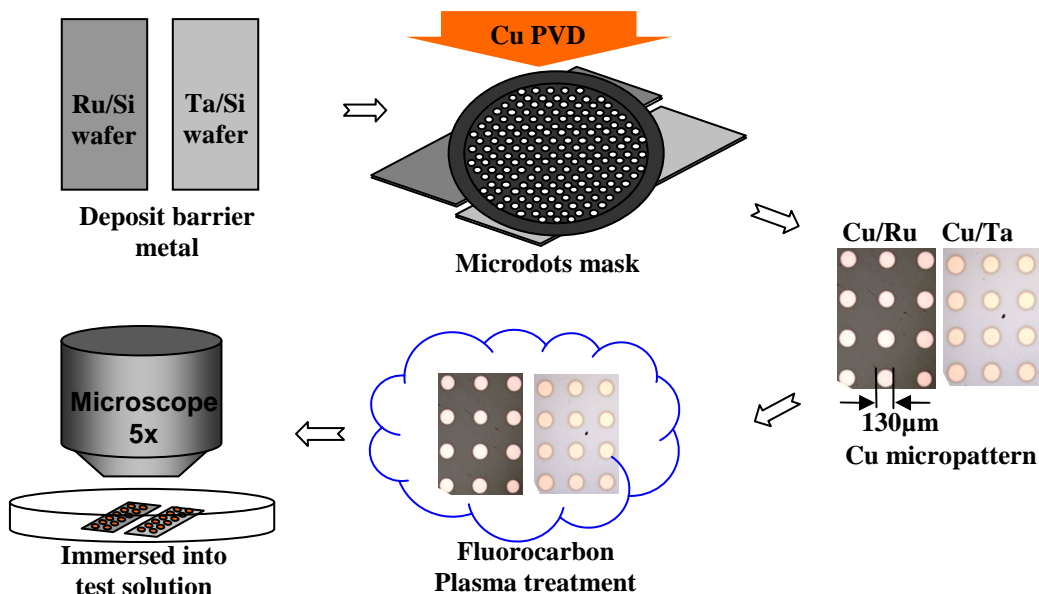

Figure 4.2 Schematic of micropattern corrosion testing method

While the Cu/Ru and Cu/Ta samples are immersed in TMAH, pH 14 solutions the disappearance (corrosion) of Cu dots was observed under optical microscope. Based on the time it takes to corrode the Cu microdots completely, the rate of corrosion was determined for each of the samples. PHI 1600 model XPS system was used to acquire the photoelectron spectra for C, F, O analysis and Cu LMM Auger spectra were obtained to identify the oxide nature on plasma treated Cu surfaces. Direct current measurements were done using Keithley source meter, model 2400. Water contact angles were obtained to evaluate the surface hydrophobicity of plasma treated samples.

4.3 Results and Discussion

4.3.1 XPS Analysis of Plasma Treated Cu

C 1s Peak Analysis

Figure 4.3 shows the C 1s XPS spectra of all plasma treated Cu samples. The carbon present on the surface originates from two sources: from atmosphere and from fluorocarbon gas plasma treatments. Among all those different plasma etch gas treatments, C_4F_8 treated sample distinctively shows multiple carbon peaks at higher binding energies that corresponds to CF (288 eV), CF_2 & CF_3 (292 eV). The high electronegativity of fluorine causes an increased shift in the binding energy of carbon. The multiple C-F bonding are probably due to the high amount of fluorine contained in C_4F_8 gas. The Cu samples treated by other plasma etch gases mostly contained carbon peak at 285 eV that belongs to C-C or C-H bonding.

In order to differentiate the carbon arising due to the plasma treatments from the atmospheric carbon, Ar ion sputtering was done on all the samples and the spectra were shown in Figure 4.4. Cu treated by SF_6 plasma etch gas was taken as a reference point in order to optimize the sputter cleaning parameters required to clean atmospheric carbon. SF_6 treated sample is

chosen because it is expected to contain only atmospheric carbon and none from plasma treatment.
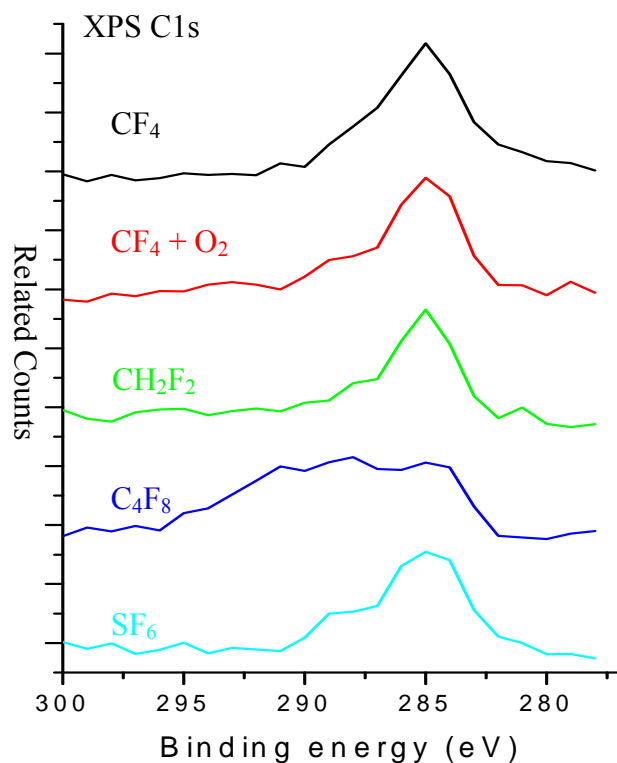

Figure 4.3 XPS C 1s spectra of plasma etch gas treated Cu surfaces

It appears that sputter cleaning for about 5 Å is sufficient to remove the atmospheric carbon from SF_6 treated sample. Hence, the same amount of Ar ion sputtering was also done for all the other samples in order to differentiate the plasma carbon deposits from atmospheric carbon. The carbon peaks intensity significantly decreased from all the samples after sputter cleaning.

F 1s Peak Analysis

F 1s x-ray photoelectron signals were obtained before and after sputter cleaning. Figure 4.5 shows F 1s spectra before sputter cleaning. A huge peak at 688 eV was observed only on sample treated by C_4F_8 which corresponds to fluorine bonding with carbon.
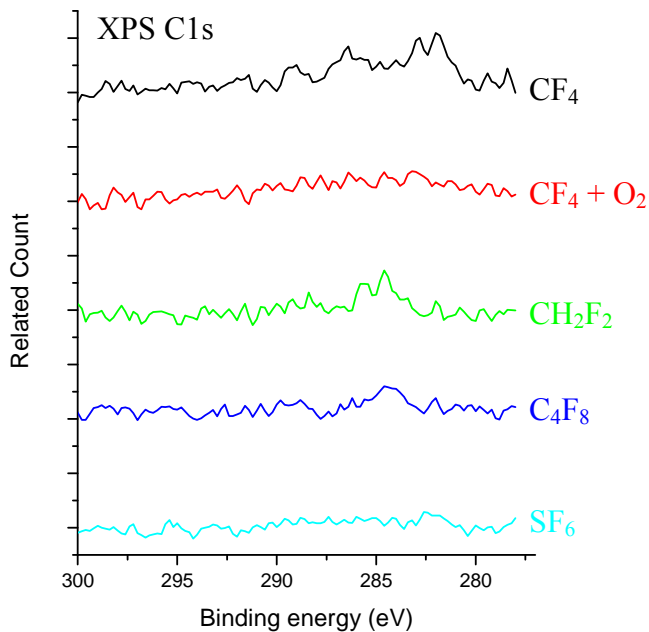

Figure 4.4 XPS C 1s spectra of plasma etch gas treated Cu surfaces after Ar^+ ion sputtering
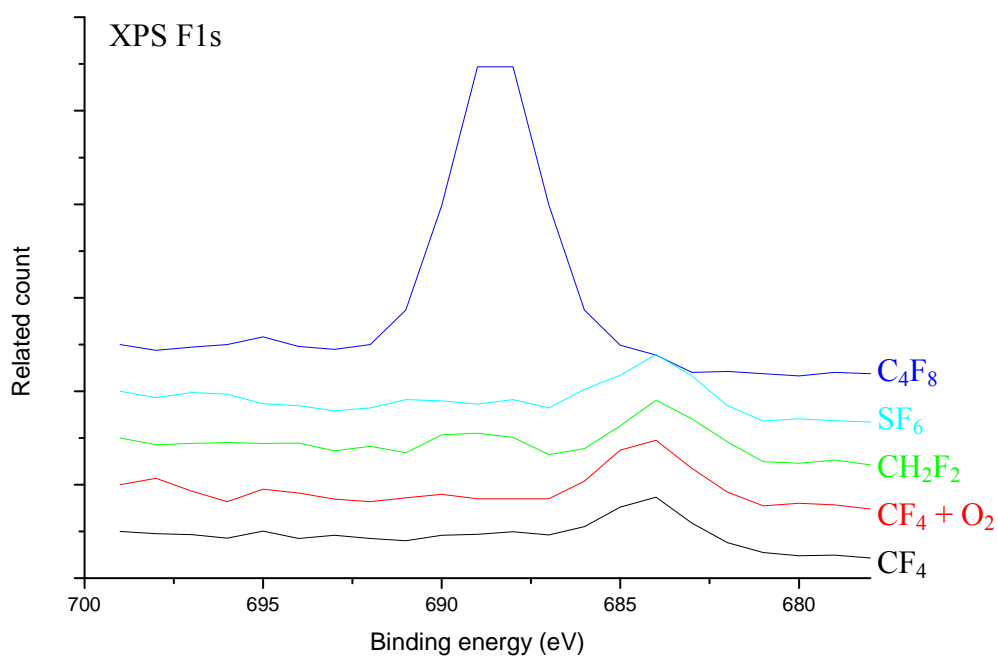
Figure 4.5 XPS F 1s spectra before sputter cleaning

This suggests that the C_4F_8 plasma leaves a lot of fluorocarbon residue on the surface during the treatment. The peak at 684 eV which belongs to Cu bonding with F [22] is present on all other samples except C_4F_8. This indicates C_4F_8 plasma etch gas did not fluorinate the Cu but it only deposits polymer residue on the surface.
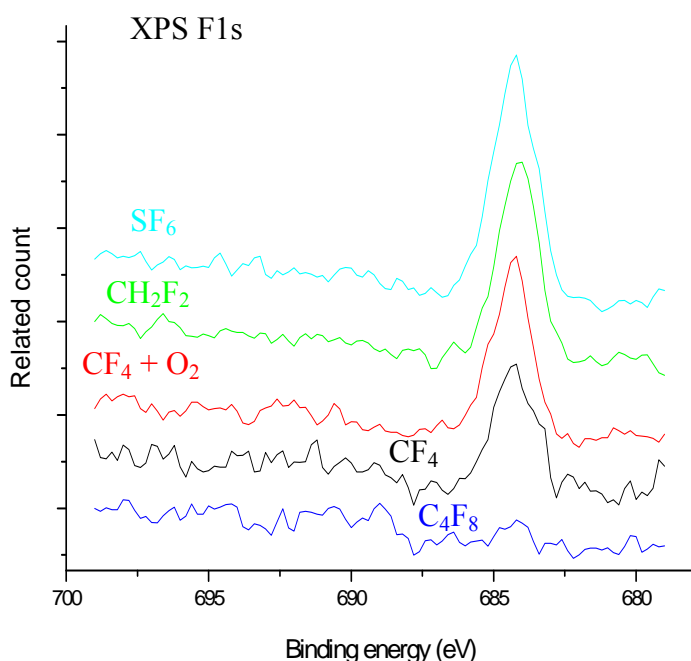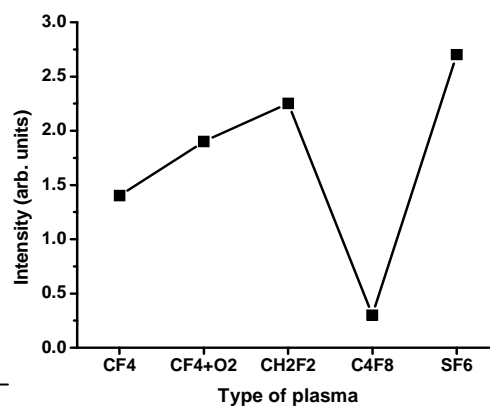
Figure 4.6 XPS F 1s spectra after Ar sputter cleaning

Figure 4.7 Plot of fluorine peak intensity vs. type of plasma etch treatment

Figure 4.6 shows fluorine peaks after 5Å sputter cleaning. It was observed that even after sputter cleaning, the copper-fluorine peak at 684 eV is still present for all samples except C_4F_8 treated Cu sample. Also the huge C-F peak at 688 eV which was present before sputter clean is completely disappeared after 5 Å sputter cleaning.

Figure 4.7 shows the Cu-F peak intensity based on 684 eV for plasma treated samples. The F-Cu peak intensity was highest for SF_6 plasma treated Cu sample and it is very least for C_4F_8. Two of the high fluorine content plasma gases, SF_6 & C_4F_8 behave totally different in terms of Cu fluorination. Compared to CF_4, the Cu-F peak intensity is higher if CF_4 is added with either oxygen or substituted with hydrogen as in the case of CH_2F_2.

The fact that the C_4F_8 leaves only polymer deposits on the surface and do not fluorinate Cu is also evidenced by observing the appearance of Cu (0) peak in Cu LMM Auger spectra as

shown in the figure 4.8. After Ar ion sputter cleaning, the polymer deposits on C_4F_8 treated

sample were removed and the underneath Cu metallic surface is exposed. This is not observed in

other samples where there are not much polymer deposits present. Instead, Cu oxides and Cu

fluorides are terminated on the surface which was not easily removed by the set Ar ion sputter
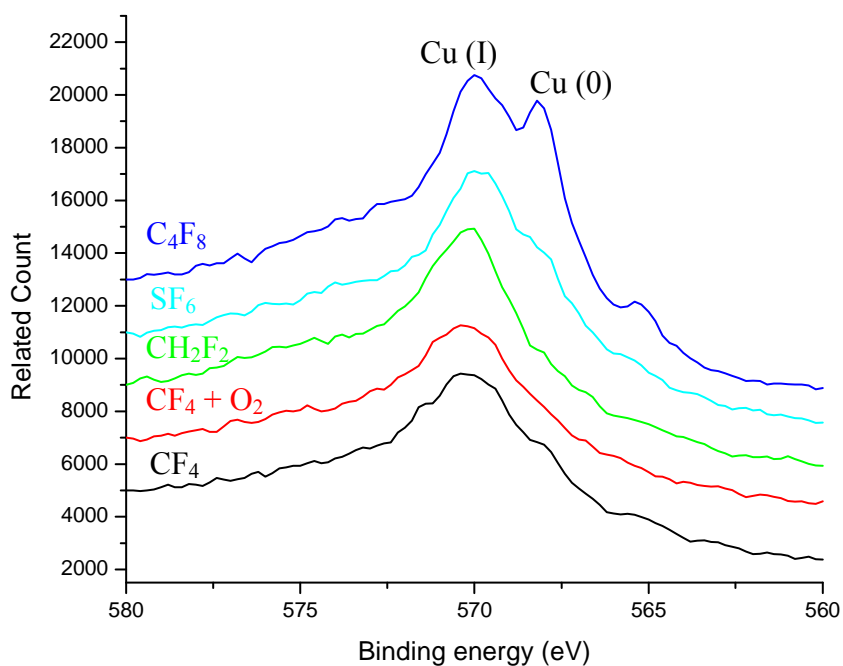
cleaning.

Figure 4.8 Cu LMM spectra of plasma treated Cu samples after Ar ion sputter cleaning
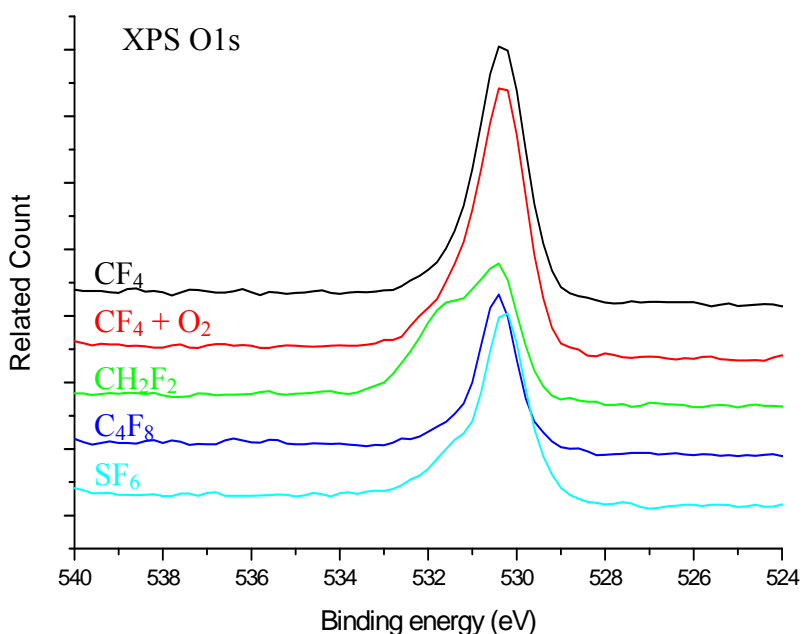O 1s Peak Analysis

Figure 4.9 XPS O 1s spectra after 5 Å sputter cleaning

All the plasma processed Cu surfaces were composed of Cu oxide which is evident from

the presence of oxide peak at 530.4 eV that belongs to oxygen bonding with Cu, shown in figure

4.9. While all other plasma treated surfaces showed a single peak for oxygen, CH_2F_2 showed a

shoulder peak at higher binding energy (531.6 eV) that is found to be the bonding with carbon.

4.3.2 Effect of Plasma Treatments on Cu Corrosion

4.3.2.1 Micropattern Corrosion Testing

The Cu surface chemistry change due to the plasma processing has been a great issue in

terms of their corrosion behavior. To our knowledge, there is no literature published on how

these plasma radicals/ions modified Cu behaves especially in post etch cleaning solutions. We

studied the corrosion properties of these plasma treated Cu samples in 5 % TMAH solution at a

pH of 14, using micropattern corrosion technique [23]. Figure 4.10 shows the corrosion rates of

Cu microdots deposited both on Ru and Ta substrate in TMAH solution. It was observed that the

corrosion is much faster for Cu/Ru than Cu/Ta due to the substrate inducing effect. Since Ru is nobler than Cu, the bimetallic contact between them enhances the galvanic corrosion. Since Ta is less noble than Cu, it provides cathodic protection to Cu and thereby taking more time to corrode. The maximum corrosion rate was 12.5 Å/min for Cu/Ta caused by C_4F_8 treatment and ca. 34 Å/min for Cu/Ru caused by SF_6 plasma treatment. Either way it was observed that the higher fluorine content plasma etch gases i.e. C_4F_8 & SF_6, the interaction of which with Cu surface somehow makes the Cu to corrode faster in TMAH, pH 14 solution.
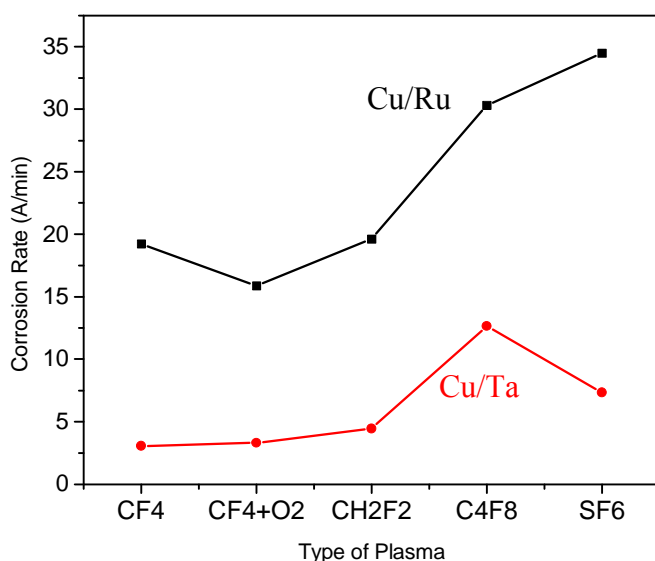
Figure 4.10 Corrosion rate of plasma treated Cu in TMAH, pH 14 Solution

From the XPS data, SF_6 results in Cu fluorination but C_4F_8 just deposits fluorocarbon residues on top of the Cu surface. More controlled experiments have to be done in order to evaluate the effect coming from the interaction between polymer residues, Cu fluoride and the TMAH solution. The other three plasma gases CF_4, CF_4+O_2 and CH_2F_2 treated Cu has similar and lesser corrosion rate 3-5 Å/min for Cu/Ta and 15-20 Å/min for Cu/Ru. The corrosion rate of all plasma modified Cu on Ta substrate is higher than untreated Cu/Ta that consists only of air

exposed oxide on the surface. The important observation to be noted is that the fluorinated and plasma modified Cu is easier to corrode in TMAH solution compared to air exposed Cu oxide.

4.3.2.2 Direct Galvanic Current Measurements

In order to verify the corrosion rates from micropattern testing, we measured the actual galvanic corrosion current from each of these plasma modified Cu samples coupled with Ru. This was done by connecting both the electrodes i.e. plasma-Cu sample and Ru shot to the two terminals in Keithley source meter and immersing them in TMAH solution. To obtain comparable current values, the area of the plasma-Cu electrodes exposed to the solution was fixed and same for all the samples. The measurement was taken as soon as the electrodes are immersed in the solution to record the initial corrosion current as the initial current responses varied for different plasma treated samples. Figure 4.11 shows the galvanic corrosion current of plasma treated Cu samples over the time of immersion in TMAH against Ru shot electrode. It was ensured that the state of Ru surface is always fresh polished before measuring the current for plasma treated Cu samples. It appears that the corrosion current is least for CF_4+O_2 treated Cu sample and maximum for Cu treated with C_4F_8 and SF_6. This supports the micropattern corrosion data because the rate of corrosion is directly proportional to corrosion current.
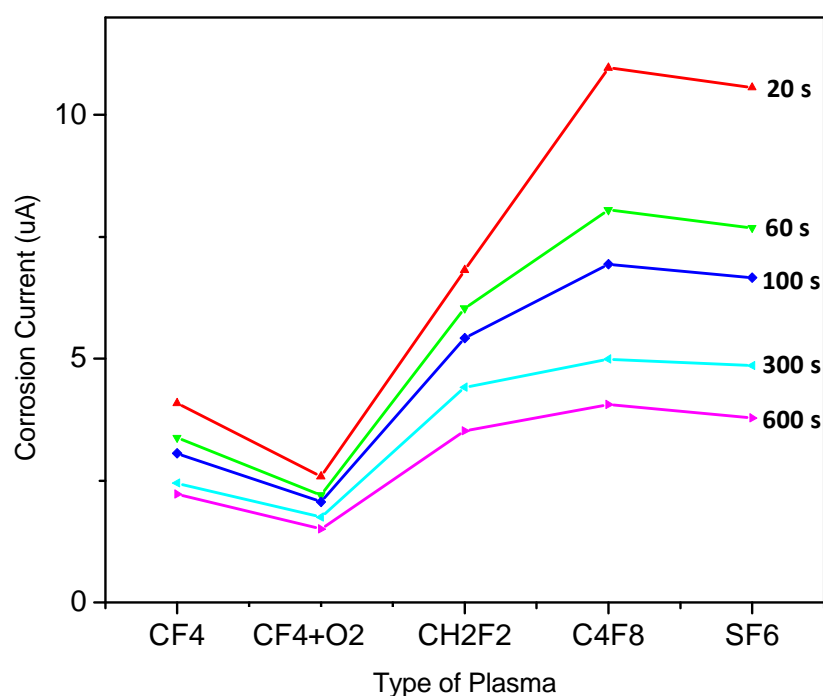
Figure 4.11 Direct galvanic current for plasma-Cu samples against Ru shot electrode in TMAH, pH 14 solution

4.3.2.3 Water Contact Angle Measurements

Water contact angle is a simple technique used to quickly identify the nature of any surfaces. A droplet of DI water is slowly introduced on the surface of plasma treated Cu samples to characterize about hydrophilic and hydrophobic nature by contact angle measurement. Figure 4.12 shows the trend of water contact angle on these plasma modified Cu surfaces over different immersion time in TMAH solution and totally for 30 minutes. The contact angles are measured only on Cu surface and there was no exposure of either Cu/Ru or Cu/Ta interface.
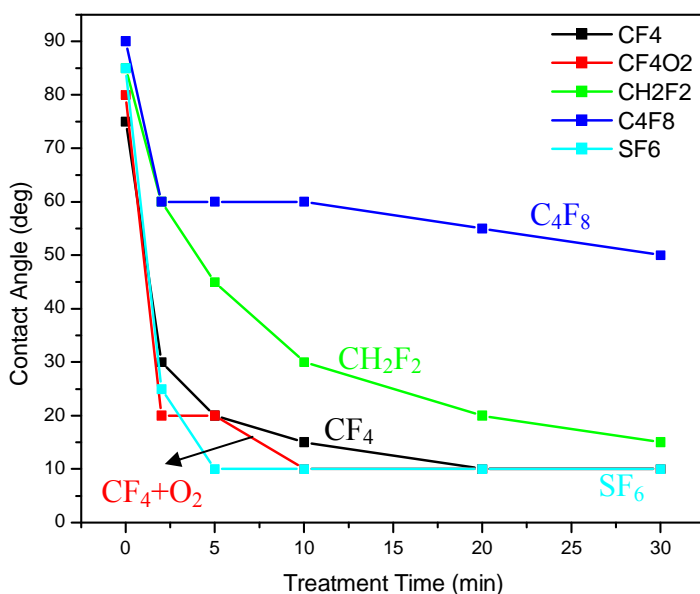
Figure 4.12 Water contact angles on plasma etch gas treated Cu surfaces

Prior to TMAH treatment, the contact angles for all plasma treated Cu samples were about 75° to 90°. Just after immersing for 2 min TMAH, the samples that were subjected to CF$_4$, CF$_4$+O$_2$ and SF$_6$ plasma treatments became hydrophilic. This indicates that the CF$_x$ polymer deposits on the surface are easily removed by alkaline TMAH solution likely due to less CF$_x$ polymer deposits. The extent of Cu oxidation is higher in CF$_4$+O$_2$ makes the contact angle decrease to 20° in 2 min of treatment. The galvanic corrosion current is lowest for CF$_4$+O$_2$ indicating a slight passivity of surface and the XPS result show comparatively higher oxide peak intensity. With the combined results from contact angle, corrosion current, and XPS, it can be hypothesized that the surface layers may be composed of mixture of Cu oxides and polymers in CF$_4$+O$_2$ sample. In 20 min of treatment, CF$_4$, CF$_4$+O$_2$ & SF$_6$, all reach the same hydrophilic character. H is added to fluorocarbon gases for the purpose of minimizing the low-k damage during plasma etching. In CH$_2$F$_2$ the decrease in contact angle is gradual and close to linear over

106

time. This suggests that CH_2F_2 forms a post-etch residue layer that is relatively resistant to TMAH attack. As expected, the contact angle maintained higher value for C_4F_8 treated sample even after treating the sample for 30 minutes. This proves that the surface is deposited full of CF_x polymer residue.

4.4 Conclusion

New insights have been provided on the Cu corrosion behaviors treated by different plasma etch gases in TMAH alkaline solution. The corrosion rate of plasma gas treated Cu on Ru and Ta substrates was observed using micropattern corrosion screening method. It shows that the corrosion rate of all the fluorocarbon gas plasma treated Cu samples is higher than that of non-treated blank Cu. Though the samples were treated by etch gas plasma, the corrosion rate is found to be affected by Cu/Ru and Cu/Ta interface. Enhanced corrosion was observed for Cu/Ru than Cu/Ta which was attributed to higher nobility of Ru. XPS results confirm the presence of Cu oxides and Cu fluoride in all the samples except C_4F_8. Compared to other gas plasma treatments, C_4F_8 resulted in depositing a large amount of fluorocarbon residues on the surface. This is attributed to the higher amount of C and F in C_4F_8 compared to other gases. From the contact angle measurements, it was evident that C_4F_8 treated Cu showed greater resistance to cleaning with TMAH solution while other plasma treatments like CF_4, CF_4+O_2 and SF_6 , Cu can be cleaned within 10 min.

4.5 References

1. Gorden Moore**,** *Electronics*, Volume 38, Number 8*,* April 19, **1965**.

2. M, T. Bohr, "*interconnect scaling - the real limiter to high performance VLSI*," *Tech. Dig*. **1995** IEDM. p. 241.

3. R L hl Dang and N. Shigyo, "*Coupling capacitance for two-dimensional wires*," IEEE Electron Device Letters,EDL-2, p.196,**1981**.

4. W. W. Lee and P. S. Ho, *MRS Bull*. 10, 19 (**1997**)

5. D. Shamiryan, T. Abell, F. Iacopi1 and K. Maex, *Materials today*, **2004**

6. D. Shamiryan, M. R. Baklanov, S. Vanhaelemeersch, and K. Maex, *J. Vac. Sci. Technol*. B, Vol. 20, No. 5, Sep/Oct **2002**

7. C. K. Hu, and J. M. E. Harper, *Materials Chemistry and Physics*, 52 (1), pp. 5-16 (**1998**).

8. H. Miyazaki, K. Takeda, N. Sakuma, S. Kondo, Y. Homma, and K. Hinode, *Journal of Vacuum Science & Technology*, B15 (2), pp. 237-240 (**1997**).

9. K. Choi, and C. Han, *Japanese Journal of Applied Physics, Part 1*, 37 (11), pp. 5945-5948 (**1998**).

10. J. A. Mucha, D. W. Hess, and E. S. Aydil, "Plasma Etching," in *Introduction to Microlithography*, L. F. Thompson, C. G. Willson, and M. J. Bowden, 2nd Edition, Washington, DC, American Chemical Society (**1994**).

11. M. R. Baklanov, M. Van Hove, G. Mannaert, S. Vanhaelemeersch, H. Bender, T. Conard, and K. Maex, *J. Vac. Sci. Technol*. B 18, 1281 (**2000**)

12. C. J. Mogab, A. C. Adams and D. L. Flamm: *J. Appl. Phys*. 49 (**1978**) 3796.

13. K. Maex, M.R. Baklanov, D. Shamiryan, F. Iacopi, S.H. Brongersma, Z.S. Yanovitskaya, *J. Appl. Phys*. 93 (**2003**) 8793.

14. Q.T. Le, J. Keldermans, N. Chiodarelli, E. Kesters, M. Lux, M. Claes, G. Vereecke, Jpn. *J. Appl. Phys*. 47 (**2008**) 6870.

15. M. Claes, Q.T. Le, E. Kesters, M. Lux, A. Urionabarrenetxea, G. Vereecke, P.W. Mertens, *ECS Trans*. 11 (2) (**2007**) 177.

16. Q.T. Le, N. Chiodarelli, I. Blum, E. Kesters, M. Lux, M. Claes, G. Vereecke, P.W. Mertens, in: *Sematech Surface Preparation and Cleaning Conference*, Austin, Texas, April 25–26, **2007**.

17. S. Ojima, T. Jizaimaru, S. Omae, T. Ohmi, *J. Electrochem. Soc*. 144 (**1997**) 4005.

18. G. Levitin, C. Timmons, D.W. Hess, *J. Electrochem. Soc*. 153 (7) (**2006**) G712– G720.

19. Y.-S. Lim, D.-C. Bae, H.-J. Kim, Y.-N. Kim, Y.-H. Kim, T.-S. Kim, *Mater. Res. Soc. Symp. Proc*. 990 (**2007**) B07–B16.

20. T. Maruyama, H. Abe, T. Karita, T. Aoyama, *US Patent 6440326 B1*, **2002**.

21. D. Danielson, T.-L. Huang, D.L. Scovell, K. Willis, *US Patent 7087996 B2*, **2006**.

22. George G. Totir, Gary S. Chottiner, Christopher L. Gross, Daniel A. Scherson; *Journal of Electroanalytical Chemistry* 532 (**2002**) 151 (156)

23. Kyle Kai-Hung Yu, Karthikeyan S. M. Pillai, Praveen R. Nalla, Oliver Chyan; *J Appl Electrochem* (**2010**), 40(1), 143-149